

COMENIUS UNIVERSITY IN BRATISLAVA  
FACULTY OF MATHEMATICS, PHYSICS AND INFORMATICS

**Secular changes of orbits in the  
hierarchical quadruple VW LMi**

Master's Thesis

COMENIUS UNIVERSITY IN BRATISLAVA

FACULTY OF MATHEMATICS, PHYSICS AND INFORMATICS



# Secular changes of orbits in the hierarchical quadruple VW LMi

Master's Thesis

<b>Field of Study</b>	Physics
<b>Study Programme</b>	1140 and 1141, Astronomy and Astrophysics
<b>Supervisor</b>	RNDr. Theodor Pribulla, CSc.
<b>Department</b>	Department of Astronomy, Physics of the Earth and Meteorology

Bratislava, 2019

Bc. Emil Puha



## THESIS ASSIGNMENT

- Name and Surname:** Bc. Emil Puha  
**Study programme:** Astronomy and Astrophysics (Single degree study, master II. deg., full time form)  
**Field of Study:** Physics  
**Type of Thesis:** Diploma Thesis  
**Language of Thesis:** English  
**Secondary language:** Slovak
- Title:** Secular changes of orbits in the hierarchical quadruple VW LMi
- Annotation:** VW LMi is a very tight quadruple system composed of a contact eclipsing binary star with orbital period of 0.47755 days and a detached non-eclipsing pair with orbital period of 7.93 days. The binaries revolve each other in 355 days. With medium to high dispersion spectroscopy radial velocities of all components can be reliably determined. The 355-days outer orbit is visible in timing variability of the eclipsing pair. The spectroscopic and the timing data can be combined to arrive at accurate component and orbital parameters. Recently it was shown that because of the short mutual orbital period the inner binaries should show significant secular changes caused by gravitational perturbations. While inclination angle of the eclipsing pair is predicted to change by a few tens of degrees the non-eclipsing pair should show changes as large as 10 degrees. The orbit of the wider, non-eclipsing binary is eccentric. Thus, it is probable that apsidal motion would be detected and affected by gravitational perturbations. The evolution of the system will be, very probably, affected by the angular momentum transfer between the binaries and the outer orbit.
- Aim:** Detection and analysis of secular changes of inner orbits in hierarchical quadruple system VW LMi. Determination of absolute parameters of its components as well as orbital elements. Discussion of the origin and further evolution of this tight quadruple system.
- Literature:** Hilditch, R.W., 2001, An Introduction to Close Binary Stars, Cambridge  
Vokrouhlicky, D., 2016, MNRAS 461, 3964  
Pribulla, T. et al., 2008, MNRAS 390, 798
- Comment:** The student is expected to obtain echelle spectroscopy of VW LMi with 60cm and 1.3m telescopes of the Astronomical institute of the Slovak Academy of Sciences. The multi-colour photometry could be obtained with a 28cm student telescope of the Comenius university. The data reduction will be done using dedicated pipelines in IRAF but basic programming and scripting skills are required. The analysis of spectra will be performed mostly in IDL. Analysis of orbit perturbations will require development of a new software tools. Good knowledge of English is necessary.
- Supervisor:** RNDr. Theodor Pribulla, CSc.  
**Department:** FMFI.KAFZM - Department of Astronomy, Physics of the Earth and Meteorology



Comenius University in Bratislava  
Faculty of Mathematics, Physics and Informatics

---

**Head of  
department:**

prof. RNDr. Peter Moczo, DrSc.

**Assigned:**

16.11.2017

**Approved:**

19.11.2017

prof. Ing. Pavel Mach, CSc.  
Guarantor of Study Programme

Student

Supervisor

# Declaration

I hereby, declare that this thesis is my own work and that, to the best of my knowledge and belief, it contains no material which has been accepted or submitted for the award of any other degree or diploma.

I also declare that, to the best of my knowledge and belief, this thesis contains no material previously published or written by any other person except where due reference is made in the text of the thesis.

---

Bc. Emil Puha

# Aknowledgements

I would like to express my deep gratitude to RNDr. Theodor Pribulla, Csc., my research supervisor, for his patient guidance, enthusiastic encouragement and useful critiques of this thesis.

# Abstract

VW LMi was classified as an W UMa-type eclipsing binary after the discovery of photometric variability by Hipparcos mission in 1997. Long-term spectroscopy (Pribulla et al., 2006) showed that VW LMi is a quadruple system consisting of a contact eclipsing binary and a non-eclipsing binary. The short outer orbital period (355 days) indicates a presence of significant orbital perturbations in the inner sub-systems. The aim of this thesis was to improve orbital elements and physical parameters of components but also to search for secular changes. First of all, new spectra from Stara Lesná, Skalnaté pleso and Tautenburg observatories were deconvolved in order to obtain the broadening functions and the radial velocities of the components. The fitting of observed radial velocities as well as light-time effect visible in the photometric data was crucial to determine orbital parameters. These parameters were used in further numerical simulations to investigate evolution of the system and to constrain mutual inclination of the inner and outer orbits.

**keywords:** hierarchical quadruple, secular orbital changes

# Abstrakt

VW LMi bola klasifikovaná ako zákrytová premenná typu W UMa po objave jej fotometrickej premennosti misiou Hipparcos v roku 1997. Dlhodobá spektroskopia (Pribulla et al., 2006) ukázala, že VW LMi je štvorhviezdny systém pozostávajúci zo zákrytovej dvojhviezdy a nezákrytovej dvojhviezdy. Krátka vonkajšia obežná doba (355 dní) naznačuje prítomnosť výrazných dráhových porúch vnútorných podsystémov. Cieľom práce bolo presnejšie určenie dráhových elementov a fyzikálnych parametrov jednotlivých zložiek a hľadanie sekulárnych zmien dráh. V prvom rade sa spektrá z observatórií Stará Lesná, Skalnaté pleso a Tautenburg rozložili, aby sa získali funkcie rozšírenia a radiálne rýchlosti zložiek. Fitovanie napozorovaných radiálnych rýchlostí, ako aj light-time effect (LITE) pozorovaný vo fotometrických dátach boli kľúčovými pri určovaní dráhových elementov. Tieto elementy boli využité pri následných numerických integráciách systému, pri ktorých sa skúmala evolúcia systému pri rôznych hodnotách inklinácie medzi vnútornými dráhami a vonkajšou dráhou.

**kľúčové slová:** štvorhviezdny systém, sekulárne zmeny dráhy

# Preface

Systematic spectroscopic study of VW LMi by Pribulla et al. (2008) indicated a presence of significant orbital perturbations in the hierarchical quadruple system. The aim of this thesis is the further study of the system: precise determination of its orbital parameters and secular orbital changes. The main tool used is spectroscopy. Radial velocities of components determined from observed spectra via deconvolution routines in IDL as well as light-time effect observed in photometric data are crucial for the resolution of orbital parameters. For the demands of this thesis we developed a computer code to fit observed values of radial velocities with the radial velocity equation. Using multidimensional minimization this fit provides almost all Keplerian orbital parameters of the system. Comparing the results with parameters determined by Pribulla et al. (2008) the orbital changes due to secular orbital perturbations should be visible. To take a look at the further evolution of the system we developed another code: a model that numerically integrates the components in time. Via setting various initial conditions we resolved all missing orbital parameters that could not be determined through radial velocity fitting. Setting all resolved orbital elements as parameters for our model provided us a look on the evolution of hierarchical quadruple VW LMi as well as the trends of the system's secular orbital changes.

Aristotle said a bunch of stuff that was wrong. Galileo and Newton fixed things up. Then Einstein broke everything again. Now, we have basically got it all worked out, except for small stuff, big stuff, hot stuff, cold stuff, fast stuff, heavy stuff, dark stuff, turbulence and the concept of time (Weinersmith, 2017). One aim of this thesis is to extend the present knowledge of the multiple stuff. We hope that this thesis will contribute to the better understanding of behaviour and celestial mechanics of this tight quadruple system as well as of multiple stellar systems in general.

# Contents

<b>1</b>	<b>Multiple stellar systems</b>	<b>1</b>
1.1	Mechanisms of quadruple star formation . . . . .	2
<b>2</b>	<b>Secular orbital changes</b>	<b>4</b>
2.1	The Kozai-Lidov effect . . . . .	5
2.2	The eccentric Kozai-Lidov effect . . . . .	10
2.3	Kozai-Lidov effect in quadruple systems . . . . .	12
2.4	Empirical stability limit . . . . .	13
<b>3</b>	<b>Presenting VW LMi</b>	<b>16</b>
3.1	Orbital parameters of VW LMi . . . . .	17
3.2	Presence of secular orbital changes . . . . .	19
<b>4</b>	<b>Numerical integration of orbits</b>	<b>21</b>
4.1	Encke's Method . . . . .	21
4.2	Cowell's Method . . . . .	22
4.3	Numerical integrators . . . . .	24
<b>5</b>	<b>Radial velocity and Doppler effect</b>	<b>26</b>
5.1	Cross-correlation technique . . . . .	27
5.2	Broadening function technique . . . . .	28
5.3	Spectroscopic orbit . . . . .	31
5.4	Spectroscopic orbits in quadruple systems . . . . .	33
<b>6</b>	<b>Photometry</b>	<b>35</b>
6.1	The light-time effect . . . . .	36
6.2	Minima determination . . . . .	37
6.3	LITE and VW LMi . . . . .	39
6.4	Combining spectroscopy and photometry . . . . .	40

<b>7</b>	<b>New observations of VW LMi</b>	<b>41</b>
7.1	Spectroscopic observations . . . . .	41
7.2	Photometric observations . . . . .	42
<b>8</b>	<b>Data processing</b>	<b>44</b>
8.1	IDL . . . . .	45
8.2	Orbit fitter . . . . .	47
8.3	<i>Coordinates</i> module . . . . .	50
8.4	N-body model . . . . .	51
8.5	<i>Elements</i> module . . . . .	53
<b>9</b>	<b>Results</b>	<b>54</b>
9.1	Radial velocities . . . . .	54
9.2	The orbital parameters . . . . .	55
9.3	Numerical integration of VW LMi . . . . .	59
9.4	Secular orbital changes in orbits of VW LMi . . . . .	61
<b>10</b>	<b>Conclusion</b>	<b>65</b>
10.1	Discussing our software tools . . . . .	65
10.2	Discussing our results . . . . .	66
10.3	Discussing the nature of secular perturbations . . . . .	70
10.4	Overview . . . . .	71
	<b>Bibliography</b>	<b>73</b>
<b>A</b>	<b>New radial velocities and minima times</b>	<b>79</b>
<b>B</b>	<b>The orbit fitter</b>	<b>82</b>
<b>C</b>	<b>The <i>Coordinates</i> module</b>	<b>89</b>
<b>D</b>	<b>The N-body model</b>	<b>92</b>
<b>E</b>	<b>The <i>Elements</i> module</b>	<b>97</b>

# Chapter 1

## Multiple stellar systems

The following chapter is dedicated to overview the present knowledge of stellar multiple systems. As multiple stellar systems we consider systems with at least three stars tied together by gravitational attraction. As discussed in Tokovinin (1997), multiple systems are useful objects as they provide precise values of stellar masses and luminosities - properties tied together via relation  $L = M^\alpha$ , which help us understand the processes of the stellar evolution. On the other hand, from the dynamical point of view, these systems aid our understanding of the formation of physical multiples or higher order stellar systems. We do recognize two categories of multiple systems:

- Chaotic multiple systems
- Hierarchical multiple systems

Chaotic systems, as their name suggests, have chaotic dynamics. These systems, also called trapezia, have strongly interacting orbits, therefore they are dynamically unstable. On the other hand, hierarchical systems have stable orbits, which could be divided into smaller nested sub-orbits. It is important to note, that the mentioned sub-orbits could be treated as Keplerian two-body problems, whilst chaotic systems must be treated via N-body problem. Hierarchical multiple systems are described through mobile diagrams as proposed by Evans (1968). These diagrams are simply just binary trees divided into levels. The widest system forms the uppermost level of the diagram, every other component is represented as a bifurcation at the next level. Mobile diagrams are alterable - they represent the present knowledge of the multiple stellar system and could be changed as new components are discovered (mostly via spectroscopic or interferometric observations). Accordingly, the terms as "triple", "quadruple" or "quintuple" represent our current knowledge, rather than the true multiplicity of the system. Examples of mobile diagrams are shown in Figure 1.1.

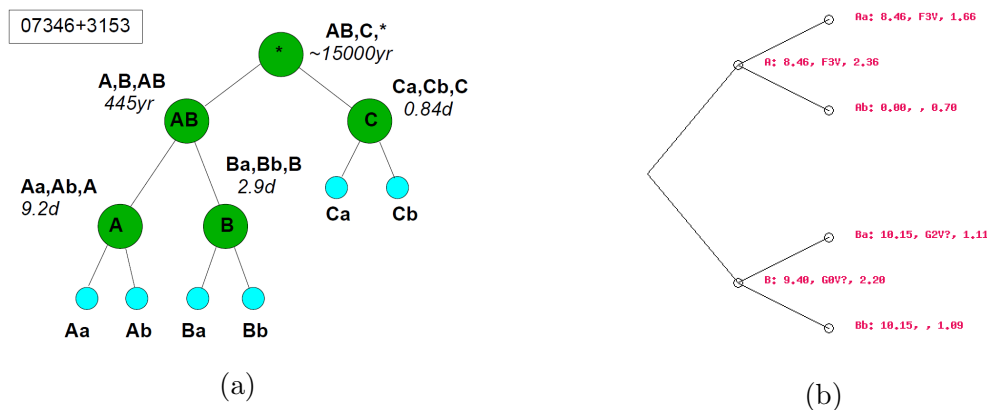


Figure 1.1: Examples of mobile diagrams. (a) Mobile diagram of sextuple system  $\alpha$  Gemini - Castor. Credit: Tokovinin (2018). (b) Mobile diagram of VW LMi. Credit: Tokovinin’s Multiple Stellar Catalogue (MSC).

Comparing various catalogs of multiple stellar systems, it is clear, that the majority of such systems are hierarchical and not chaotic (Tokovinin, 1997). However, this fact seems to be obvious: chaotic systems are dynamically unstable, they must not appear as physically bound systems at all. Moreover, these systems disintegrate hastily to separate rogue stars or smaller hierarchical systems, therefore there is a lower probability of observing such systems.

## 1.1 Mechanisms of quadruple star formation

Stars form after gravitational collapse in interstellar gas clouds, while the collapse generally occurs in more regions of the cloud. This means, that multiple stars form from one interstellar cloud and they create loosely bound stellar open clusters. The further fate of these clusters was discussed in (Tokovinin, 2004a). The cartoon showing the current understanding of multiple stars formation is shown in Figure 1.2.

First of all, stars evolve in a collapsing cloud, which is often part of a larger interstellar gas cloud. The protostars accrete cloud material and fall towards the center of the cloud as the timescale of both processes is roughly  $10^4 - 10^5$  yrs. At the first close encounter of protostars, interstellar surrounding gas is still present and it significantly affects the further dynamical evolution of the cluster. Single or binary stars may be ejected from this system and some unstable hierarchical multiples may form. Stronger hierarchies may form through dynamics and tidal dissipation. Or the initial weak hierarchies may become unstable as the remaining gas of the cloud interacts with their outer components. Studies of statistical properties of multiple star lead to comprehension of quadruple stellar systems formation mechanism as published in (Tokovinin,

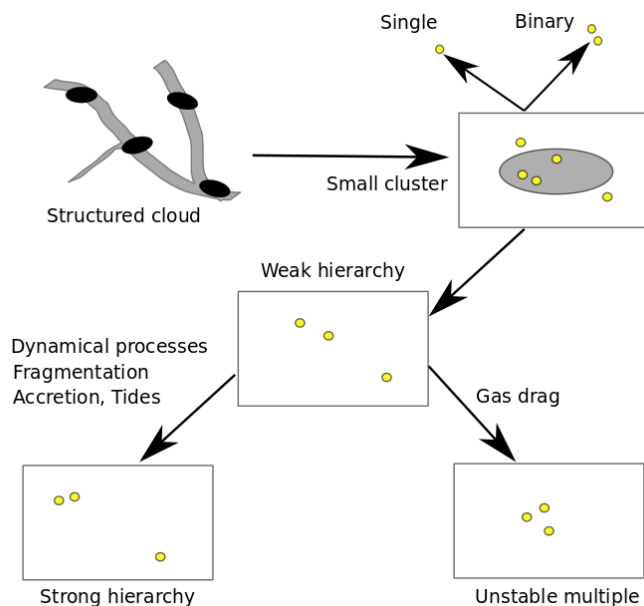


Figure 1.2: Scenario of multiple star formation. Credit: Tokovinin (2004a).

2008). It was shown, that dynamical dissipation of stellar clusters leaves behind mostly single stars and just a minority of binary and multiple systems (Goodwin and Kroupa, 2005). However, other mechanisms for quadruple formation were suggested. The most promising of these mechanisms are as follows.

### 1.1.1 Rotationally driven fragmentation

The first promising scenario for quadruple system formation is the rotationally driven fragmentation. In this scenario two binaries are formed in the collapsing interstellar gas with initial separation roughly  $10^2 - 10^4$  a.u. They interact with the remnants of the surrounding gas, create spiral waves and transfer their angular momentum outwards, becoming tighter and tighter. This process naturally produces quadruple stars consisting of two binaries.

### 1.1.2 Migration due to gas accretion

The second scenario is migration of the orbits as a result of accretion of gas to binary, with consequent increase of the mass ratio, and associated braking by the massive circum-binary disc. This scenario might consist of two separate mechanisms: accretion induced migration, which acts on larger scales and a second migration, not associated with accretion, which shortens inner orbital periods. All in all, the outer orbit shrinks by accretion from the envelope, while the gas accreted in the inner binaries inherits its angular momentum and shrinks the inner orbits.

## Chapter 2

# Secular orbital changes

As the main topic of this thesis is to determine secular orbital changes of quadruple system VW LMi, herewith we introduce the definition and physical background of secular orbital changes. Secular orbital changes, or secular perturbations, are defined as long term phase average evolutions on timescales much longer than the orbital periods of system's subsystems (Naoz, 2016). As secular timescales are longer than the orbital periods, motions of the individual components could be averaged over their orbits. Therefore, only secular changes of the orbital elements should be studied (Antognini, 2015). Obviously, contemplating secular perturbations has sense for stellar systems with at least three components - triples. In case of a triple stellar system, the system is decomposed to a binary system and its stellar companion bound by gravitational force. As theories and observations confirm, the companion orbiting around the binary system causes secular perturbations in the orbit of the binary. This topic in case of gravitationally bound triple systems has already been studied by Lagrange, Laplace or Poincare.

More detailed studies of hierarchical triple systems were published by Lidov (1962) and Kozai (1962). Lidov (1962) focused on the evolution of orbits of artificial satellites in the Solar system due to perturbations from outer potential. Kozai (1962) published a study, where he discussed the effect of Jupiter's gravitational perturbations on a highly inclined asteroid orbits. We note, that hereafter the semi-major axis of the inner orbit is noted as  $a_{in}$ , whilst the semimajor axis of the outer orbit is denoted as  $a_{out}$ . The total energies of the inner orbits, as well as the total energy of the outer orbit are conserved separately, which implies that  $a_{in}$  and  $a_{out}$  are constants during evolution. The presence of the secular perturbations is due to the exchange of the angular momentum between the inner and outer orbits. Kozai's method was to expand the three-body Hamiltonian in parameter  $\alpha$ , which is the ratio  $a_{in}/a_{out}$ , average through whole orbit and truncate the expression to lowest possible (quadruple) order, which is proportional to  $(a_{in}/a_{out})^2$

(Naoz, 2016). Both Kozai (1962) and Lidov (1962) found out that large eccentricity and inclination oscillations are present in such system's inner orbits and that most of the angular momentum is carried by the third (outer) perturber. Also, assuming axisymmetric outer potential, the z-components of the angular momenta vectors of both inner and outer orbits are conserved quantities. Majority of the further studies of the Kozai-Lidov effect used the stated quadrupole level approximation. However, the quadrupole approximation has its boundaries as secular perturbations manifest only for initially highly inclined inner and outer orbits ( $\sim 40^\circ - 140^\circ$ ). Also, this approximation could be applied in the special case of circular outer orbit, therefore it is not suitable for more eccentric systems. As Naoz et al. (2011) showed that neglecting the boundaries of the quadrupole approximation leads to different dynamical evolution of a multiple system.

The study of Kozai-Lidov effect re-emerged towards the end of the century as peculiar systems were discovered, such as the discovery of a highly eccentric exoplanet 6 Cyg B (Cochran et al., 1996) or the study of almost perpendicular system Algol (Eggleton et al., 1998). It was obvious, that higher order approximation would be needed to overcome the limitations of the quadrupole approximation. The solution was to truncate the expanded three-body Hamiltonian series to octupole order, proportional to  $(a_{in}/a_{out})^3$ . Using this approximation allows inner orbit eccentricity reach extraordinary high and uncertain values, because the whole system becomes more chaotic at all (Ford et al., 2000). What is more important, the inclination of the inner orbit could change up to value of  $\pi/2$ , which means that the orientation of the orbit could flip from prograde to retrograde with respect to the angular momentum (Naoz et al., 2011). The described process with exceptionally high eccentricities and orbital flips is called the eccentric Kozai-Lidov effect. This mechanism results in far more interesting dynamical evolution of a multiple systems. However, the effect does not occur in systems where the components of the inner sub-system have comparable masses, mass loss from whichever component could induce the eccentric oscillations (Antognini, 2015).

## 2.1 The Kozai-Lidov effect

In this section the theoretical basis of the Kozai-Lidov effect will be derived. Firstly derived by Lidov (1962) and Kozai (1962), the quadrupole order approximation was derived afterwards by many other authors. Hereby, the timescale of Kozai-Lidov effect and the time evolution equations of the orbital elements will be derived. The derivation is based and closely follows the works of Harrington (1968), Naoz (2016), Ford et al. (2000) and Antognini (2015).

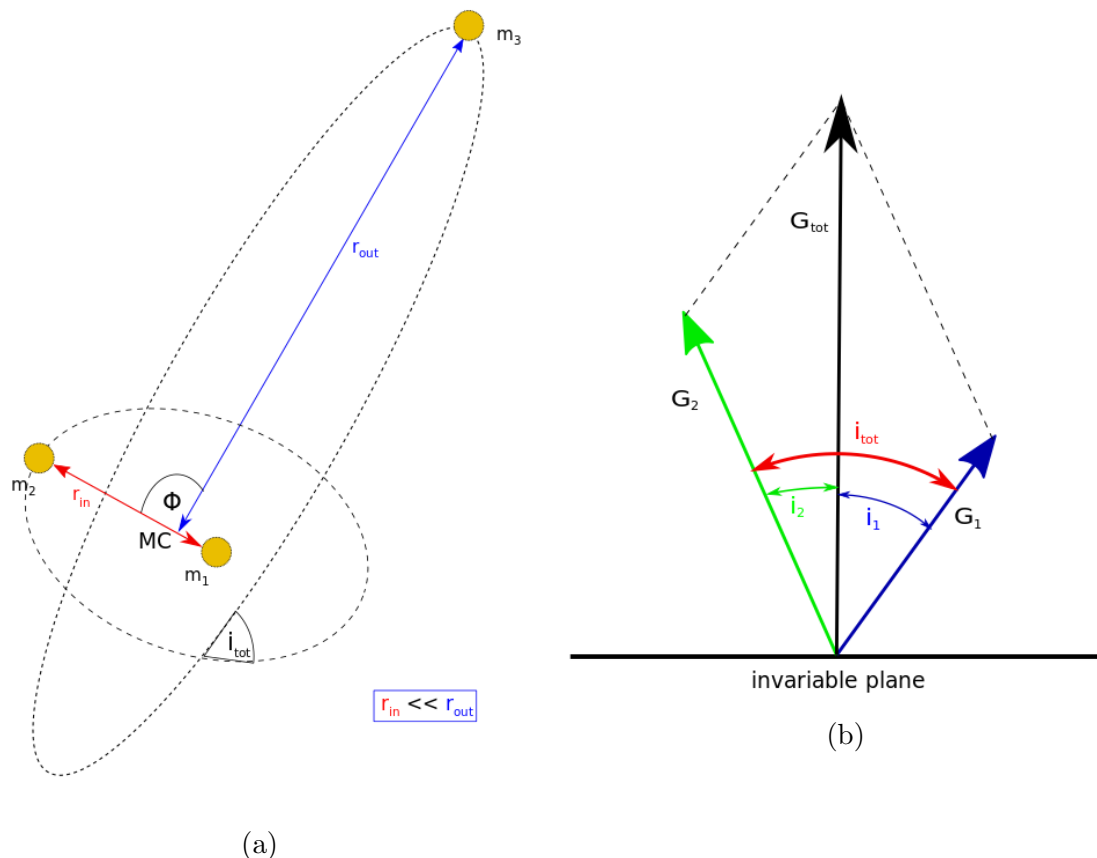


Figure 2.1: Cartoon of the three-body perturbation problem. (a) Spatial scheme of the inner and outer orbit. MC denotes mass center of the inner orbit.  $r_{in}$  and  $r_{out}$  are the state vectors, while  $\Phi$  is the angle between them. (b) The angular momenta  $G$  and inclinations. The invariable plane is perpendicular to  $G_{tot}$ .

The scheme of the three-body problem is illustrated on Figure 2.1a. A tight binary and a distant third companion form the triple hierarchy. As it is a hierarchical system, we can divide the motion to two separate Keplerian orbits: denoted as inner (tight binary) and outer (mass center of tight binary and the third body). The inner system is formed by bodies of mass  $m_1$  and  $m_2$ ,  $r_{in}$  is the relative position vector from  $m_1$  to  $m_2$ . The third body has mass  $m_3$  and  $r_{out}$  is the relative position vector from the mass center of the inner binary to  $m_3$ . We will describe the system using Hamiltonian formalism. The Hamiltonian of the given system consists of the Hamiltonians of the inner and outer orbit and the perturbed Hamiltonian, which represents their mutual interaction. The coupling term in the Hamiltonian is rewritten as a power series in the ratio of the semi-major axes  $\alpha = a_{in}/a_{out}$ . The described Hamiltonian as published by Harrington (1968) is given in Equations 2.1 and 2.2.

$$\mathcal{H} = \frac{k^2 m_1 m_2}{2a_{in}} + \frac{k^2 m_3 (m_1 + m_2)}{2a_{out}} + \mathcal{H}_{pert} \quad (2.1)$$

$$\mathcal{H} = \frac{k^2 m_1 m_2}{2a_{in}} + \frac{k^2 m_3 (m_1 + m_2)}{2a_{out}} + \frac{k^2}{r_2} \sum_{n=2}^{\infty} \left( \frac{r_{in}}{r_{out}} \right)^n M_n P_n(\cos \Phi) \quad (2.2)$$

Here  $k^2$  is the gravitational constant,  $P_n$  are Legendre polynomials,  $\Phi$  is the angle between  $r_{in}$  and  $r_{out}$ .  $M_n$  is the mass parameter:

$$M_n = m_1 m_2 m_3 \frac{m_1^{n-1} - (-m_2)^{n-1}}{(m_1 + m_2)^n}. \quad (2.3)$$

The reference frame of the system is the invariable plane, perpendicular to  $z$  axis along the total angular momentum of the system, which is a conserved quantity during the whole secular evolution, see Figure 2.1b. Adopting canonical Delaunay's elements, every orbit could be described via three sets of angles ( $M, \omega, \Omega$ ) and their three conjugate momenta ( $L, G, H$ ). Afterwards we will change the notation of the latter angles to frequent notation ( $M, \omega, \Omega$ )  $\rightarrow$  ( $l, g, h$ ). The first angles are the mean anomalies  $M_{in}$  and  $M_{out}$ , their conjugate momenta  $L_{in}, L_{out}$  are as follows:

$$\begin{aligned} L_{in} &= \frac{m_1 m_2}{m_1 + m_2} \sqrt{k^2 (m_1 + m_2) a_{in}}, \\ L_{out} &= \frac{m_3 (m_1 m_2)}{m_1 + m_2 + m_3} \sqrt{k^2 (m_1 + m_2 + m_3) a_{out}}. \end{aligned} \quad (2.4)$$

The second angles are the arguments of periastron  $\omega_{in}$  and  $\omega_{out}$ , their conjugate momenta  $G_{in}, G_{out}$  are as follows:

$$\begin{aligned} G_{in} &= L_{in} \sqrt{1 - e_{in}^2}, \\ G_{out} &= L_{out} \sqrt{1 - e_{out}^2}. \end{aligned} \quad (2.5)$$

Where  $e_{in}$  and  $e_{out}$  are the inner and outer orbit's eccentricities. The third angles are the longitudes of ascending nodes  $\Omega_{in}$  and  $\Omega_{out}$ . Noting that  $i_{in}$  and  $i_{out}$  are the inclinations of the inner and outer orbits, the conjugate momenta  $H_{in}$  and  $H_{out}$  of the ascending nodes are:

$$\begin{aligned} H_{in} &= G_{in} \cos(i_{in}), \\ H_{out} &= G_{out} \cos(i_{out}). \end{aligned} \quad (2.6)$$

Perceive that  $G_{in}$  and  $G_{out}$  are the magnitudes of angular momentum vectors  $\mathbf{G}_{in}$  and  $\mathbf{G}_{out}$ , while  $H_{in}$  and  $H_{out}$  are the  $z$ -components of these vectors. The configuration of these vectors is shown in Figure 2.1b. Considering the conservation of total angular momentum, we get the relation between the  $z$ -component of angular momenta and the total angular momentum magnitude:

$$G_{tot} = H_{in} + H_{out}. \quad (2.7)$$

Now, the equations of motion are represented by the following canonical relations:

$$\frac{dL_j}{dt} = \frac{\partial \mathcal{H}}{\partial l_j}, \quad \frac{dl_j}{dt} = \frac{\partial \mathcal{H}}{\partial L_j}, \quad (2.8)$$

$$\frac{dG_j}{dt} = \frac{\partial \mathcal{H}}{\partial g_j}, \quad \frac{dg_j}{dt} = \frac{\partial \mathcal{H}}{\partial G_j}, \quad (2.9)$$

$$\frac{dH_j}{dt} = \frac{\partial \mathcal{H}}{\partial h_j}, \quad \frac{dh_j}{dt} = \frac{\partial \mathcal{H}}{\partial H_j}, \quad (2.10)$$

where  $j = 1, 2$  denotes the canonical relations to have opposite sign, because of the chosen sign convention for this Hamiltonian. If the semi-major axis ratio  $\alpha$  is a small parameter, then in the zeroth approximation each orbit is a Keplerian orbit with conserved total energy. Averaging the equations of motion on short timescales allows us to look on the long-term orbital dynamics of the system. In this, so-called secular approximation the energies and semi-major axes of orbits are conserved quantities and angular momentum exchange between the orbits takes place. Eliminating short-term orbital changes is done via Von Zeipel transformation (Brouwer, 1959) and the whole process is described in (Naoz et al., 2011). In the final secular approximation and generally for systems without non-gravitational effects, two quantities are conserved: the energies (and semi-major axes) and the total angular momentum  $G_{tot}$ . Now, the time evolution of eccentricities and inclinations could be obtained from the equations of motion 2.8, 2.9, 2.10:

$$\frac{de_j}{dt} = \frac{\partial e_j}{\partial G_j} \frac{\partial \mathcal{H}}{\partial g_j}, \quad (2.11)$$

$$\frac{d \cos(i_j)}{dt} = \frac{\dot{H}_j}{G_j} - \frac{\dot{G}_j}{G_j} \cos(i_j). \quad (2.12)$$

Here  $j = 1, 2$  denotes the inner and the outer orbit, respectively. The quadrupole approximation is the lowest order approximation and is proportional to  $(\alpha)^2$ . As a result of the Von Zeipel transformation, the outer orbit's angular momentum  $G_{out}$  remains a constant quantity. As a consequence, the quadrupole order approximation should be used only for circular outer orbits (axisymmetric potential). Considering the inner orbit, as the energy and the z-component of the angular momentum  $H_{in}$  are preserved, it's Hamiltonian does not depend on the longitude of ascending node and the system is integrable. The precession rate of the inner orbit's ascending node  $\Omega_{in}$  and the longitude of periapsis  $\omega_{in}$  causes large amplitude oscillations between the eccentricity and the inclination within the inner orbit.

Considering circular outer orbit and an inner test particle, while  $m_2 \rightarrow 0$ , following the derivation of Lithwick and Naoz (2011), the Hamiltonian of the three-body system is as follows

$$\mathcal{H} = \frac{3}{8}k^2 \frac{m_1 m_2}{a_{out}} \left( \frac{a_{in}}{a_{out}} \right)^2 \frac{1}{(1 - e_{out}^2)^{3/2}} F_{quad}, \quad (2.13)$$

where  $F_{quad}$  is as follows:

$$F_{quad} = -\frac{e_{in}^2}{2} + \theta^2 + \frac{3}{2}e_{in}^2 \theta^2 + \frac{5}{2}e_{in}^2 (1 - \theta^2) \cos(2\omega_{in}), \quad (2.14)$$

where  $\theta = \cos(i_{tot})$ . At this alignment the inner orbit angular momentum along the z axis with  $j_{z,in}$  being its specific z component and  $\theta$  is conserved:

$$H_{in} \propto j_{z,in} = \sqrt{1 - e_{in}^2} \cos(i_{tot}) = const., \quad (2.15)$$

$$\theta = \cos(i_{tot}) = const.$$

As  $H_{in}$  and  $F_{quad}$  are both conserved, we define the following constant defined by initial conditions of the system:

$$C_{KL} = \frac{F_{quad}}{2} - \frac{1}{2}j_{z,in}^2 = e^2 \left( 1 - \frac{5}{2} \sin(i_{tot}^2) \sin(\omega_{in}^2) \right). \quad (2.16)$$

As  $j_{z,in}$  is conserved:

$$j_{z,in} = \sqrt{1 - e_{in,max/min}^2} \cos(i_{in,min/max}) = \sqrt{1 - e_{in,0}^2} \cos(i_{in,0}). \quad (2.17)$$

Setting initial conditions as  $e_{in,0} = 0$  and  $\omega_{in,0} = 0$  we obtain the minimal eccentricity and maximal inclination (and vice versa) a multiple system must reach to manifest secular orbital perturbations:

$$e_{max} = \sqrt{1 - \frac{5}{3} \cos^2(i_0)}, \quad (2.18)$$

$$\cos(i_{min}) = \pm \sqrt{\frac{3}{5}}. \quad (2.19)$$

Equation 2.19 yields to extremal values  $i_{min} = 39.2^\circ$  and  $i_{min} = 140.77^\circ$ . These angles are called Kozai angles and they represent the limit angle between the inner and outer orbit where eccentricity and inclination oscillations are present.

From the more general point of view, if we do not consider a test particle in the inner orbit, we obtain the Hamiltonian of the system in the form:

$$\mathcal{H}_{quad} = C_2 \{ (2 + 3e_{in}^2)(3 \cos^2(i_{tot}) - 1) + 15e_{in}^2 \sin^2(i_{tot}) \cos(2\omega_{in}) \}, \quad (2.20)$$

where the constant  $C_2$  is defined as:

$$C_2 = \frac{k^4}{16} \frac{(m_1 + m_2)^7}{(m_1 + m_2 + m_3)^3} \frac{m_3^7}{(m_1 m_2)^3} \frac{L_{in}^4}{L_{out}^3 G_{out}^3}. \quad (2.21)$$

Using this general approximation, the minimal eccentricity and maximal inclination values of the inner orbit could be obtained from the conservation of total angular momentum  $G_{tot} = G_{in} + G_{out}$ :

$$G_{tot}^2 - G_{out}^2 = L_{in}^2(1 - e_{in}^2) + 2L_{in}L_{out}\sqrt{1 - e_{in}^2}\sqrt{1 - e_{out}^2}\cos(i_{tot}), \quad (2.22)$$

and from the conservation of energy, for the minimal eccentricity and maximal inclination (or vice versa), setting  $\omega_{in} = 0$  we could write:

$$\frac{\mathcal{H}_{quad}}{2C_2} = 3\cos^2(i_{tot,max})(1 - e_{in,min}^2) - 1 + 6e_{in,min}^2. \quad (2.23)$$

However, the extremal values of inclination could not be determined generally, just for a given sets of initial conditions.

Considering circular outer orbit, a typical timescale of the secular orbital perturbations of eccentricity and inclination could be determined. The timescale is given by relation  $t_{quad} = G_{in}/C_2$ . Integrating this relation between the minimal and maximal eccentricity yields to result of Antognini (2015):

$$\begin{aligned} t_{quad} &\sim \frac{16 a_{out}^3 (1 - e_{out}^2)^{3/2} \sqrt{m_1 + m_2}}{15 a_{in}^{3/2} m_3 k} \\ &= \frac{16}{30\pi} \frac{m_1 + m_2 + m_3}{m_3} \frac{P_{out}^2}{P_{in}} (1 - e_{out}^2)^{3/2}. \end{aligned} \quad (2.24)$$

Summing the presented nature of the Kozai-Lidov effect, we can see, that the conservation of the z-component of the angular momentum results in oscillations between inner orbit's eccentricity and inclination. The inner orbit becomes more eccentric for lower inclination and vice versa as shown on Figure 2.2.

## 2.2 The eccentric Kozai-Lidov effect

If the outer orbit in a hierarchical three-body system has non-zero eccentricity the Hamiltonian in Equation 2.1 requires the next-level, so called octupole approximation, which is proportional to  $\alpha^3$  as non-zero eccentricity leads to changes of the orbital parameters of the outer orbit (that are much slower than the Kozai-Lidov oscillation timescales in the inner orbit). In this approximation the inner orbit's inclination could

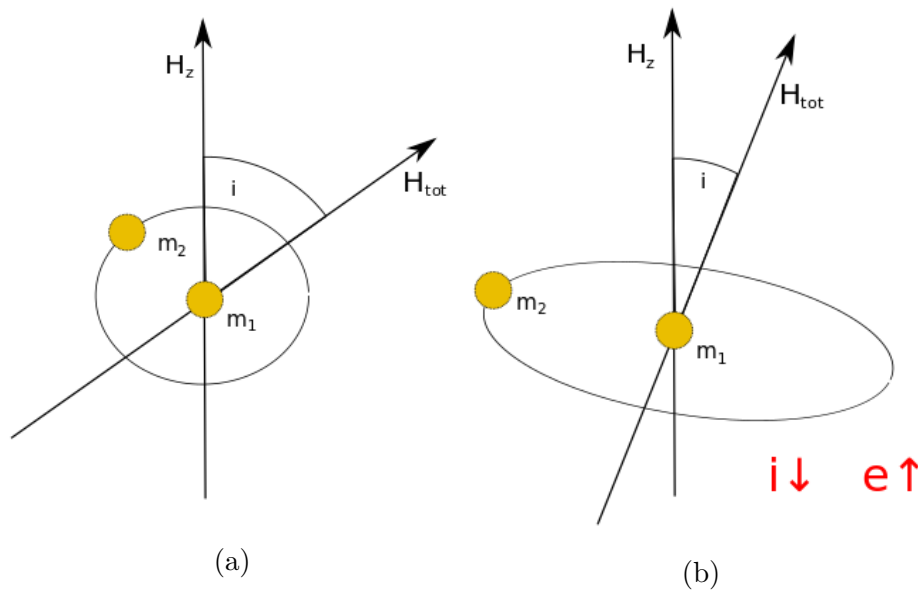


Figure 2.2: Cartoon of the consequence of the Kozai-Lidov effect. As the eccentricity in the inner orbit rises, the inclination decreases.

surpass the value of  $\pi/2$  and therefore, it could flip its orientation from prograde to retrograde. As a consequence, the inner orbit's eccentricity could reach very high and not well defined values, as the whole system becomes more chaotic. The mechanism is applicable for far more stellar systems as the quadrupole Kozai-Lidov one. It allows to study eccentric orbits such as exoplanetary orbits, black hole dynamics and higher multiplicity stellar systems. The eccentric Kozai-Lidov effect leads to higher order resonances in general, characterised by eccentricity excitations and orbit flips, which lead to chaotic behavior of the whole system at all. In addition, short range forces and stellar mass-loss could trigger the eccentric Kozai-Lidov effect, what is an important consequence in the case of contact binary systems (Naoz et al., 2011). However, in case of VW LMi both the eccentricity of the detached orbit and the mutual orbit are smaller than 0.1, therefore the eccentric Kozai-Lidov effect could not be the effect that causes secular orbital changes in this quadruple system. The Kozai-Lidov effect is important at the formation of tight binary systems. These systems can not form in proto-stellar gas clouds without the Kozai-Lidov effect. As a consequence, the inner binaries of loose triple systems in gas clouds transfer their angular momenta to their outer (third) companions, and eventually the binary systems become more tighter and hierarchic. Considering, that the orbital period of the inner binary is less than ten days, the effect of magnetic braking grows and causes further angular momentum losses, which implies formation of a contact binary system (Pribulla and Rucinski, 2006).

## 2.3 Kozai-Lidov effect in quadruple systems

The Kozai-Lidov effect was immensely studied in the lowest possible order of stellar multiplicity - hierarchical triple systems. In this case, the third component of the system, which is markedly distant from the tight inner binary system  $a_{out} \gg a_{in}$ , causes secular orbital changes in the inner orbit. Assuming non-zero eccentricity of the outer orbit, secular changes in the outer orbit could occur, too. In this section we consider the presence of secular perturbations in higher-order hierarchical multiple systems. It was stated in Chapter 1 that hierarchical multiple systems could be divided into smaller nested sub-systems. Further, each of the nested sub-systems could be treated as a Keplerian orbit. Considering this actuality, in theory any multiple stellar system could be divided into some sort of triple system and studied for the presence of Kozai-Lidov secular orbital perturbations. However, as we saw the complexity of the approximation of secular orbital perturbations in Section 2.1 for triple stellar systems, for higher-order multiplicity even more complicated analytical solutions are expected. As the aim of this thesis is to determine secular orbital changes of a hierarchical quadruple, the application of Kozai-Lidov effect on hierarchical quadruples will be presented.

The Kozai-Lidov effect in quadruple systems was not studied previously, until the research of Pejcha et al. (2013). In (Pejcha et al., 2013) considered hierarchical quadruple systems composed of two binaries, where each binary acts as a distant third perturber on the other, thus allowing to apply the analytical approximation of the three-body Kozai-Lidov effect. However, the problem is more complex as the distant third perturber is not a point mass, indeed two separate bodies orbiting each other. This setting causes secular orbital perturbations in both inner and outer orbits. Therefore quadruple systems exhibit new dynamics related to Kozai-Lidov cycles. The work of Pejcha et al. (2013) exposed, that quadruple's dynamics qualitatively and quantitatively differs from the dynamics of triple systems. In quadruple systems, close encounters and further collisions of stars occur more frequently. The aftermath of close encounters or collisions by which binaries merge into single stars is that quadruple systems often dissipate into single rogue stars and triple systems. Dissipation could explain the lesser count of quadruple systems compared to triple systems, what is consistent with the Multiple Stellar Catalog (Tokovinin, 2008, 2018). For that reason, the lower frequency of quadruples may be the result of a presence of much stronger and efficient Kozai-Lidov effect in these systems. These results imply important applications of Kozai-Lidov effect in quadruple systems such as the explanation of the origin of close binaries and blue stragglers on a wide mutual orbit (Perets and Fabrycky, 2009) or the origins of cataclismic mergers of white dwarfs orbiting close binary systems (Soker and Tylenda, 2006). Considering a quadruple system, which consists of two white

dwarves on a close binary orbit and a distant binary star perturber, the two white dwarves could merge due to Kozai-Lidov effect, thus creating type Ia supernova (Benz et al., 1989). There are much more applications in case of quadruple systems as there are no restrictions on the inclination of the perturbing body as in the case of triple systems (Katz and Dong, 2012).

The analytic solution for quadruple systems consisting of two binary systems was formulated by Vokrouhlický (2016). The results show, that unless the system is very compact, a quadruple system could be perceived as two triple system in superposition with gravitational effects on each other. The typical timescale of secular orbital changes in quadruple systems as showed in (Vokrouhlický, 2016) and (Pejcha et al., 2013) is as follows:

$$t_k = \frac{2}{3\pi} \left( \frac{a_A(1 - e_{AB}^2)}{a_B} \right)^{3/2} \left( \frac{a_{AB}}{a_A} \right)^3 P_B. \quad (2.25)$$

Here, as a quadruple system was considered, different notation was used:  $A$  denotes parameters of one binary system, while  $B$  denotes the parameters of the second one.  $AB$  denotes the orbital parameters of the shared mutual orbit of two binaries. This typical timescale, also called as the Kozai unit gives us a useful estimation of secular perturbation's duration, thus allows us to precisely set the run-times of further numerical integrations of studied systems. Integration run-times are generally set as the multiples of the system's Kozai unit, which could be directly determined from observed orbital parameters. Vokrouhlický (2016) tested his solutions on various well observed quadruple systems as V994 Her, V379 Cep and even VW LMi. Results on VW LMi showed, that pericentre of the non-eclipsing binary could drift by roughly  $3^\circ yr^{-1}$  due to gravitational interaction with the eclipsing binary system. As a part of this thesis, we will provide further examination of this drift. Using numerical integrator, we would probe VW LMi's secular orbital changes over a period of multiple Kozai units of the stellar system, see Equation 2.25.

## 2.4 Empirical stability limit

All multiple systems with well defined orbits are dynamically stable (Tokovinin, 2008) and the eccentricities of the outer orbits obey an empirical stability limit

$$\frac{P_{out}(1 - e_{out})^3}{P_{in}} > 5. \quad (2.26)$$

Based on statistics on the Tokovinin's Multiple Stellar Catalog, an important empirical ratio arises:

$$\frac{P_{out}}{P_{in}} > 5, \quad (2.27)$$

where  $P_{out}$  is the period of the mutual wide orbit and  $P_{in}$  is the period of the particular inner orbit. This ratio could be comprehended as a stability limit of a stellar system. Systems whose values of period ratios are higher than five appear to be dynamically stable as shown on Figure 2.3.

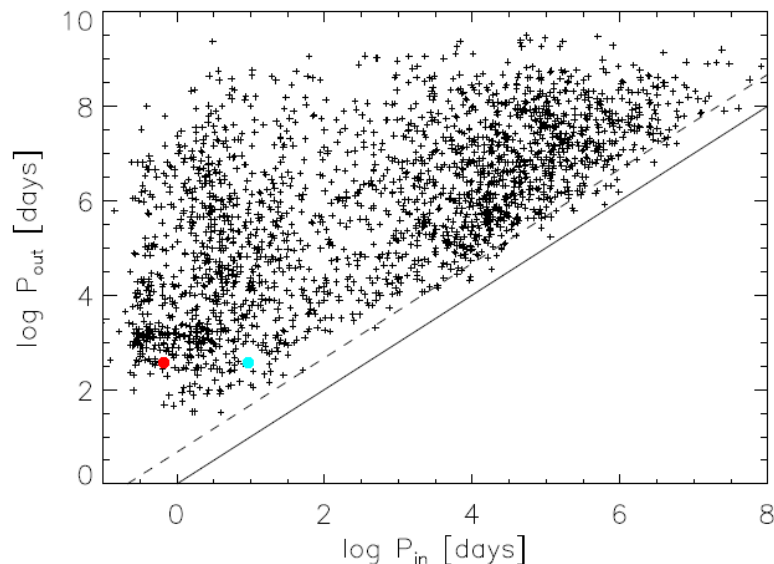


Figure 2.3: The relation between the inner and outer period for all physical multiple system in Multiple Stellar Catalog. Full line represents equality, dashed line represents value  $P_{out}/P_{in} = 5$ . Red dot represents the contact binary and the blue dot the detached binary of VW LMi. Credit: Tokovinin (2018).

As we see, almost all known multiple stellar systems lay above this limit. In Figure 2.3 we can see some multiple systems laying in between values 0 and 5. It must not necessarily mean that these systems are dynamically unstable. Most probably, this is a result of a selection effect: these systems could be parts of higher-order multiple systems (with period ratios obeying the empirical stability limit), which were not discovered yet. Discovering higher-order hierarchies requires combination of various observation techniques (photometry, spectroscopy, interferometry). A marked example is VW LMi. VW LMi was classified as an W UMA-type eclipsing binary after the discovery of photometric variability by Hipparcos mission in 1997. Long-term spectroscopy (Pribulla et al., 2006) showed that VW LMi is a quadruple system consisting of a contact eclipsing binary and a non-eclipsing binary. As stated in (Tokovinin, 2004b) all stellar systems with well-defined orbits are dynamically stable systems. Possible explanation is, that dynamically unstable systems such as trapezia, see Chapter 1,

dissipate quite rapidly, therefore it is not possible to define their orbital elements precisely or on the other hand, they just dissipated a long time ago and they do not form a multiple system at the time. Thus, based on statistics we can say, that if we observe a stellar system and determine its orbital parameters precisely, the stellar system will be, with a high probability, dynamically stable. Comparing Equation 2.27 with the typical timescale of Kozai-Lidov oscillations, Equation 2.24, we can see a direct restraint between the empirical stability limit and the Kozai-Lidov effect. The ratio is also tied with the probability of secular orbital changes (Kiseleva et al., 1998). Applying Kepler's third law on Equation 2.27 we get the ratio of outer and inner semi-major axes. Thus, we can see the tightness of the system. If the ratio of semi-major axes (and therefore orbital periods) is small, the multiple system's components are at close mutual distances and they behave dynamically unstable. However, if the component's separation high enough, the system remains stable and Kozai-Lidov oscillations reveal on timescales longer than the timescales of the orbital periods. All these empirical and analytic results imply, that the period ratio is an important parameter in the field of study of multiple stellar systems as it reveals the system's stability and the presence of secular orbital changes.

## Chapter 3

# Presenting VW LMi

VW LMi is a spectral type F3-5V hierarchical quadruple with 8.0 maximal visual magnitude (Pribulla et al., 2006). Its photometric variability with period 0.477547 days was found by Hipparcos mission in 1997. It was classified as a W UMa - type eclipsing binary. This type of system consists of a contact binary with a common envelope and a characteristic strong tidal distortion is present (Ruciński, 1973). First ground based photometric measurements of the contact binary were performed in 1999 and 2000 by Dumitrescu (2000). Later analysis of light curves and determination of system's parameters (Dumitrescu, 2003) proved that the system is a contact binary. BV photometry and its analysis was presented in 2003 (Gomez-Forrellad et al., 2003), while Fourier analysis of Hipparcos light curve was presented in 2004 (Selam, 2004).

Long-term spectroscopy (1998-2005) by Pribulla et al. (2008) showed the presence of a second non-eclipsing binary system. Thereafter VW LMi was classified as a spectroscopic hierarchical quadruple <sup>1</sup>. However, it was shown, that a nearby star HD95606 forms a loose binary with the quadruple system. Its separation and gravitational effect is such minimal, that from the view of the dynamics of the quadruple system it could be neglected. The periods of the three orbits were determined: contact eclipsing binary with period  $P_{12} = 0.4775$  days, non-eclipsing binary with period  $P_{34} = 7.93$  days, both systems on a tight, 355 days long period mutual orbit. The masses of all four components as well as the light-time effect (LITE) due to mutual revolution were also determined. New photometric elements of VW LMi were obtained by Sánchez-Bajo and Garcia-Melendo (2007).

With its shortest mutual period, VW LMi is the tightest quadruple system ever discovered (Tokovinin, 2008). The short mutual period is a key parameter of this thesis. As was shown in Section 2.4, the ratio of the outer (mutual) orbital period and inner

---

<sup>1</sup>Notation: Indexes 1,2 - parameters of the eclipsing binary. Indexes 3,4 - parameters of the detached binary.

orbital periods is an important parameter - the value of this fraction is tied to the probability of secular orbital changes in multiple stellar systems. In the discussed system the ratio of outer period  $P_{1234}$  and inner non-eclipsing period  $P_{34}$  is equal to 44.5. Since systems with outer/inner period ratio higher than five are dynamically stable and have high probability of secular orbital changes as a consequence of mutual gravitational interactions (Kiseleva et al., 1998), we expect that secular orbit changes on timescales as short as decades are present in this hierarchical system. Since the components tight maximal angular separation (10 mas) (Pribulla et al., 2006), observational determination of the system's parameters would be possible by interferometric method. However, as we could not acquire interferometric observational time to observe VW LMi, photometric and spectroscopic observations will be used to determine the systems orbital parameters.

VW LMi		
GSC	2519-2347	
HD	95660	
HIP	54003	
$\mu_\alpha$ [mas.yr <sup>-1</sup> ]	13.303(0.120)	(Gaia Collaboration et al., 2018)
$\mu_\delta$ [mas.yr <sup>-1</sup> ]	-6.083(0.166)	(Gaia Collaboration et al., 2018)
RV [km.s <sup>-1</sup> ]	-0.15(25)	(Pribulla et al., 2008)
$\pi$ [mas]	9.0488(0.12)	(Gaia Collaboration et al., 2018)
$V_{max}$	8.0003(0.0123)	(Gaia Collaboration et al., 2018)
$(B - V)$	0.340(21)	(Hog et al., 2000)
$(J - K)$	0.208(30)	(Skrutskie et al., 2006)
$T_{eff}$ [K]	6506.0	(Gaia Collaboration et al., 2018)
sp. type	F3 - 5V	(Pribulla et al., 2006)

Table 3.1: Parameters of the variable VW LMi. The last column shows the source of parameters.

### 3.1 Orbital parameters of VW LMi

In this section we present the known parameters of VW LMi. Secular orbital perturbations are contemplated in the system, therefore it is important to state the orbital parameters from the older observations to compare them with the new orbital parameters obtained in this thesis. First of all, in Table 3.1 we present the observational parameters of VW LMi obtained from various sources - from David Dunlap Observatory (Pribulla et al., 2008) Tycho-2 Catalog (Hog et al., 2000), 2MASS (Skrutskie et al.,

2006) and from the most recent GAIA data release (Gaia Collaboration et al., 2018). Secondly and most importantly, the spectroscopic orbital parameters by (Pribulla et al., 2008) determined by simultaneous fit to observed radial velocities of both binaries and times of minima of the eclipsing pair. The spectroscopic orbital parameters of (Pribulla et al., 2008) will be crucial as the same processing techniques will be applied in this thesis, therefore these parameters would serve as comparison to newly-determined orbital parameters.

<b>Contact binary</b>		<b>Detached binary</b>	
$P_{12}$ [days]	0.47755106(3)	$P_{34}$ [days]	7.93063(3)
$Q$ [days]	$1.63(9) 10^{-10}$	$e_{34}$	0.035(3)
$T_{12}$ [HJD]	2,452,500.1467(2)	$T_{34}$ [HJD]	2,452,274.54(11)
$K_1$ [km.s <sup>-1</sup> ]	105.8(1.0)	$K_3$ [km.s <sup>-1</sup> ]	63.99(23)
$K_2$ [km.s <sup>-1</sup> ]	250.2(1.2)	$K_4$ [km.s <sup>-1</sup> ]	65.53(27)
$M_{12} \sin^3 i_{12}$ [ $M_\odot$ ]	2.231(23)	$M_{34} \sin^3 i_{34}$ [ $M_\odot$ ]	1.785(11)
$i_{12}$ [deg]	79.0	$i_{34}$ [deg]	68.9(1.5)
$M_1$ [ $M_\odot$ ]	1.66	$M_3$ [ $M_\odot$ ]	1.11
$M_2$ [ $M_\odot$ ]	0.70	$M_4$ [ $M_\odot$ ]	1.09
$\chi_\nu^2$ (RV1)	1.086	$\omega_{34}$ [rad]	1.90(9)
$\chi_\nu^2$ (RV2)	1.058	$\chi_\nu^2$ (RV3)	0.862
$\chi_\nu^2$ (MIN)	1.086	$\chi_\nu^2$ (RV4)	0.851
<b>Mutual wide orbit</b>			
	$P_{1234}$ [days]		355.02(17)
	$e_{1234}$		0.097(11)
	$T_{1234}$ [HJD]		2,456,046(6)
	$K_{12}$ [km.s <sup>-1</sup> ]		21.61(49)
	$K_{34}$ [km.s <sup>-1</sup> ]		23.22(33)
	$M_{1234} \sin^3 i_{1234}$ [ $M_\odot$ ]		3.32(10)
	$i_{12}$ [deg]		64.1(4.2)
	$M_{1234}$ [ $M_\odot$ ]		4.56(0.07)
	$\omega_{1234}$ [rad]		2.20(12)
	$V_0$ [km.s <sup>-1</sup> ]		-0.15(25)

Table 3.2: Spectroscopic elements of VW LMi. Determined via simultaneous fit to radial velocities of both binaries and minima times of the eclipsing binary. The contact binary has a circular orbit. Explanation:  $P_j$ -orbital period,  $e_j$ - eccentricity,  $T_j$ -time of periastron passage in eccentric orbits, time of minimum light for the contact pair,  $K_j$ - spectroscopic half-amplitude,  $M_j \sin^3 i_j$ - projected mass,  $i_j$ - inclination,  $M_k$ -component mass,  $\omega_j$ - argument of periapsis,  $j \in (12, 34, 1234)$ ,  $k \in (1, 2, 3, 4)$ ,  $\chi^2$  are the reduced chi-squared tests. Standard errors are given in parentheses. The stated stellar masses and orbital inclinations are estimates. Credit: (Pribulla et al., 2008).

Physical and geometrical parameters of the components that could not be determined through spectroscopy, could be determined by a procedure used in (Pribulla et al., 2006). These parameters, namely the component’s masses and orbit’s inclinations were estimated in (Pribulla et al., 2008). We present these values in Table 3.2, however, these are estimates, not directly determined values.

### 3.2 Presence of secular orbital changes

As it was stated in Section 2.4, based on works of (Tokovinin, 2004b) and (Kiseleva et al., 1998), the empirical relation between the ratio of outer and inner orbital periods  $P_{out}/P_{in}$  serves as a useful tool to show, if the multiple system is stable and if there are present any secular orbital changes. In case of VW LMi, the ratio of orbital periods of the outer orbit and the orbit of the non-eclipsing binary is  $P_{1234}/P_{34} = 44.76$ , while the ratio of orbital periods of the outer orbit and the orbit of the contact binary is  $P_{1234}/P_{34} = 743$ . Therefore, we have the following consequences: as both period ratios are higher than the limit value five as stated in Equation 2.27, the system is dynamically stable and according to the timescale of Kozai-Lidov oscillations, visible secular orbital changes are expected on timescale of decades in case of the non-eclipsing binary and on scale of centuries in case of the contact binary system. On human timescales, only the secular changes of orbit of the non-eclipsing binary could be detected. However, long-term observations of VW LMi are available. Pribulla et al. (2008) compared the observations of the quadruple system for a decade 1998-2008. The values of important parameters of the non-eclipsing binary determined from various observations are shown in Table 3.3.

Year	1998	1999-2000	2002	2004-5	2007-8
HJD (2 400 000+)	50852-50960	51261-51673	52277-52391	53060-53836	53823-54650
$e_{34}$	0.032(6)	0.030(6)	0.032(5)	0.038(4)	0.039(4)
$\omega_{34}$ [rad]	1.43(19)	1.81(12)	2.04(15)	2.17(14)	2.18(9)
$K_3$ [km.s <sup>-1</sup> ]	63.69(37)	62.72(27)	65.00(39)	63.72(28)	63.59(34)
$K_4$ [km.s <sup>-1</sup> ]	65.67(42)	66.47(32)	65.51(43)	65.22(33)	65.79(39)

Table 3.3: Evolution of the non-eclipsing orbit. Standard errors of the last digit are given in parentheses. Credit: (Pribulla et al., 2008).

The important consequences of the results are:

- The eccentricity remains quite stable

- The semi-amplitudes remain stable within error, thus mutual orbit and non-eclipsing orbit are probably very close to coplanar
- There is a definite apsidal motion.

Further observations, which will expose the precise rate of the apsidal motion of the non-eclipsing binary system are provided in this thesis. For better view on the secular orbital changes of the quadruple system and to determine the changes in the orbit of the eclipsing binary, which could not been determined from observations yet, we will perform numerical integration of the quadruple system on a scale of multiple Kozai units to reveal the nature and timescales of secular changes in the quadruple system VW LMi.

## Chapter 4

# Numerical integration of orbits

In Chapter 1 it was stated, that hierarchical multiple systems consist of smaller nested sub-orbits which could be treated as Keplerian two-body problems. Using this approach, in Chapter 2 we showed the analytical solution of Kozai-Lidov effect for hierarchical triple systems. The solution is complex and not trivial. The analytical solution for hierarchical quadruple systems was outlined in Section 2.3. Coming out from the solution for triple systems, the solution for the quadruple systems becomes far more complex as seen in the publication of Vokrouhlický (2016). For this reason it is more convenient to study the motion of multiple stellar systems through numerical methods rather than looking for exact analytical solution. In this chapter we introduce the numerical integration procedures, which were used in this thesis. First of all, we introduce two basic approaches of finding the solution of perturbed orbital motions as published in (Danby, 1992).

### 4.1 Encke's Method

Encke's method comes up from the osculating orbit, an ideal Keplerian orbit unperturbed by other bodies. However, if there are any other perturbing bodies, the osculating orbit of our studied body will vary in time. Cartoon showing the basic geometry of Encke's method is show in Figure 4.1.

Let  $\mu = G(M + m)$  and  $\vec{F}$  to be the perturbing force. Considering the geometry shown in Figure 4.1, the equation for undisturbed motion (osculating orbit) is given by

$$\ddot{\vec{\rho}} + \mu \frac{\vec{\rho}}{\rho^3} = \vec{F}, \quad (4.1)$$

while the equation for the perturbed orbit is given by

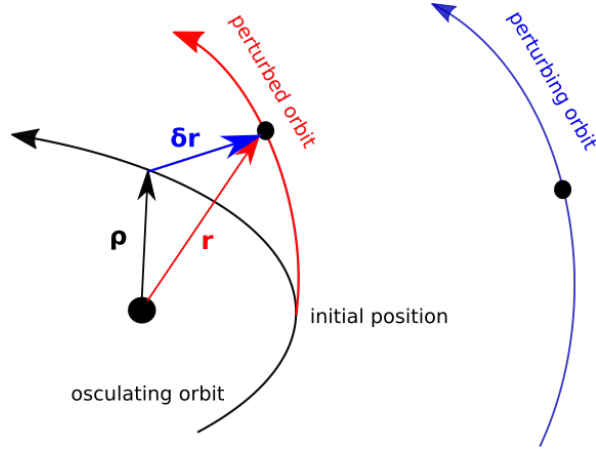


Figure 4.1: Cartoon showing the geometry of Encke's method.

$$\ddot{\vec{r}} + \mu \frac{\vec{r}}{r^3} = \vec{F}. \quad (4.2)$$

The difference from the osculating orbit  $\delta\vec{r}$  is given by

$$\delta\vec{r} = \vec{r} - \vec{\rho}, \quad (4.3)$$

thus we get the equation of motion

$$\frac{d^2}{dt^2} \delta\vec{r} = \vec{F} + \mu \left( \frac{\vec{\rho}}{\rho^3} - \frac{\vec{r}}{r^3} \right). \quad (4.4)$$

Equation 4.4 could be solved for  $\delta\vec{r}$  through numerical integration. The undisturbed orbit's equation of motion 4.1 could be easily solved as a Keplerian two-body problem. Thus, with  $\delta\vec{r}$  and  $\vec{\rho}$  solved, the real position of the perturbed body  $\vec{r}$  could be directly calculated using Equation 4.4. Encke's method allows integration on a larger time interval as perturbations,  $\delta r$  and its derivatives are small. However, calculating each step of Encke's method takes much more time comparing to Cowell's method. Also, with accumulating perturbations  $\delta r$  increases and the whole procedure becomes divergent.

## 4.2 Cowell's Method

Cowell's method, often called direct integration, is the simplest and most straightforward method of orbit integration. It comes up from the N-body problem. Simply, for  $N$  gravitationally interacting bodies, the final force affecting the  $i$ -th body is given by the sum of forces from bodies  $j$ :

$$m_i \ddot{\vec{r}}_i = -G \sum_{j=1, i \neq j}^{j=N} \frac{m_i m_j (\vec{r}_i - \vec{r}_j)}{|\vec{r}_i - \vec{r}_j|^3}, \quad (4.5)$$

where  $m_i, \vec{r}_i$  are the mass and state vector of the  $i$ -th body,  $m_j, \vec{r}_j$  are the mass and state vector of  $j$ -th body and  $G$  is the gravitational constant. Equation 4.5 is indeed the formulation of Newton's law of gravitational force for  $N$ -body problem. The principle of this method is to numerically integrate the cartesian coordinates of each celestial body. Considering  $N$ -body problem with its geometry shown on Figure 4.2, dividing Equation 4.5 by  $m_i$  we gain the acceleration of  $i$ -th body to the other  $N - 1$  bodies.

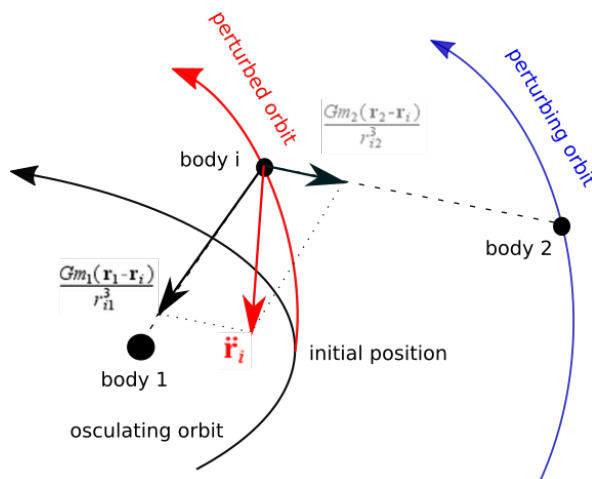


Figure 4.2: Cartoon showing the geometry of Cowell's method.

By numerical integration we can obtain the  $i$ -th body's velocity and by further integration we obtain its position. Since acceleration, velocity and position are three-dimensional vectors, we split them to their components:

$$\vec{a} = \begin{bmatrix} \ddot{x} \\ \ddot{y} \\ \ddot{z} \end{bmatrix}, \vec{v} = \begin{bmatrix} \dot{x} \\ \dot{y} \\ \dot{z} \end{bmatrix}, \vec{r} = \begin{bmatrix} x \\ y \\ z \end{bmatrix}. \quad (4.6)$$

The whole method is based on the integration of each cartesian component separately. To start the numerical integration, we must set the initial conditions of the system. Taking a look at Equation 4.5, the consequent initial conditions are the masses, initial positions and initial velocities of the studied bodies. Taking advantage of the initial conditions, the accelerations could be determined directly from Equation 4.5. The implementation of Cowell's method is easier and quicker than the implementation of Encke's method. However, if the motion of the objects becomes rapid or the perturbations increase, smaller intervals of evaluation are required, which results in the increase of the computational time and errors. Nevertheless, Cowell's method is the chosen method of orbit integration in this thesis. As any suitable numerical integrator could be used to evaluate orbits, in the following section we present two integrators used in this thesis.

## 4.3 Numerical integrators

At the beginning of this section we define the meaning of the term integrator. Let  $\vec{r}$  be the position at time  $t$  and  $h$  a timestep. If we want to determine a new position at time  $t' = t + h$ , which approximates the true position of an object, we require an algorithm. Algorithms that allow us determine such positions are called integrators. Hereby we present the principles of two integrators used in this thesis as they are published in (Press et al., 1986).

### 4.3.1 Euler integrator

Euler's integrator is a simple numerical integrator suitable for solving first order ordinary differential equations. Let have a given differential equation

$$\frac{d\vec{y}}{dt} = f(y, t). \quad (4.7)$$

For a small interval  $h$  in time  $t$ , using Taylor expansion we could obtain

$$y_{i+1} = y_i + f(y_i, t_i)h. \quad (4.8)$$

Since Newton's second law, just as Equation 4.5 is a second order ordinary differential equations, we have to simultaneously solve two first order equations

$$\frac{d\vec{r}}{dt} = \vec{v}(t), \quad \frac{d\vec{v}}{dt} = \vec{a}(t). \quad (4.9)$$

Taking advantage of Equation 4.8 and solving for Equations 4.9, we obtain the following results for orbital motion:

$$\begin{aligned} r_{i+1}^{\vec{r}} &= \vec{r}_i + h\vec{v}_i \\ v_{i+1}^{\vec{v}} &= \vec{v}_i + h\vec{a}_i. \end{aligned} \quad (4.10)$$

While  $\vec{a}_i$  is determined directly from Equation 4.5. As seen in Figure 4.3, the derivative at the starting point of each interval is extrapolated to find the next function value. That means, that Euler's method is asymmetric, which means that it advances the solution through an interval  $h$ , but uses derivative information only at the beginning of the interval. The error in each step of this method is proportional to  $O(h^2)$ . Therefore, to acquire precise solution of a differential equation, small stepsize must be chosen, which markedly increases computational time of the method. Also, the method is not as accurate as other methods run at the equivalent stepsize and most crucially, it is not very stable. Euler's integrator is the most basic Runge-Kutta method. Runge-Kutta methods of higher orders provide more precise solutions of ordinary differential equations.

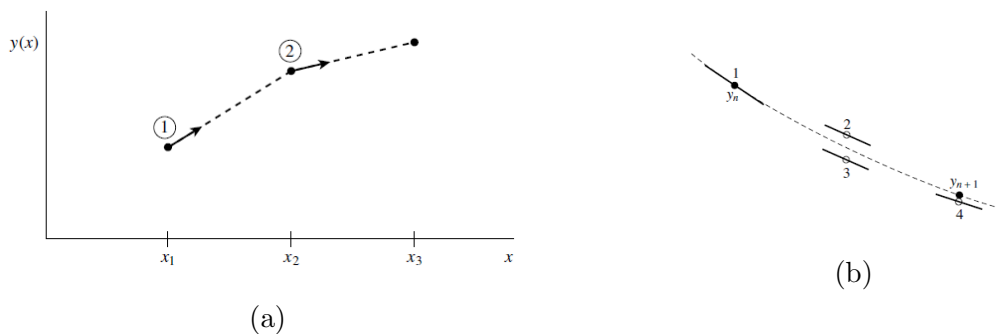


Figure 4.3: Various integration methods. (a) Euler's method. (b) Fourth-order Runge-Kutta method. Credit: (Press et al., 1986)

### 4.3.2 Fourth-order Runge-Kutta integrator

Fourth-order Runge-Kutta method of orbit integration is in fact an extended Euler method. However, fourth-order Runge-Kutta method calculates new function values in more steps, which eventually increases the accuracy of calculation. Coming out from first order differential equations 4.9, we obtain the function values in time  $t' = t + h$  from the following equation:

$$y_{i+1} = y_i + \frac{h}{6}(k_1 + 2k_2 + 2k_3 + k_4), \quad (4.11)$$

where  $h$  is the timestep and the coefficients  $k_1, k_2, k_3$  and  $k_4$  are defined as

$$\begin{aligned} k_1 &= f(t_i, y_i) \\ k_2 &= f(t_i + h/2, y_i + k_1/2) \\ k_3 &= f(t_i + h/2, y_i + k_2/2) \\ k_4 &= f(t_i + h/2, y_i + k_3). \end{aligned} \quad (4.12)$$

Coefficients indicate the slope of the function at the beginning, at the midpoint and at the end of the time interval. The slope of the midpoint is determined twice. The determination of these slopes is shown in Figure 4.3. As there are four coefficients, the fourth-order Runge Kutta method requires four calculations at each step of size  $h$ . The final function value determined from Equation 4.11 is much more precise than the function value determined from the Euler method. The error in each step of this method is proportional to  $O(h^5)$ . Smaller error means, that the method remains stable even if we use larger timesteps during integration.

The method will be used to numerically integrate the orbital motion of multiple system VW LMi to study the nature of the system's secular orbital perturbations.

## Chapter 5

# Radial velocity and Doppler effect

The Doppler shifted stellar velocity in the line of sight of the observer called radial velocity is

$$v_r = \frac{c(\lambda - \lambda_0)}{\lambda_0}, \quad (5.1)$$

where  $c$  is the speed of light,  $\lambda$  is the observed wavelength of light and  $\lambda_0$  is wavelength of light without Doppler shift. Broadening due to rotation of the star is caused by the Doppler shift of light waves caused by the differences of radial velocity of individual surface elements of a star caused by its rotation. Doppler broadening of the spectral lines due to rotation of the star has a shape of rotational profile (Gray, 2005). The observed spectrum is a convolution of the local spectrum (unaffected by macroscopic motions) and the broadening kernel (which includes radial-velocity shifts and rotational broadening). The broadening kernel or broadening function (hereafter BF) gives the dependence of flux on the radial velocity. Thus, instead of a function  $f(u)$ , we observe a function  $h(x)$  which is a convolution with a broadening function (Rucinski, 1999):

$$h(x) = \int_{-\infty}^{\infty} f(u)g(x - u)du = f(x) * g(x). \quad (5.2)$$

The function  $f(u)$  is the sharp-line (or local) spectrum of a non-rotating star being at constant distance with respect to the observer (having zero radial velocity). The function  $h(x)$  The function  $h(x)$  is the observed spectrum of a star with rotationally broadened lines moving in the radial direction. Now we have observed spectrum  $h(x)$ . If we could produce a synthetic spectrum  $f(u)$ , which would be the ideal spectrum of the star without broadening effects, from Equation 5.2 we could determine the broadening function  $g(x)$ . As we are interested in broadening function caused by the motion of the star, we have to choose spectral lines which are less affected by other broadening effects. For this reason we have to choose a spectrum with narrow metal spectral lines, which

are less affected by thermal or pressure broadening. Therefore, the ideal spectral range free of hydrogen lines of the Balmer series and disturbing telluric lines is 4900-5500 Å. Hydrogen atoms move in gas much faster than the atoms of metals, thus its lines are more broadened. Also, lines are more broadened due to high abundance of hydrogen. As regards for the other broadening effects, there are elegantly eliminated during the process of deconvolution. Natural, pressure and thermal broadening of spectral lines are present both on the template and the object spectra. As these effects are the same on both spectra, during the deconvolution they simply eliminate each other. The resulting broadening function has the shape of a rotational profile for a single star rotating as a solid body (as long as we have sufficient spectral resolution). For binaries and multiple stars, the broadening function is a superposition of rotational profiles for individual components shifted in radial velocity because of the Doppler effect. The function  $f(u)$  could be obtained by creating a synthetic spectrum or using a template spectrum of a slow-rotating star, which has similar spectral type, metallicity and  $\log g$  to our studied star. Using this procedure we could obtain the broadening functions, which are caused by the motion of the star and from these broadening functions we could easily determine the radial velocities of the observed star. The radial velocity of a star or a stellar system can be determined by various ways. The most primitive way is to measure centers of stellar lines and finding their Doppler shifts. It is much better to use the information from a longer section of spectrum. This can be done by (i) cross-correlation of the observed spectrum with a spectrum of a radial velocity standard (template) or by (ii) deconvolution of the observed spectrum by a template.

## 5.1 Cross-correlation technique

Hereby we present the method of cross-correlation as published in (Hilditch, 2001). The cross-correlation technique was first implemented by Griffin (1967). Cross-correlation is an operation which for real functions differs from the convolution only in the symmetry of the arguments. The result is the cross-correlation function:

$$ccf(x) = \int_{-\infty}^{\infty} f(u)g(x+u)du = f(x) * g(x). \quad (5.3)$$

The function determines when the two functions  $f(u)$  and  $g(x)$  are best correlated. Here,  $f(u)$  could be comparison star or a synthetic spectrum. The function can be determined using fast Fourier transformation. The maximum of  $ccf(x)$  corresponds to the radial velocity difference of the studied star and the template spectrum. The  $ccf(x)$  resembles to the broadening function but it loses original spectral resolution so it is its pure substitute. Lower resolution means that  $ccf(x)$  is not ideal to determine

the radial velocities of the individual components because of their blending. The cross-correlation was one of the first methods to determine radial velocities from spectra and it is still widely used for single and slowly rotating stars. Therefore, in this thesis we will use the broadening-function technique described in the following section.

## 5.2 Broadening function technique

The broadening function technique is a method of spectra deconvolution worked out by Rucinski (1999). The method could be described through equation:

$$P(\lambda) = S(\lambda) * B(\lambda). \quad (5.4)$$

Here  $P(\lambda)$  is the observed spectrum,  $S(\lambda)$  is the template sharp line spectrum and  $B(\lambda)$  is the broadening function. Essentially, the broadening function is a function mapping sharp-line template spectrum to rotationally broadened spectrum. In principle it is the Doppler image of a star or stellar system, which gives the dependence of flux on radial velocity. The computation of the broadening function is as follows. Having an observed broadened spectrum  $P$  and spectrum of a slowly rotating template  $S$ , we look for the convolution kernel  $B$  to the broadened spectrum  $P$ :

$$P(x) = \int_{-\infty}^{\infty} S(y)B(y - x)dy. \quad (5.5)$$

Both spectra must be expressed in constant step in radial velocity:

$$\lambda_i = \lambda_0(1 + \Delta/c). \quad (5.6)$$

For real and discrete data the Equation 5.5 could be written as summation and results in many linear equations for the broadening function:

$$\begin{pmatrix} s_{m-1} & \dots & s_1 & s_0 \\ s_m & \dots & s_2 & s_1 \\ s_{m+1} & \dots & s_3 & s_2 \\ \cdot & \cdot & \cdot & \cdot \\ \cdot & \cdot & \cdot & \cdot \\ s_{n-1} & \dots & s_{n-m+1} & s_{n-m} \end{pmatrix} \begin{pmatrix} b_0 \\ b_1 \\ \cdot \\ \cdot \\ b_{m-1} \end{pmatrix} = \begin{pmatrix} p_{m_c} \\ p_{m_c+1} \\ \cdot \\ \cdot \\ p_{n-m_c} \end{pmatrix} \quad (5.7)$$

This system of linear equations could in principle be solved e.g., by the Gaussian elimination method. The problem is that we deal with a large set of equations (typically several hundreds) which are ill-defined (close to being singular). A very powerful technique for dealing with sets of equations or matrices that are either singular or

numerically very close to singular is the singular value decomposition (Press et al., 1986). Results obtained via broadening function technique are superior compared to results of the cross-correlation technique as shown in Figure 5.1.

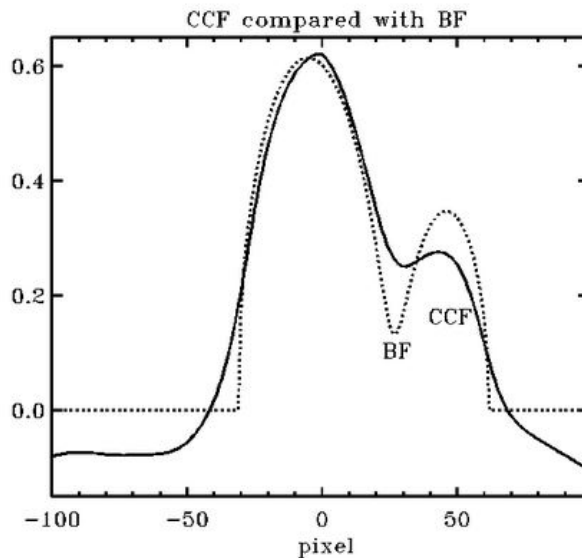


Figure 5.1: Cross-correlation (CCF) compared with the broadening function (BF). Credit: (Rucinski, 1999).

As we see, the broadening function is a true linear deconvolution, with the proper baseline at zero and no distortions. Meanwhile the cross-correlation is a non-linear proxy of the broadening function with various distortions.

The extraction of radial velocities from the broadening functions is done through fitting the broadening functions with Gaussian and rotational profiles. Gaussian profiles fit properly the broadening functions of slowly-rotating stars. This is the case when the projected rotational velocity of the star is comparable or smaller than spectral resolution of our spectrograph in radial velocity. For close binary stars including the extreme case of contact binaries it is better to directly model the broadening functions taking into account so-called proximity effects such as deformed shape of the components, gravitational darkening, mutual irradiation or eclipses. For fast rotators including components of close binaries theoretical limb-darkened rotational profiles are appropriate. Rotational profile can be evaluated without excessive error by the linear limb darkening law:

$$\frac{I_C}{I_C^0} = (1 - \epsilon) + \epsilon \cos \phi, \quad (5.8)$$

where  $I_C^0$  is the specific intensity at the center of the disk and  $\phi$  is the angle between the particular surface element and the direction to the observer (center of the disk) as

viewed from the center of the star (so-called foreshortening angle). It is important to note, that from the various limb darkening laws the linear law is the only one which allows us analytically evaluate the rotational profile. The rotational profile with limb darkening as stated in (Gray, 2005) is as follows:

$$G(\nu) = \frac{2(1 - \epsilon)\sqrt{1 - \left(\frac{\nu_z}{\nu_L}\right)^2} + \frac{1}{2}\pi\epsilon\left(1 - \left(\frac{\nu_z}{\nu_L}\right)^2\right)}{\left(1 - \frac{\epsilon}{3}\right)\pi\nu_L}. \quad (5.9)$$

The shape and the interpretation of the rotational profile is shown on Figure 5.2. Fit of broadening functions via rotational profiles and Gaussian functions is compared on Figure 5.3.

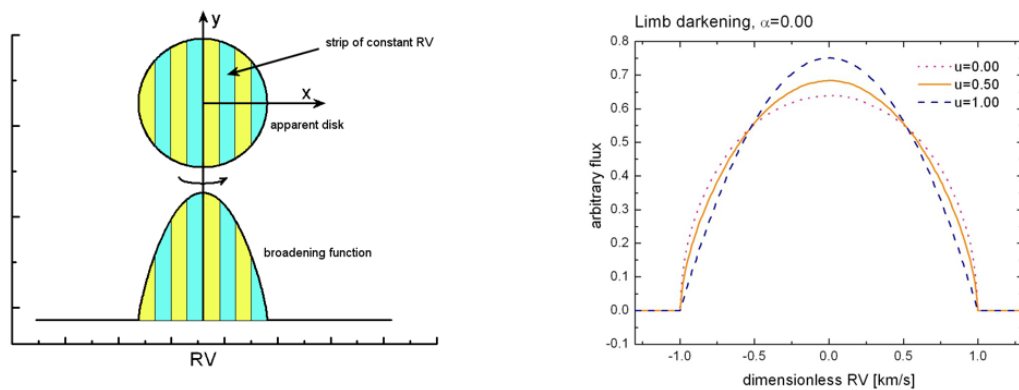


Figure 5.2: The shape and the interpretation of the rotational profile (left), dependence of the rotational profile shape on the linear limb-darkening coefficient (right). Credit: T. Pribulla

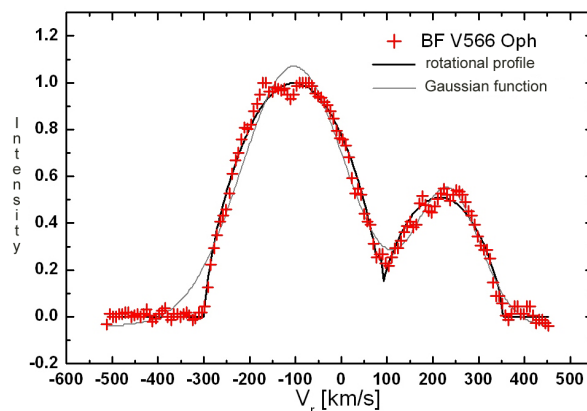


Figure 5.3: Rotational profile and Gaussian function fit of a binary star broadening function. Credit: T. Pribulla.



$$z = -r \sin(\nu + \omega + \pi) \sin i = r \sin(\nu + \omega) \sin i, \quad (5.10)$$

where  $r$  is the position vector,  $\nu$  is true anomaly,  $\omega$  is the argument of periapsis and  $i$  is the inclination angle between the ellipses. As we are interested in determination of speed along z-axis, we differentiate Equation 5.10 with respect to time

$$\dot{z} = \dot{r} \sin(\nu + \omega) \sin i + r \dot{\nu} \cos(\nu + \omega) \sin i. \quad (5.11)$$

We can obtain  $\dot{r}$  from the equation of ellipse in polar coordinates

$$r = \frac{a(1 - e^2)}{1 + e \cos \nu}, \quad \frac{1}{r} = \frac{1 + e \cos \nu}{a(1 - e^2)}. \quad (5.12)$$

Differentiating  $1/r$  gives

$$\begin{aligned} \dot{r} \frac{1}{r^2} &= \dot{\nu} \frac{e \sin \nu}{a(1 - e^2)} \\ \dot{r} &= \dot{\nu} \frac{r^2 e \sin \nu}{a(1 - e^2)} = \frac{2\pi ab e \sin \nu}{Pa(1 - e^2)} = nb \frac{e \sin \nu}{1 - e^2} \\ &= na \sqrt{(1 - e^2)} \frac{e \sin \nu}{1 - e^2} = \frac{nae \sin \nu}{\sqrt{(1 - e^2)}}. \end{aligned} \quad (5.13)$$

Here we used Kepler's second law which is the starting point for the computation of  $\dot{\nu}$

$$\begin{aligned} r^2 \dot{\nu} &= \frac{2\pi ab}{P} = nab \\ r \dot{\nu} &= \frac{nab}{r} = \frac{nab(1 + e \cos \nu)}{a(1 - e^2)} = \frac{nb(1 + e \cos \nu)}{1 - e^2} \\ &= \frac{na\sqrt{1 - e^2}(1 + e \cos \nu)}{1 - e^2} = \frac{na(1 + e \cos \nu)}{\sqrt{1 - e^2}}. \end{aligned} \quad (5.14)$$

Taking advantage of trigonometric formula

$$\begin{aligned} \cos \omega &= \cos[(\nu + \omega) + \nu] \\ &= \cos \nu \cos(\nu + \omega) + \sin \nu \sin(\nu + \omega), \end{aligned} \quad (5.15)$$

we can express the Equation 5.12 as

$$\begin{aligned} \dot{z} &= \frac{nae \sin \nu}{\sqrt{1 - e^2}} \sin(\nu + \omega) \sin i + \frac{na(1 + e \cos \nu)}{\sqrt{1 - e^2}} \cos(\nu + \omega) \sin i \\ &= \frac{na \sin i}{\sqrt{1 - e^2}} [e \cos \omega + \cos(\nu + \omega)]. \end{aligned} \quad (5.16)$$

The observed radial velocity consists of a constant velocity  $V_0$ , which is the velocity of the system's barycenter and from  $\dot{z}$ , which is variable with time since  $\nu$  varies with

time. Other symbols in the equation are Keplerian orbital constants. Thus, the final equation of the radial velocity is as follows

$$RV = V_0 + K[e \cos \omega + \cos(\nu + \omega)], \quad (5.17)$$

where the spectroscopic half amplitude  $K$  is

$$K = \frac{na \sin i}{\sqrt{1 - e^2}}. \quad (5.18)$$

## 5.4 Spectroscopic orbits in quadruple systems

Now, as VW LMi is a quadruple system consisting of two binaries and the spectra of all four components are observable, the radial velocity equation for this quadruple system as expressed in (Pribulla et al., 2008) is:

$$RV_i = V_0 + K_{12}[e_{1234} \cos \omega_{1234} + \cos(\nu_{1234} + \omega_{1234})] \\ + (-1)^{i+1} K_i[e_{12} \cos \omega_{12} + \cos(\nu_{12} + \omega_{12})]. \quad (5.19)$$

This is the radial velocity equation of the contact binary. The contact binary's elements are denoted with indexes "12", while the detached binary's elements are denoted with indexes "34". The elements of the mutual orbit of the quadruple system are denoted with indexes "1234". In Equation 5.19 index  $i = 1, 2$  denotes the individual components. Similarly, the radial velocity equation for the detached binary is as follows

$$RV_i = V_0 - K_{34}[e_{1234} \cos \omega_{1234} + \cos(\nu_{1234} + \omega_{1234})] \\ + (-1)^{i+1} K_i[e_{34} \cos \omega_{34} + \cos(\nu_{34} + \omega_{34})], \quad (5.20)$$

where index  $i = 3, 4$  denotes the individual components. The true anomalies could be computed from

$$\nu = 2 \arctan\left(\sqrt{\frac{1+e}{1-e}} \tan \frac{E}{2}\right), \quad (5.21)$$

where  $E$  is the eccentric anomaly. However, further in this thesis the true anomaly is represented in derivatives by the truncated series up to the second degree in orbital eccentricity as follows:

$$\nu \approx M + 2e \sin M + \frac{5}{4}e^2 \sin 2M, \quad (5.22)$$

where  $M = 2\pi(t - T)/P$  is the mean anomaly, with  $t$  being the observation time,  $P$  the orbital period and  $T$  the time of periastron passage.

As we can see, the radial velocity equation is a function of Keplerian orbital parameters. This is the key to determine orbital parameters through spectroscopy. Radial velocities of the components can be obtained by modeling extracted broadening function by the Gaussian or rotational profiles. If we have a given set of radial velocities with corresponding observation times  $t$ , we could determine the unknown parameters in Equations 5.18, 5.20 and 5.21 via fitting the observed data with the theoretical Equations 5.18, 5.20 and 5.21 using least-squares minimization. This is exactly how the orbital parameters of VW LMi will be determined further in this thesis.

# Chapter 6

## Photometry

VW LMi was detected by the Hipparcos mission as a W UMa-type eclipsing binary. The non-eclipsing binary in the system does not change its brightness and hence it was revealed by the spectroscopy. The light curve of the contact binary was analyzed by Pribulla et al. (2008). The authors determined the inclination angle, degree of contact and mass ratio. In this thesis we will concentrate on the timing information encoded in the photometric data. The light-curve analysis is beyond our scope. To inspect the timing variability, we construct so-called  $(O - C)$  diagram. In the term  $(O - C)$ ,  $O$  stands for observed, while  $C$  stands for calculated value of a physical parameter. It means, that  $(O - C)$  diagram designates the deviation of an observational parameter from its theoretically predicted value. In its broadest sense it is a diagnostic tool in the natural sciences and involves the evaluation and interpretation of the discord between the measure of an observable event and its predicted or foretold value (Sterken, 2005). While observing eclipsing binary systems, the observations are mostly timed in the times of photometric minima. Photometric minima occur when the components of the binary system are eclipsing each other, thus lesser light is observable. From the light curves of such minima we can determine the exact time of the middle of the eclipse. Let this exact time be our observed value  $O$ . As the revolution of a binary system around its center of mass is a periodic event, if we know the length of the revolution's period and at least one time of a photometric minimum, we can determine the upcoming times of photometric minima. This is our value  $C$  in the  $(O - C)$  diagram. If the deviation  $(O - C)$  is marked, it means that the revolution's period changes. The changes in periods are caused by physical processes in the system, such as mass transfer between components, mass loss or decelerating of the rotation due to magnetic braking. Also, the period could change due to light-time effect, which would be described later. Note, that the period changes caused by the light-time effect are apparent and seen by the observer only. The most straightforward method of determining the the upcoming

times of photometric minima is through the linear ephemeris:

$$T_{min} = T_0 + PE, \quad (6.1)$$

where  $T_0$  is an initial minimum time,  $P$  is the period and  $E$  is the epoch. However, if there is a constant change of period in the system, the trend of the  $(O - C)$  diagram is parabolic, therefore the quadratic ephemeris must be used to compute minima times:

$$T_{min} = T_0 + PE + QE^2, \quad (6.2)$$

where  $Q$  is the parameter of the quadratic ephemeris. An example of a star with constantly changing period is shown on Figure 6.1.

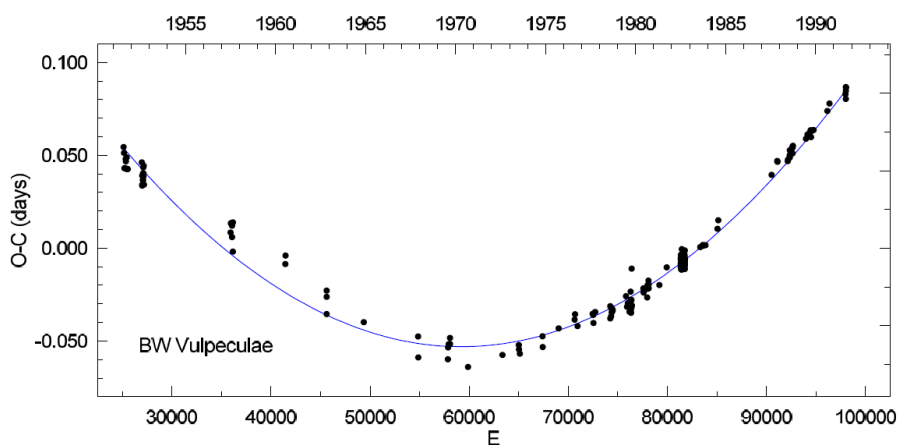


Figure 6.1:  $O - C$  diagram for some  $T_{min}$  of BW Vul with best fit parabola. Credit: (Sterken, 2005)

If the residuals have a sinusoidal trend, it means that periodic changes occur, which could be caused by orbital perturbations, apsidal motion or by the light-time effect.

## 6.1 The light-time effect

The light time effect (hereafter LITE) is an effect caused by the finite speed of light and the changing distance from the observer. As the distance of the observer from the light source varies also varies the time needed to travel this distance at the speed of light (light-time). This basic, yet brilliant principle was recognized by Ole Rømer, who firstly estimated the speed of light from the observations of Jupiter's moons using this exact principle. LITE in eclipsing binaries, caused by the orbital motion of the eclipsing pair around the barycenter of the triple system, produces period variation in minima timings (Zasche, 2005). Analyzing the  $(O - C)$  diagram of the eclipsing binary it is possible to determine the orbital parameters of the eclipsing binary's orbit

around the triple system’s barycenter. This is crucial in case of VW LMi as we can combine spectroscopic and photometric observations in order to determine the orbital parameters of the quadruple system. If there is LITE present, the ephemeris could be computed from equation:

$$T_{min} = T_0 + PE + QE^2 + \Delta T, \quad (6.3)$$

where  $c$  is the speed of light. The amplitude of LITE is:

$$\Delta T = \frac{a_{in} \sin i}{c} \left( \frac{1 - e^2}{1 + e \cos \nu} \sin(\nu + \omega) + e \sin \omega \right), \quad (6.4)$$

where  $a_{in}$  is the semi-major axis of the eclipsing binary and  $e$ ,  $\nu$ ,  $\omega$  are the eccentricity, true anomaly and the argument of perigee of the mutual wide orbit. Note, that the Equation 6.4 could be derived directly from Equations 5.10 and 5.11. The light-time is derived simply from Equation:

$$t = \frac{z}{c}, \quad (6.5)$$

where  $z$  is the distance of the object  $c$  is the speed of light. The sinusoidal trend in the  $O - C$  diagram caused by the LITE is shown in Figure 6.3.

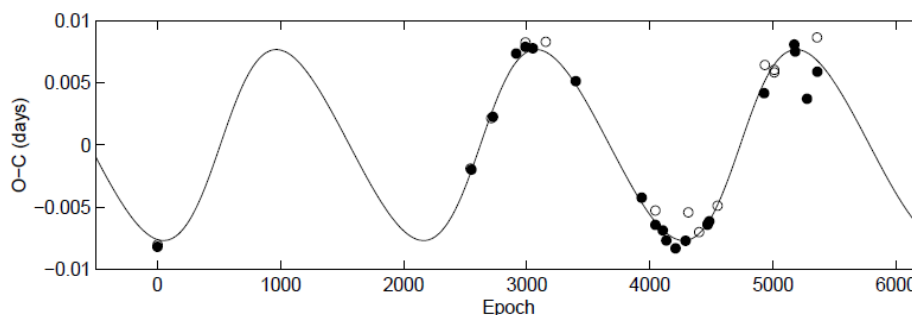


Figure 6.2: An example of an  $O - C$  diagram of AU Aur with LITE . Credit: (Zasche, 2005)

As stated in (Wolf, 2014), LITE in eclipsing binaries and its combination with other effects of celestial mechanics is a very efficient tool for study of triple and multiple stellar systems. It can only be applied successfully in those cases where the expected period of the third body is well defined by existing observations.

## 6.2 Minima determination

Most widespread approach to obtain instants of minima of eclipsing binaries is to use Kwee & van Woerden’s method (Kwee and Van Woerden, 1956). From our experience

the errors estimated using their formula (14) are often unrealistically small. The real uncertainties are very probably dominated by systematic errors. The principal problem in case of CCD photometry is scattered light which cannot be fully corrected by flat-fielding. This results in spurious shifts/trends in differential photometry in case that the telescope is not perfectly guided making times of minima systematically shifted. Our photometry could possibly be improved by using an algorithm based on Principal Component Analysis proposed by Tamuz et al. (2005). Unfortunately, the frames were obtained at several observatories with different setups and even different orientation of the field. Systematic errors in minima positions were partially removed by fitting technique proposed below. Since light curve of the system appears to be very stable (we do not see any asymmetries or changes) fitting templates were prepared to obtain instant of conjunction (minimum) for any sufficiently long photometric sequence. Such a way we made use not only of the minima but of other light curve segments. The template light curves were represented by symmetric trigonometric series of the 10th order.

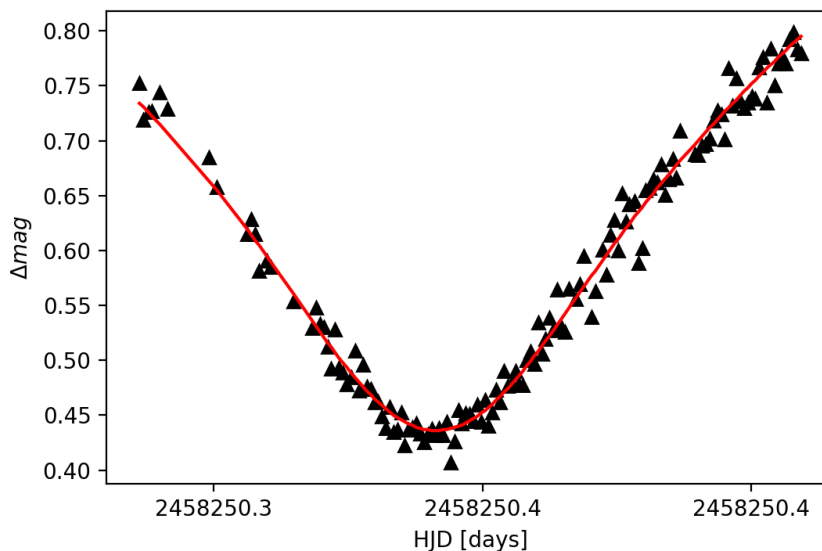


Figure 6.3: An example of a fit of the observed light curve by template  $T(x)$ . From the best fit a new minimum time was determined.

Even if the eclipsing pair is a contact binary, amplitude of it's light curve depends on the wavelength. The differences in amplitude primarily result from wavelength-dependent limb darkening and light contribution of the non-eclipsing binary. Due to the differences in filter transparencies and wavelength response of detectors we had to form a template light curve for each filter separately and the fitting light curve was scaled to match the observations. We also noted small ( $\approx 0.02$  mag) shifts of the light

curves observed even with the same instrument. Sometimes even slight slopes of the light curve were recorded. These shifts/slopes are very probably caused by scattered light combined with different pointing of the telescope. To obtain good fits of the observed light curves by templates  $T(x)$  we formed the following fitting function:

$$F(x) = A + Bx + CT(x - D). \quad (6.6)$$

This allowed for shifting, scaling and "slanting" of the template light curve. Fixing of the parameters was judged according to the appearance of individual light curves. The example of a fit of the observed light curve by template  $T(x)$  is shown in Figure 6.3.

### 6.3 LITE and VW LMi

While determining the orbital parameters of VW LMi, we decided to fit a global model to radial velocities and the minima times to better characterize the outer orbit. Rigorous modeling of those datasets (four RV curves and times of minima) is quite complex since times of all RV observations should be properly corrected for the LITE caused by the mutual revolution of the binaries (Pribulla et al., 2008). The LITE is most important in the case of the minima times of the contact binary orbit, where the LITE amplitude is substantially larger than the data errors. Thus we will ignore LITE correction of the radial velocity data. For this specific quadruple system, the Equation 6.3 for the ephemeris of the contact binary acquires the following form:

$$T_{min} = T_{12} + P_{12}E + QE^2 + \Delta T_{12}, \quad (6.7)$$

where the last term is the amplitude of LITE:

$$\Delta T_{12} = \frac{K_{12}P_{1234}(1 - e_{1234})^{3/2} \sin(\nu_{1234} + \omega_{1234})}{2\pi c (1 + e_{1234} \cos \nu_{1234})}, \quad (6.8)$$

while our reference plane is the plane parallel to the sky and intersecting mass center of the quadruple system. As we see, 6.7 and 6.8 shares the orbital parameters with the radial velocity equation for the quadruple system VW LMi, presented in Section 5.4. In the further data processing, these equations will be used for the global fit of the observations to determine the orbital parameters of VW LMi.

## 6.4 Combining spectroscopy and photometry

We decided to fit the datasets of the radial velocities together with the dataset of new photometric minima times. Both datasets are, however, nicely complementary: during the spectroscopic conjunction, when the radial velocities of the components are not measurable, we can observe minima giving the radial distance of the eclipsing binary in the outer orbit.

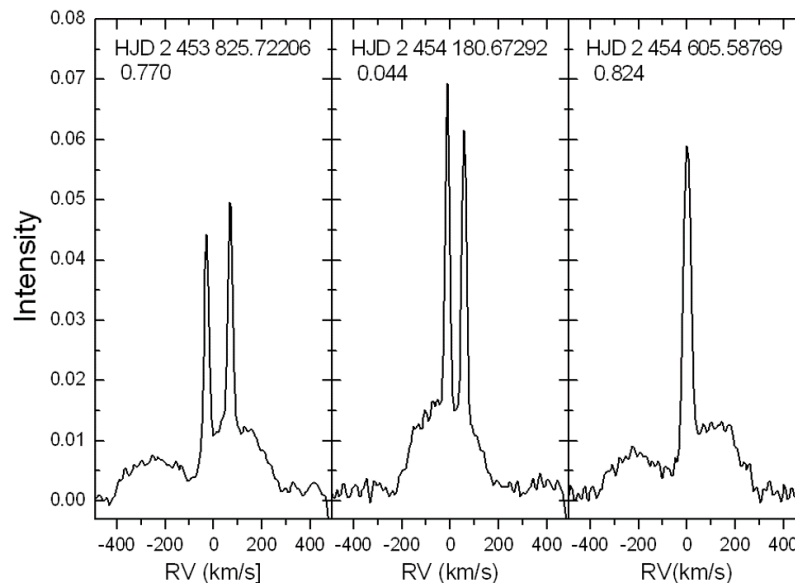


Figure 6.4: Broadening functions of VW LMi. Left to right: all four components visible, contact binary’s components in conjunction, detached binary’s components in conjunction. Credit: (Pribulla et al., 2008)

As we can see in Figure 6.4, when the binary systems are in conjunctions, their broadening functions are blended, thus one cannot determine the radial velocities of components. However, the time of the contact binary’s conjunction is exactly the time of a photometric minimum. Photometric minima times can be modelled by Equation 6.7. Combining spectroscopic and photometric observations allows us to determine the orbital parameters more precisely as in times of spectroscopic conjunctions we still have observational information about the orbits in form of photometric minima times.

# Chapter 7

## New observations of VW LMi

As our aim is to find secular changes of orbits in the hierarchical quadruple VW Leonis Minoris, the basis of this thesis was to obtain new observations to acquire the current Keplerian orbital parameters of this system. The purpose of acquiring new orbital parameters is to compare them with the decade-old orbital parameters shown in Table 3.2 determined by Pribulla et al. (2008). This comparison should expose definite changes in system's orbits. New observations were obtained in season 2017-2018. Leo Minor is in observable altitudes in a period from November up to May. In this period during years 2017 and 2018 several new spectroscopic and photometric observations of VW LMi were obtained at Astronomical Institute of the Slovak Academy of Sciences in Tatranská Lomnica and at Thüringer Landessternwarte Tautenburg.

### 7.1 Spectroscopic observations

Medium and high-dispersion spectroscopy of VW LMi was obtained with three spectrographs. At Stará Lesná observatory the observations were performed at the G1 pavilion with a 60cm, f/12.5 Zeiss Cassegrain telescope equipped with a fiber-fed échelle spectrograph eShel (Pribulla et al., 2015; Thizy and Cochard, 2011). The spectrograph has a 4150-7600 Å (24 échelle orders) spectral range and a maximum resolving power of about  $R = 11,000$ . The ThAr calibration unit provides about 100 m.s<sup>-1</sup> radial-velocity accuracy. An Atik 460EX CCD camera, which has 2749×2199 array chip, 4.54 μm square pixels, read-out noise of 5.1 e<sup>-</sup> and gain 0.26e<sup>-</sup>/ADU, was used as the detector. The observations were also performed with a 1.3m, f/8.36, Nasmyth-Cassegrain telescope equipped with a fiber-fed échelle spectrograph at Skalnaté Pleso. Its layout follows the MUSICOS design (Baudrand and Bohm, 1992). The spectra were recorded by an Andor iKon 936 DHZ CCD camera, with a 2048×2048 array, 13.5μm square pixels, 2.7e<sup>-</sup> read-out noise and gain close to unity. The spectral range of the

instrument is 4250-7375 Å (56 échelle orders) with the maximum resolution of  $R = 38,000$ . Additional spectra were obtained at Thüringer Landessternwarte Tautenburg with the Alfred Jensch 2m telescope and coude échelle spectrograph. These spectra cover 4510-7610 Å in 51 orders. A 2.2'' slit was used for all observations giving  $R = 31,500$ .

Because of the short orbital period the exposure times were limited to 900 seconds to prevent orbital-motion smearing.

The raw data obtained with the 60cm and 1.3m telescopes were reduced using IRAF package tasks, Linux shell scripts and FORTRAN programs as described in Pribulla et al. (2015). In the first step, master dark frames were produced. In the second step, the photometric calibration of the frames was done using dark and flat-field frames. Bad pixels were cleaned using a bad-pixel mask, cosmic hits were removed using the program of Pych (2004). Order positions were defined by fitting Chebyshev polynomials to tungsten-lamp and blue LED spectra. In the following step, scattered light was modeled and subtracted. Aperture spectra were then extracted for both object and ThAr lamp and then the resulting 2D spectra were dispersion solved. The spectra obtained at Thüringer Landessternwarte Tautenburg were reduced under the IRAF environment (Guenther et al., 2009; Hartmann et al., 2010; Hatzes et al., 2005).

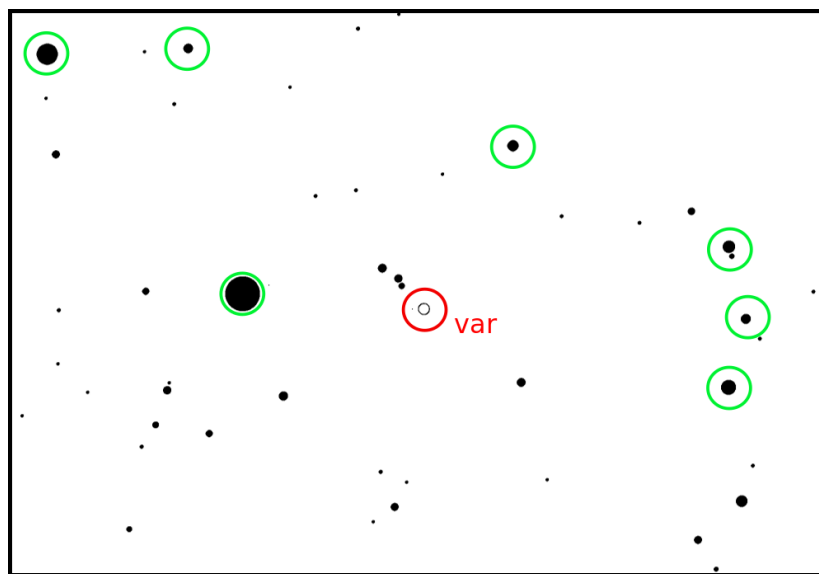


Figure 7.1: Comparison stars used in aperture photometry and VW LMi.

## 7.2 Photometric observations

Multicolour photometric observations were obtained primarily to measure the light-time effect but could be used to constrain possible secular inclination-angle changes.

CCD *BVI* photometric data of VW LMi were also obtained. The primary goal of the photometry was to better define the timing variability in the outer orbit. The data were obtained at the Stará Lesná observatory with a 18cm f/10 auxiliary Maksutov-Cassegrain telescope attached to the Zeiss 60cm Cassegrain used to obtain the échelle spectroscopy (G1 pavillion). An SBIG ST10 MXE CCD camera and the Johnson-Cousins filters were used. The field of view (FoV) of the CCD camera is  $28.5 \times 18.9'$ . The filter set is also close to the Johnson-Cousins system. The CCD frames were photometrically reduced under the IRAF environment. First, master dark and flat-field frames were produced, then bad pixels were cleaned and the frames were photometrically calibrated. Prior to aperture photometry all frames were astrometrically solved to define the pixel to WCS<sup>1</sup> transformation. Ensemble aperture photometry was performed with respect to 8 stars close to VW LMi as shown in Figure 7.1.

---

<sup>1</sup>World Coordinate System

# Chapter 8

## Data processing

The data processing consisted of deconvolution of the spectra in IDL to extract the broadening functions and to determine the radial velocities of the quadruple system's individual components, global fit to radial velocities and minima times to determine the orbital parameters and the numerical integration of orbits for further study of the system's secular orbital evolution. While spectra deconvolution and radial velocity extraction was done in IDL using routines of Rucinski (1999), for the global fit of radial velocities and the photometric minima times and the numerical integration of orbits own software tools were developed. The workflow of the data processing is shown in Figure 8.2.

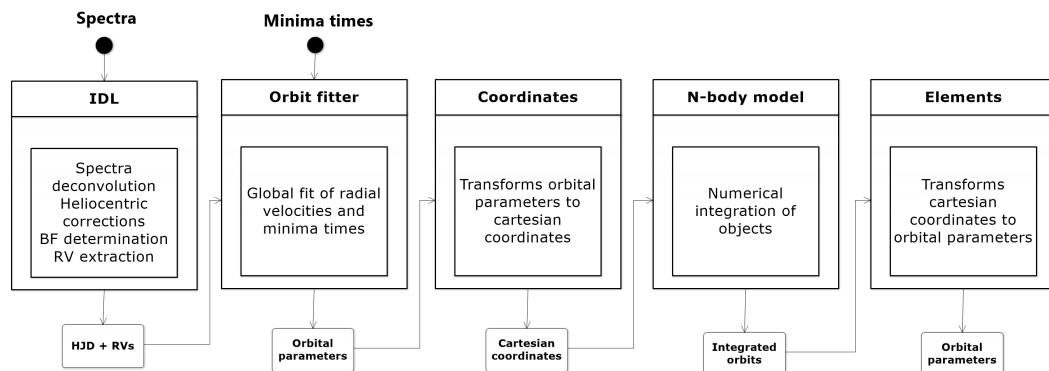


Figure 8.1: UML diagram of data processing.

The reduction of spectroscopic (raw frames to 1D normalized spectra) and photometric data (raw frames to light curves) was performed by the supervisor. The focus of this thesis is on the processing of spectroscopic and photometric observations, especially the determination of the observed system's orbital parameters through global fit of the data and numerical modeling of the system. Hereby, we describe the steps of our data processing workflow as well as the process of our development of new software tools.

## 8.1 IDL

Interactive Data Language (IDL) is a high-level programming language designed specifically for scientific data analysis (Bowman, 2006). IDL consists of both an interactive programming environment and a programming language. The first part of our workflow - spectra processing was done in IDL. Our aim was to deconvolve spectra, and afterwards to determine the radial velocities of VW LMi's components modeling the extracted broadening functions. As working with stellar spectra in form of FITS files, and important prerequisite was the Astro library for IDL (Landsman, 1993). This library contains routines for reading and writing FITS files, performing barycentric correction of spectra and a lot more. All the spectra processing was done using IDL routines<sup>1</sup> of Rucinski (1999), which use the broadening function technique. Hereby, we present the important steps of the spectra processing.

### 8.1.1 Analysis of the template spectrum

First of all, all spectra must be fully reduced - wavelength calibrated and normalized to unity at maxima (rectified). The work process starts with the singular value decomposition of the template spectrum using routine *BFpro1.pro*. This step is necessary for the derivation of broadening functions from all other spectra. The template was a spectrum of star HD128167. This star has similar spectral type, metallicity and  $\log g$  as VW LMi. However, HD128167 is slow-rotating, therefore it's spectral lines have minimal Doppler broadening. The template spectrum was taken with the same instrument as the spectra of VW LMi, thus the instrumental effects were effectively removed from all object spectra. The routine allows selection of the preferred spectral range. This is a crucial step as we must avoid telluric lines and select a spectral range without wide hydrogen lines, which are most affected by thermal Doppler broadening. In our case this spectral range is 4900-5500 Å. Using routine *BFpro1.pro* the spectra with originally linear wavelength vectors are rebinned to spectra with logarithmic wavelength vectors. Prior using this routine we have to choose a reasonable step in the velocity vector, which covers the resolution of the spectrum, ideally 2-3 steps per FWHM resolution.

### 8.1.2 Extraction of the broadening functions

The next step was the extraction of the broadening functions from the spectra of VW LMi. Solving linear Equations 5.7 we obtain the broadening functions for our object

---

<sup>1</sup>The routines are available here: <http://www.astro.utoronto.ca/~rucinski/BFdescription.html>

spectra. The method of deconvolution has an important consequence. As stated in Chapter 5, we have to choose a spectral range with spectral lines which are not affected by other than Doppler broadening effects. Evidently, all spectral lines are affected by natural and pressure broadening. However, the effects of these broadenings on the template spectrum and on our object spectra are the same as we had chosen HD128167 as the source of our template spectrum. This star has almost the same local spectrum (similar  $T_{eff}$ ,  $\log g$  and metallicity) as VW LMi, thus the stated broadening effects on the template spectrum and the object spectra are the same. The deconvolution causes that effects, which are the same on both template and object spectra will be eventually eliminated. Thus the resulting broadening function is an exclusive function of Doppler broadening caused by the motion of the observed object. The extraction of the broadening functions was done using the routine *BFpro2.pro*.

### 8.1.3 Smoothing of the broadening functions

Take a look at Figure 8.2, top left picture. This is the broadening function of VW LMi determined with routine *BFpro2.pro*. As we see, the shapes of the function are not well defined. This is caused because the individual points in the function are treated as independent variables. Moreover, our spectrograph has a finite spectral resolution. Thus we have to convolve the broadening function (which has now virtually infinite resolution) with Gaussian corresponding to the spectral resolution of our instrument. Smoothing of the functions is done through convolution with Gaussian functions with various widths of FWHMs. FWHM is a function of the function's variance  $\sigma$ . In Figure 8.2 we present the smoothed broadening functions of VW LMi for various values of variance  $\sigma$ . As we increase the value of  $\sigma$ , the shape of the function becomes more marked and the individual broadening functions of the quadruple's components become visible. The two sharp peaks are the broadening functions of the slow-rotating detached binary system, while the two wider peaks are the broadening functions of the contact binary system.

### 8.1.4 Heliocentric velocity corrections

To ensure correct measurements of radial velocities from the obtained broadening functions we must compute heliocentric dates of middle exposure, heliocentric radial velocity corrections and orbital phases of periodic variables. These computations and routines are provided by routines *hjd.vel* and *hjd.phase*, respectively.

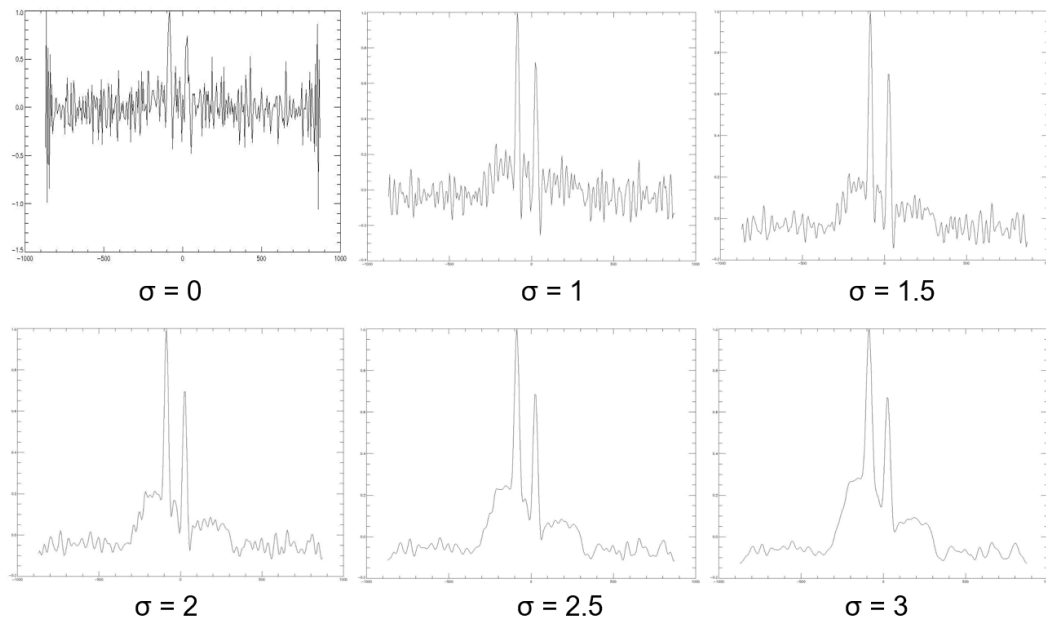


Figure 8.2: Smoothed broadening functions of VW LMi. Smoothing was done through convolution with Gaussian functions with various values of  $\sigma$ .

### 8.1.5 Radial velocity extraction

The final step is the determination of the radial velocities of the individual components. Because of the reason stated in Subsection 8.1.2, the profiles of components can be approximated by Gaussian profiles. However, in case of a contact binary system, the profile of the broadening function must be modelled by rotational profile with limb darkening. Therefore, the extraction of the radial velocities of the quadruple VW LMi was done as follows. Firstly, all four peaks of the broadening function were modelled by Gaussian functions. From the best fits of the Gaussian functions the radial velocities of the detached binary were determined directly. Afterwards, we had to subtract the peaks of the detached binary in order to model the remaining peaks of the contact binary system by rotational profiles with linear limb darkening. From the best fit of the broadening function by Equation 5.9 we determined the radial velocities of the contact binary system's individual components. As an example we present the broadening functions of VW LMi in Figure 8.3. As we see on the left image all four components of the quadruple systems are visible.

## 8.2 Orbit fitter

The outputs from the data processing in IDL were arrays of radial velocities and corresponding heliocentric julian dates for VW LMi's individual components. In order to determine the orbital parameters of VW LMi we had to model the observational

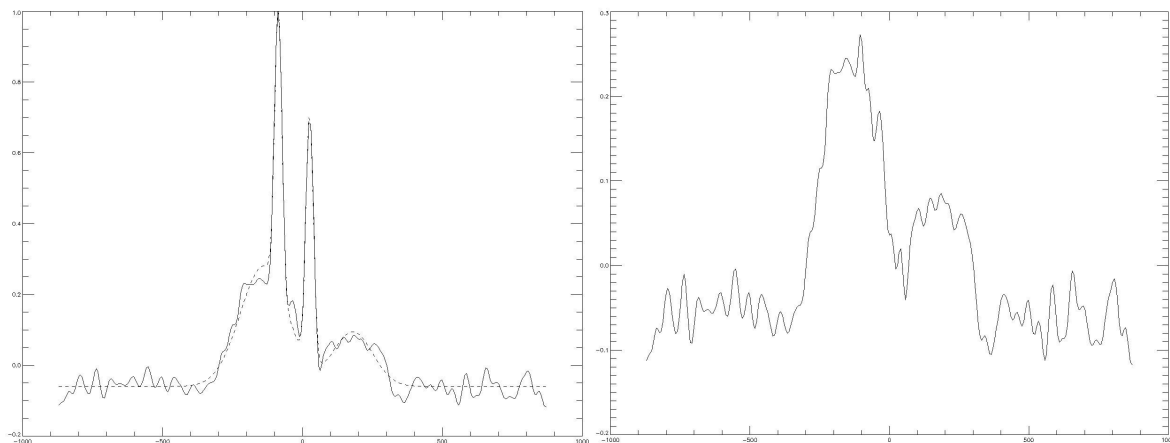


Figure 8.3: Broadening functions of VW LMi. On x-axis is the radial velocity and on the y-axis the intensity. Left: all four components visible with their best Gaussian fits. Right: components of the contact binary after subtraction of the detached system’s components.

radial velocities with the theoretical equation of the radial velocity, see Equations 5.19 and 5.20 together with the obtained times of photometric minima. To perform the mentioned global fit of all five datasets (radial velocities of four components and the photometric minima times), we developed a new software tool - *Orbit fitter*. The tool was written entirely in Python programming language with the use of Python libraries *pandas* (data manipulation library), *numpy* (numerical procedures library), *lmfit* (non-linear optimization and curve fitting library) and *matplotlib* (visualization and plotting library). The optimization of data was performed via simplex method for function minimization (Press et al., 1986). This optimization method, originally published by Nelder and Mead (1965) was provided in Python’s *lmfit* library. The source code of the *Orbit fitter* is presented in Appendix B. Hereby, we present the most important steps of data processing via this software tool. Line numbers are references to Appendix B.

### 8.2.1 Preparing the fit

The first part of our tools is responsible for reading the datasets of radial velocities and minima times and converting these datasets to numerical arrays, which are suitable for further methods. All the data manipulation was done using library *pandas*. Starting from line 32, we define the functions, which were used during the optimization. These are the equations of the mean anomaly, true anomaly 5.21, the LITE ephemeris 6.7 and the radial velocity equation for the contact binary 5.19 and for the detached binary 5.20.

### 8.2.2 The parameters

The parameters are objects of *lmfit*'s class *Parameters*. These objects are the key concepts of *lmfit* library. Parameters are the quantities to be optimized in all minimization problems, in our case the parameters are the Keplerian orbital elements defined on lines 94-112. By using *Parameter* objects instead of plain variables, the objective function does not have to be modified to reflect every change of what is varied in the fit, or whether bounds can be applied. This simplifies the writing of models, allowing general models that describe the phenomenon and gives the user more flexibility in using and testing variations of that model (Newville et al., 2016).

### 8.2.3 Individual fits of the datasets

Individual fits of the datasets were necessary before the global fit. The goodness of fit is described through the reduced chi-squared distribution  $\chi_\nu^2$  (Bevington et al., 1993):

$$\chi_\nu^2 = \frac{1}{\nu} \sum_{i=1}^N \frac{(O_i - C_i)^2}{\sigma_i^2}, \quad (8.1)$$

where  $O_i$  are the observed data,  $C_i$  the calculated data,  $N$  the number of data-points,  $\sigma_i$  are the uncertainties of the observed data and  $\nu$  is the number of the degrees of freedom, which equals to number of observations  $N$  minus number of fitted parameters  $m$ . The value of  $\chi_\nu^2$  is in substance the summed deviation of our observed data from the theoretically calculated expectations. In an ideal case, if the uncertainties of the data are correctly determined and our model is appropriate,  $\chi_\nu^2$  is close to unity. Our individual fits (starting from line 114) were necessary, because our observational data had not assigned uncertainties. Thus, we had to determine the unknown values of  $\sigma$  before approaching to global fit of the data. The unknown uncertainties were determined by fitting the individual datasets and changing the values of  $\sigma$ , until  $\chi_\nu^2$  for each dataset was closest to unity. The determined values of  $\sigma$  were then used as average uncertainties of datasets in the global fit of the data.

### 8.2.4 Global fit of the data

This is the ultimate method of the *Orbit fitter*. In order to determine the unknown orbital parameters, we fitted all our datasets at once. As a merit function we used the reduced chi-squared distribution, see Equation 8.1. The merit function defined on line 157 was optimized using *lmfit*'s *minimize* method, which we called on line 199. The result of the global fit was the set of optimized orbital parameters.

### 8.2.5 Plot of radial velocity curves

The rest of our code is responsible for calculating the phases of observations and plotting the curves of radial velocities and LITE ephemeris against the observational data. While plotting the observational data, we had subtracted the motion of the mutual mass center of the quadruple system.

### 8.2.6 Comparing different approaches

The developed tool *Orbit fitter* relies on numerical procedures carried out by various Python libraries. The merit function 8.1 is minimized by numerical methods in many iterations. This thesis compares the orbital parameters of VW LMi published by Pribulla et al. (2008). However, in (Pribulla et al., 2008) a different approach was used. The merit function was minimized by the steepest descent approach (gradient method). Let the merit function's quantity  $(O_i - C_i)$  be a function  $f$  we want to minimize. We have to compute the partial derivatives of function  $f$  by each parameter<sup>2</sup>:

$$\delta f = \frac{\partial f}{\partial V_0} \delta V_0 + \frac{\partial f}{\partial K_{12}} \delta K_{12} + \frac{\partial f}{\partial K_{34}} \delta K_{34} + \dots \quad (8.2)$$

We then put  $\delta f$  back in the merit function 8.1 and optimize the function via simplex method for function minimization (Nelder and Mead, 1965). In (Pribulla et al., 2008) computation of Equation 8.2 was done using analytic formulas for derivatives in the merit function and optimized using a software tool written in Fortran language. Using this approach, the number of optimization iterations is much smaller as there is no need to partially derive the merit function (eighteen times). In the following Chapter, we present our results obtained through both approaches.

## 8.3 *Coordinates* module

Presented in Appendix C, module *Coordinates* is a trivial, yet important transformation module in between *Orbit fitter* and *N-body model*. Via *Orbit fitter* we had determined the Keplerian orbital elements of VW LMi. However, as we decided to use Cowell's method of orbit integration, we needed some initial cartesian position and velocity vectors of VW LMi's components before orbit integration. Module *Coordinates* provides the transformation from Keplerian orbital elements to cartesian position and velocity vectors at some arbitrary initial time using basic equations of orbital mechanics (Danby, 1992). The origin of our cartesian coordinate system is in the mutual mass center of both binaries, while our reference plane is the plane perpendicular to observer

<sup>2</sup>Note, that in our case we have eighteen orbital parameters we want to optimize.

- the plane of sky. Thus, we also had to perform transformation of the cartesian vectors to the plane of sky. This transformation of positions was performed using the following equations (Hilditch, 2001):

$$\begin{aligned}x &= r(\cos \Omega \cos(\omega + \nu) - \sin \Omega \sin(\omega + \nu) \cos i) \\y &= r(\sin \Omega \cos(\omega + \nu) + \cos \Omega \sin(\omega + \nu) \cos i) \\z &= r(\sin i \sin(\omega + \nu)).\end{aligned}\tag{8.3}$$

While the velocities were transformed through:

$$\begin{aligned}v_x &= \frac{xhe}{rp} \sin \nu - \frac{h}{r} \cos \Omega \sin(\omega + \nu) + \sin \Omega \cos(\omega + \nu) \cos i \\v_y &= \frac{yhe}{rp} \sin \nu - \frac{h}{r} \sin \Omega \sin(\omega + \nu) - \cos \Omega \cos(\omega + \nu) \cos i \\v_z &= \frac{zhe}{rp} \sin \nu - \frac{h}{r} \cos(\omega + \nu) \sin i,\end{aligned}\tag{8.4}$$

where  $h$  is the absolute value of the angular momentum vector. These obtained components of the cartesian position and velocity vectors served as initial conditions for our numerical simulation.

## 8.4 N-body model

As we wanted to study the scale and long-term evolution of the orbital changes in the quadruple system VW LMi, we had developed a numerical simulator *N-body model*, to perform numerical integration of orbits in this system. The tool was written entirely in Python programming language with the use of Python libraries *numpy* (numerical procedures library) and *matplotlib* (visualization and plotting library). *N-body model* is an object-oriented software tool, where stellar objects are represented as objects (arbitrary objects could be defined). The source code of the *N-body model* is presented in Appendix D. Hereby, we describe it's individual parts.

### 8.4.1 Class *Body*

Class *Body* (defined on line 63) is used to define celestial objects. The objects are defined through their masses and initial components of their position and velocity vectors. In case of VW LMi, the initial vector components were computed using module *Coordinates*. The masses of VW LMi's individual stellar components were obtained from (Pribulla et al., 2008). An important part of this class is the method *CalcAcc* (defined on line 75). Using Equation 4.5 this method provides the calculation of the acceleration vector of the celestial body. Additional methods *Energy* and *Momentum* provide the

calculation of the body’s total energy and angular momentum, which are necessary to inspect as these quantities during integration are conserved. List *Body.attributes* is used to store the results of numerical integration.

### 8.4.2 Class *Model*

Class *Model* (defined on line 103) is the core of the *N-body model*. List *Model.attributes* stores the celestial objects, the stellar system we want to simulate. Method *RK4* (line 109) is the fourth-order Runge-Kutta integrator, which calculates new positions, velocities and accelerations for each stellar object and appends these new values to their *Body.attributes* lists. The main method of this class is *simulation* (defined on line 175). It provides the iteration to calculate new position, velocity and acceleration vectors for defined time interval and step size. The final method *plot* provides visualization of the integrated orbits.

### 8.4.3 Integrating VW LMi

Quadruple stellar system VW LMi is defined from line 213. During the integration we focused on the orbital changes of the detached binary as modelling the contact binary system would require a different gravitational model, with built in solid-body model of the stars, which is not implemented in the current version of our *N-body model*. Thus, we took the contact binary system as one point mass and we studied the changes in orbits of the detached binary. As  $P_{34} = 7.929$  days, the timestep of integration must be much chosen to be much smaller than period  $P_{34}$ . Further, as Kozai timescales of secular orbital changes of the detached binary system are on scales of decades, we had to integrate the orbits for several decades to observe secular changes in their orbital elements. From spectroscopy one cannot determine the values of the longitudes of the ascending nodes. As the scale of secular orbital changes in the orbit of the detached binary directly depends on the difference of the longitudes of ascending nodes  $\Omega_{34}$  and  $\Omega_{1234}$ , we set  $\Omega_{34} = 0$  and integrated the orbits for various values of  $\Omega_{1234}$ . The result of the integrations were the positions and velocities of components.

### 8.4.4 Additional simulations with ReboundX

As we will discuss later, the fourth-order Runge-Kutta integrator proved to be insufficient for integrating such a tight stellar system as VW LMi. We were able to integrate the system for some orbital periods, but afterwards the simulation lost its stability. Therefore, we used C/Python simulator ReboundX (Tamayo et al., 2016) to perform long-term numerical integrations of system VW LMi. ReboundX uses a fifteenth-order

adaptive stepsize Runge-Kutta integrator *ias15* (Rein and Spiegel, 2014). This integrator proved to be sufficient to integrate our system for several centuries.

## 8.5 *Elements* module

The final part of the data processing was done using the *Elements* module. The results of our numerical integrations were the cartesian position and velocity vectors of VW LMi's components. In order to study the system's orbital changes we developed the module *Elements*, which transforms cartesian vectors to Keplerian orbital elements. The source code of the module is presented in Appendix E. The main transformation method is defined on line 14. All the transformations were performed in relative orbital frame - we inserted the heavier component of the binary to the center of the system and considered that the less heavier component orbits the heavier component. In this method we firstly calculated the angular momentum vector ( $\mathbf{h\_bar}$ ). We also calculated the eccentricity vector (*ecc\_vec*), which points from the mass center of the binary system to the periastron of the orbit and the vector  $\mathbf{n}$  pointing towards the ascending node and the true anomaly. Afterwards, using basic equations of celestial mechanics we calculated the orbital parameters we were interested in: semi-major axis  $a$ , orbital eccentricity  $e$ , longitude of the ascending node  $\Omega$  and the argument of periastron  $\omega$ . In order to determine the inclination between VW LMi's binary systems, the method also returns the components of the angular momentum vector.

# Chapter 9

## Results

Following the workflow presented in Chapter 8 we processed the new spectroscopic and photometric observations of the quadruple system VW LMi. This Chapter is dedicated to presentation of our results. In dedicated sections we present the results of spectra deconvolution and radial velocity extraction in IDL, global fit of the radial velocities and minima times in order to determine the orbital parameters and the numerical integration of orbits of VW LMi.

### 9.1 Radial velocities

As stated in Chapter 7, we obtained new spectra of VW LMi at Stará Lesná, Skalnaté Pleso and Tautenburg observatories. The quality of these spectra differed widely between the observatories. The precision of the radial-velocity measurements is determined by the resolution of the spectrograph, the signal-to-noise ratio, the observed spectral range, the density of spectral lines, and the projected rotational velocity of the observed object ( $v \sin i$ ). The signal-to-noise ratio (SNR) depends on the sky transparency, object altitude and seeing conditions. Taking all this to account, the best quality spectra were from Thüringer Landessternwarte Tautenburg. The runner-ups were the spectra from Skalnaté Pleso MUSICOS spectrograph and the least quality spectra were from Stará Lesná eShel spectrograph. Controversially, we neglected the use of Tautenburg spectra. Only a few spectra from this observatory were available (9). In addition, after the determination of their broadening functions we saw, that on some of these spectra either or both binaries were in conjunction resulting in blended component profiles, therefore we were not able to extract their radial velocities. Although the spectra from Tautenburg were the most precise, their statistical weight was too negligible to reliably determine the orbital parameters of VW LMi. Consequently, all new radial velocities were determined from spectra taken by échelle spectrographs

eShel and MUSICOS at Stará Lesná and Skalnaté Pleso, respectively. Although these spectra provided less precise radial velocities, there were more numerous and the fit of the radial velocity equation was more reliable. Some examples of the broadening functions of VW LMi have been already presented in Chapter 8. The broadening functions were then modeled by Gaussian and rotational profiles in order to obtain the radial velocities of the components. Finally, all together we obtained radial velocities for 222 times, 110 of them from eShel spectra and 112 from MUSICOS spectra. All the new radial velocities, together with the 48 new minima times are appended in Appendix A.

## 9.2 The orbital parameters

We proceeded the global fit of new data. Spectra from Stará Lesná and Skalnaté Pleso had different quality and as a consequence, the radial velocities determined from fits of the broadening functions had different quality, too. The new data from Skalnaté Pleso had significantly higher dispersion compared to the new data from Stará Lesná. By this reason we had decided to fit data from these observatories separately. For both separate fits the same photometric minima times were used.

### 9.2.1 Test fit of 2008 data

To make sure, that the *Orbit fitter* provides precise orbital parameters, we performed a test fit of radial velocities and minima times, that were used to determine the orbital parameters of VW LMi published in (Pribulla et al., 2008). The test was performed following the workflow presented in Chapter 8. From the individual fits of the datasets we determined the following average uncertainties:  $\sigma_{minima} = 0.0009$  day,  $\sigma_{RV1} = 10$  km s<sup>-1</sup>,  $\sigma_{RV2} = 11.5$  km s<sup>-1</sup>,  $\sigma_{RV3} = 3.5$  km s<sup>-1</sup>,  $\sigma_{RV4} = 3.2$  km s<sup>-1</sup>. The average uncertainties determined by Pribulla et al. (2008) were as follows:  $\sigma_{minima} = 0.0008$  day,  $\sigma_{RV1} = 11.3$  km s<sup>-1</sup>,  $\sigma_{RV2} = 13.1$  km s<sup>-1</sup>,  $\sigma_{RV3} = 2.6$  km s<sup>-1</sup>,  $\sigma_{RV4} = 2.2$  km s<sup>-1</sup>. As presented in Table 9.1 the parameters determined by *Orbit fitter* were in a close match with the parameters of Pribulla et al. (2008). The corresponding fits of radial velocity curves are presented in Figure 9.1. After being assured, that our software tool provides precise results, we advanced to the fit of 2018 data.

### 9.2.2 Fit of 2018 eShel data

As it was told in Chapter 8, the *Orbit fitter* uses different methods to obtain the orbital parameters from the best fits than the software tool of T. Pribulla. Therefore we had performed fits of the new data using both tools in order to compare both approaches.

From the individual fits of the new 2018 eShel datasets we determined the following average uncertainties:  $\sigma_{minima} = 0.0009$  day,  $\sigma_{RV1} = 8.5$  km s<sup>-1</sup>,  $\sigma_{RV2} = 9.5$  km s<sup>-1</sup>,  $\sigma_{RV3} = 1.15$  km s<sup>-1</sup>,  $\sigma_{RV4} = 0.95$  km s<sup>-1</sup>. The average uncertainties determined by T. Pribulla were as follows:  $\sigma_{minima} = 0.0009$  day,  $\sigma_{RV1} = 8.9$  km s<sup>-1</sup>,  $\sigma_{RV2} = 12.3$  km s<sup>-1</sup>,  $\sigma_{RV3} = 0.86$  km s<sup>-1</sup>,  $\sigma_{RV4} = 0.87$  km s<sup>-1</sup>. The complete set of the new orbital parameters of VW LMi is presented in Table 9.1 and the corresponding best fits are shown on Figure 9.2.

### 9.2.3 Fit of 2018 MUSICOS data

From the individual fits of the new 2018 MUSICOS datasets we determined the following average uncertainties:  $\sigma_{minima} = 0.0009$  day,  $\sigma_{RV1} = 4.4$  km s<sup>-1</sup>,  $\sigma_{RV2} = 11.2$  km s<sup>-1</sup>,  $\sigma_{RV3} = 0.55$  km s<sup>-1</sup>,  $\sigma_{RV4} = 1$  km s<sup>-1</sup>. The average uncertainties determined by T. Pribulla were as follows:  $\sigma_{minima} = 0.0009$  day,  $\sigma_{RV1} = 5.2$  km s<sup>-1</sup>,  $\sigma_{RV2} = 12.7$  km s<sup>-1</sup>,  $\sigma_{RV3} = 0.55$  km s<sup>-1</sup>,  $\sigma_{RV4} = 0.42$  km s<sup>-1</sup>. The complete set of the new orbital parameters of VW LMi is presented in Table 9.1 and the corresponding best fits are shown on Figure 9.3.

Parameter	2008*	2008	eShel*	eShel	MUSICOS*	MUSICOS	Unit
$V_0$	-0.15(25)	-0.149	-2.33(3.12)	-2.35	-2.59(2.56)	-2.5	[km.s <sup>-1</sup> ]
$Q$	1.63(9) 10 <sup>-10</sup>	1.633 10 <sup>-10</sup>	-6.0(7) 10 <sup>-12</sup>	-5.99 10 <sup>-12</sup>	1.4(9) 10 <sup>-11</sup>	1.4 10 <sup>-11</sup>	[days]
$P_{12}$	0.47755106(3)	0.47755127	0.47755451(6)	0.47755454	0.47755418(8)	0.47755409	[days]
$T_{12}$	52500.1497(2)	52500.15	52500.136(6)	52500.14	52500.14(4)	52500.14	[HJD]
$K_1$	105.8(1.0)	105.58	103.74(10.29)	105.82	104.31(6.15)	104.29	[km.s <sup>-1</sup> ]
$K_2$	250.2(1.2)	250.95	232.56(14.37)	234.55	241.86(15.1)	241.32	[km.s <sup>-1</sup> ]
$K_{12}$	21.61(49)	21.59	20.89(7.77)	21.11	22.50(6.16)	22.48	[km.s <sup>-1</sup> ]
$P_{34}$	7.93063(3)	7.93018	7.93033(4)	7.93027	7.93053(1)	7.929	[days]
$T_{34}$	52274.54(11)	52279.89	52220.38(2)	52220.43	52220.26(45)	52221.56	[HJD]
$e_{34}$	0.035(3)	0.035	0.040(6)	0.0398	0.041(9)	0.042	
$K_3$	63.99(23)	63.87	63.91(1.03)	62.55	63.81(1)	63.80	[km.s <sup>-1</sup> ]
$K_4$	63.53(27)	65.48	65.01(1.23)	64.09	65.3(7)	65.24	[km.s <sup>-1</sup> ]
$K_{34}$	23.22(33)	23.18	23.25(2.16)	23.23	21.38(2.89)	21.31	[km.s <sup>-1</sup> ]
$\omega_{34}$	1.90(9)	1.90	2.83(2)	2.80	2.84(2)	2.84	[rad]
$P_{1234}$	355.02(17)	355.008	356.091(1.8)	356.06	356.96(1.45)	356.78	[days]
$T_{1234}$	53046(6)	53048.896	53008.91(240)	53009.98	53093.18(88)	53092.29	[HJD]
$e_{1234}$	0.097(11)	0.097	0.026(9)	0.0262	0.049(9)	0.049	
$\omega_{1234}$	2.20(12)	2.21	2.042(4.2)	2.025	3.63(1.54)	3.60	[rad]
$\chi^2_{\nu}(RV1)$	1.086	1.21	1.02	1.08	1.19	1.02	
$\chi^2_{\nu}(RV2)$	1.058	1.02	0.99	1.00	1.04	1.01	
$\chi^2_{\nu}(RV3)$	0.862	1.09	0.99	1.06	0.99	1.31	
$\chi^2_{\nu}(RV4)$	0.851	0.86	1.03	1.16	0.98	0.75	
$\chi^2_{\nu}(MIN)$	1.086	1.05	1.03	0.81	0.98	0.97	

Table 9.1: Orbital parameters from the global fit of radial velocities and minima times. Columns marked with an asterisk are the results of T. Pribulla, the other columns are the results obtained via *Orbit fitter*. The periastron passage times  $T_i$  are stated in heliocentric julian days – 2400000 days.

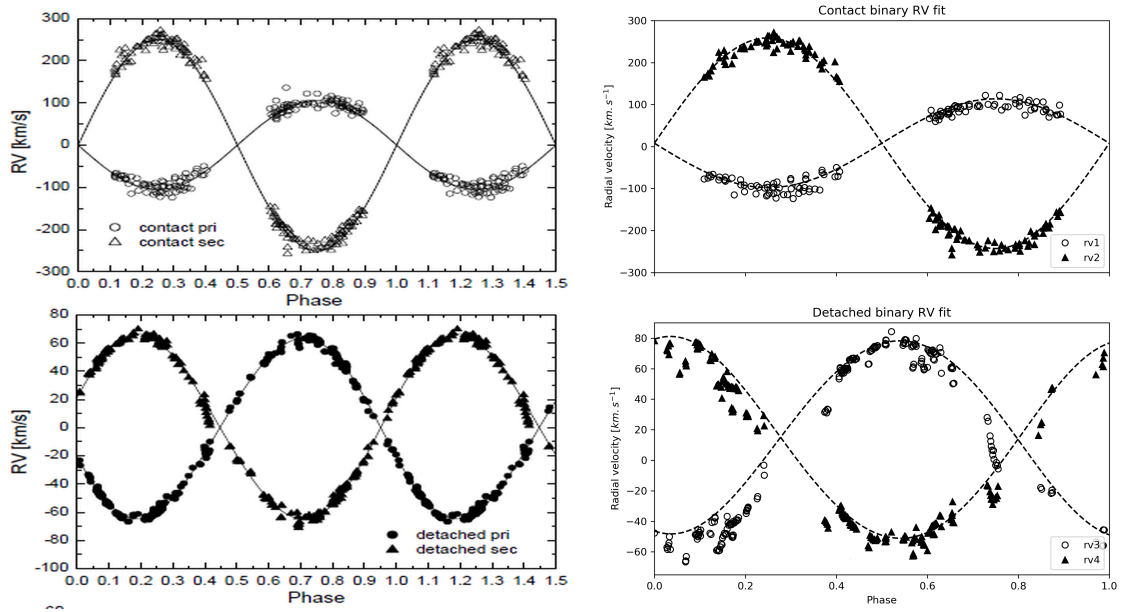


Figure 9.1: Test fits of VW LMi's radial velocities from 2008 data. Left to right: best fits of Pribulla et al. (2008), best fits obtained via *Orbit fitter*.

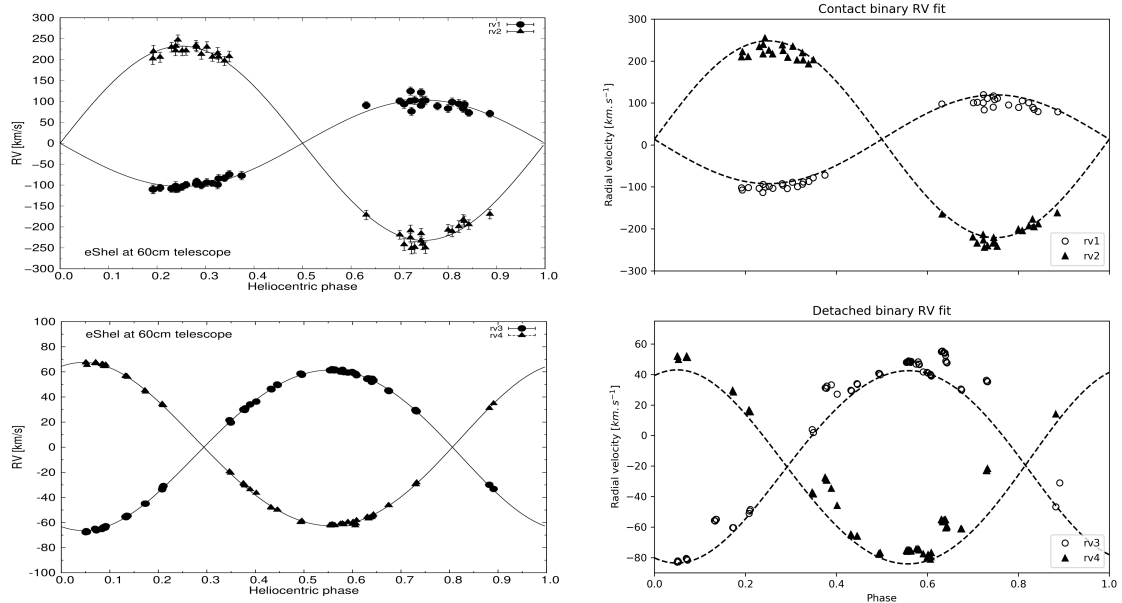


Figure 9.2: Best fits of VW LMi's radial velocities from 2018 eShel data. Left to right: best fits of T. Pribulla, best fits obtained via *Orbit fitter*.

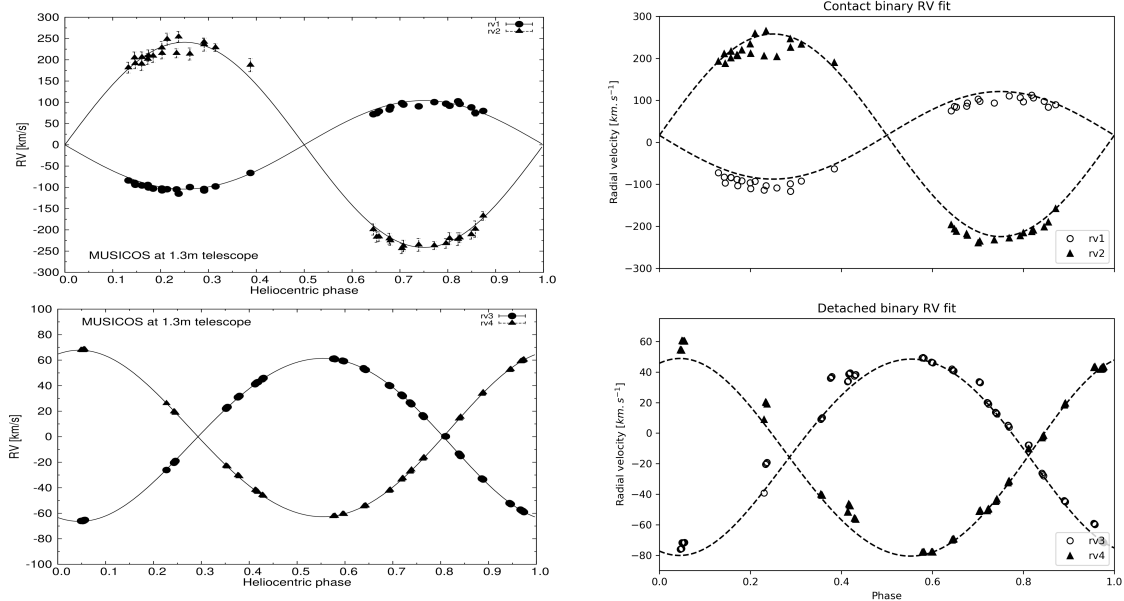


Figure 9.3: Best fits of VW LMi's radial velocities from 2018 MUSICOS data. Left to right: best fits of T. Pribulla, best fits obtained via *Orbit fitter*.

## 9.2.4 Fit of minima times

The fifth dataset that was fitted together with the radial velocities was the dataset of new minima times of VW LMi. Hereby, we present the  $(O - C)$  diagram of the new minima times.

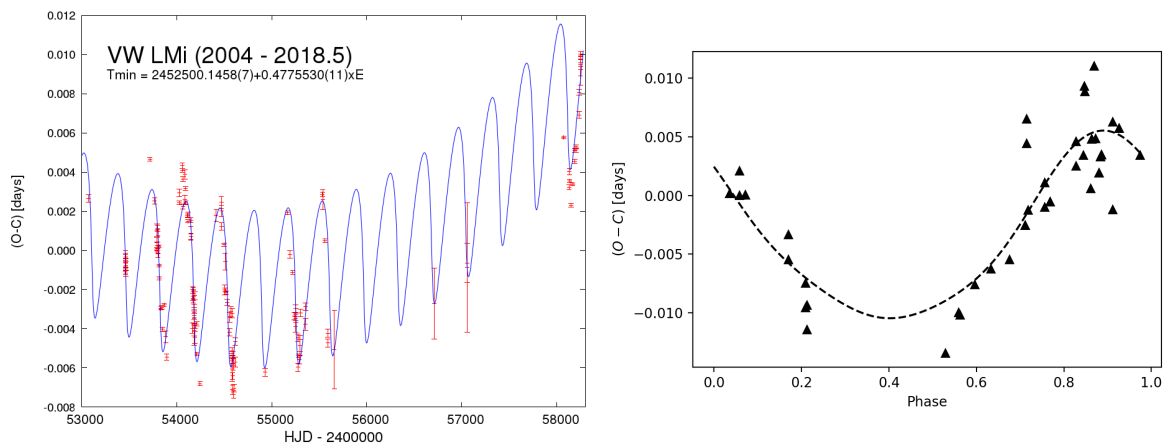


Figure 9.4: Left to right: Long-term  $(O - C)$  diagram with best fit by theoretical curve of LITE. Phase  $(O - C)$  diagram with best fit by theoretical curve of LITE, using parameters determined via *Orbit fitter*.

The minima times determined from photometric observations were fitted by the theoretical curve of LITE using parameters determined by the global fit of MUSICOS

data. In Figure 9.4 we present the best fits to the times of minima from 2004 to 2018.5 as well as the phase ( $O - C$ ) diagram of the new minima times. In Figure 9.4 we can clearly see the effect of LITE: the period of the sinusoidal curve is exactly one orbital period of VW LMi ( $\approx 355$  days) - caused by the revolution of the contact binary around the common barycenter of VW LMi.

### 9.3 Numerical integration of VW LMi

After the determination of the Keplerian orbital parameters of VW LMi we proceeded to the numerical integration of the quadruple's orbits. Using methods in module *Coordinates* we transformed the Keplerian orbital elements determined from global fit of radial velocities and minima times to cartesian position and velocity vectors at some arbitrary initial time. Module *Coordinates* requires the masses of individual components of VW LMi. These masses, as well as the inclinations of orbits with respect to the plane of sky were taken from (Pribulla et al., 2008) and they are presented in Table 3.2. As our numerical model is a point-mass model, it could not be used to integrate the motion of the contact binary. Therefore, we considered the contact binary system as one point mass with mass  $m_{12} = m_1 + m_2$  and we placed it to the mass center of the binary system. Thus, we studied the orbital perturbations in the orbit of the detached binary system and in the mutual wide orbit of VW LMi. We integrated the quadruple system for various intervals - 1 and 500 outer orbital periods of VW LMi (0.97 years and 485 years, respectively). All the orbital plots in this Section are the results of 1 period integration. In order to study long-term orbital evolution, we used the 500 period integrations. However, while performing numerical integration with the *N-body model* we realized, that our fourth-order Runge-Kutta integrator is insufficient for such tight (and massive) system as VW LMi, because after some periods of integration the system lost its stability. Because of the unstoppable marching of time that was slowly guiding us towards inevitable deadlines we had chosen to perform the 500 period integrations of the orbits using C/Python simulator ReboundX (Tamayo et al., 2016).

#### 9.3.1 Determining the longitudes of ascending nodes

The last Keplerian orbital parameters, which were necessary to compute VW LMi's cartesian position and velocity vectors were the longitudes of the ascending nodes of the detached binary's orbit ( $\Omega_{34}$ ) and the mutual wide orbit ( $\Omega_{1234}$ ). These important parameters one cannot determine from global fit of the observational data. As the inclination between the orbit of the detached binary and the mutual wide orbit ( $J_{mutual}$ )

directly depends on the difference of  $\Omega_{34}$  and  $\Omega_{1234}$  we proceeded the following way. We set the longitude of the ascending node  $\Omega_{34} = 0$ . Afterwards we performed numerical integrations for various values of  $\Omega_{1234}$ , from  $0^\circ$  up to  $360^\circ$  with  $30^\circ$  steps. Thus, we obtained twelve different results, which correspond for various values of inclinations between the detached binary's orbit the and mutual wide orbit. After transforming the results of the numerical integration to osculation Keplerian orbital elements via *Elements* module, we compared the results with observational orbital parameters of VW LMi - we were comparing observational values of eccentricities and arguments of perigee with their values obtained from numerical integrations. We found the best matches with the observational elements for the integrations with  $\Omega_{1234} = 0^\circ, 30^\circ, 330^\circ$ . In Figure 9.5 we present the orbits of VW LMi for these values of  $\Omega_{1234}$  as they are projected to the plane of sky. Our results imply, that the difference of  $\Omega_{34}$  and  $\Omega_{1234}$  must be a value from interval  $\langle 0^\circ, 0^\circ \pm 30^\circ \rangle$  and the true projection of VW LMi to the plane of sky must be similar like configurations shown in Figure 9.5.

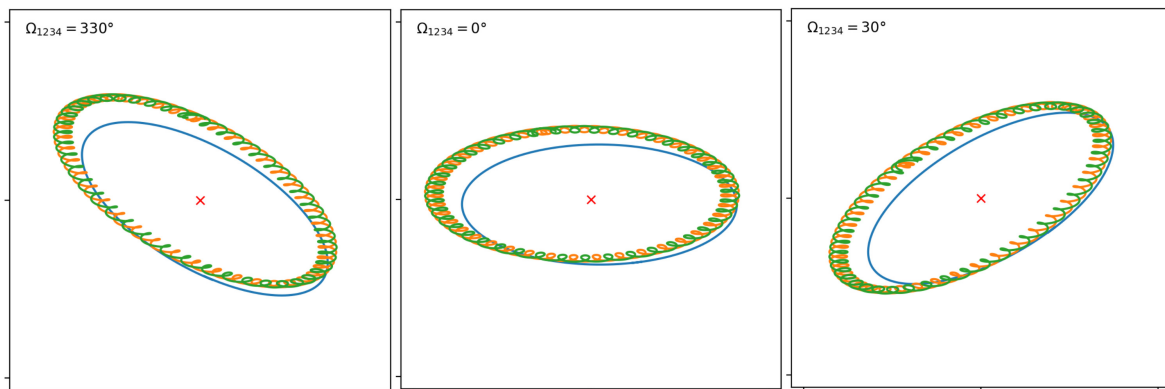


Figure 9.5: One period integrations of VW LMi for various values of  $\Omega_{1234}$  as projected to the plane of sky. Green and orange are the trajectories of the detached binary, blue is the trajectory of a contact binary considered as one mass point, while the red cross represents the mass center of the system. One unit on both axes is equal to 1 a.u.

### 9.3.2 The tightest quadruple system

We performed an integration of VW LMi's orbits with different settings. We set all the spatial angles ( $i, \Omega$ ) to zero to obtain perpendicular view to the orbital plane after plotting our results. Moreover, in this case we treated the contact binary as two separated objects. Our aim was to display how tight is the quadruple system VW LMi. The result of this integration is shown in Figure 9.6. The separation between the mass centers of the contact and detached system is only 1.62 a.u., the separation of components in the detached binary system is 0.1 a.u., while the separation of mass

centers of the contact binary is only 0.004 a.u. (approximately twice of the Earth-Moon distance). With these separations, VW LMi is the tightest quadruple system discovered yet.

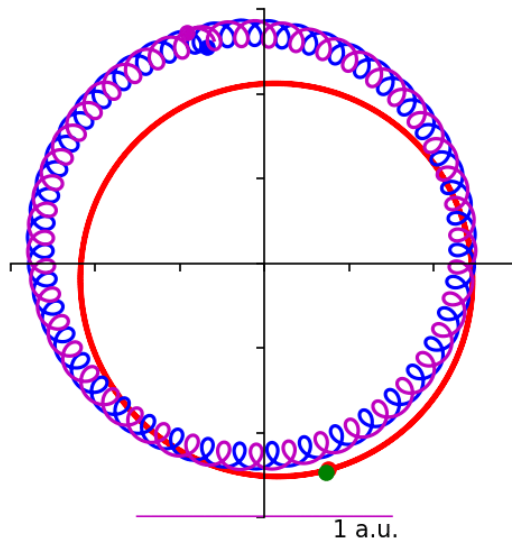


Figure 9.6: One period integration of VW LMi. Perpendicular view to the orbital plane. Blue and purple: trajectories of detached binary. Red: trajectory of the contact binary’s heavier component. Green: The less heavier component of the contact binary.

## 9.4 Secular orbital changes in orbits of VW LMi

The aim of the 500 period integrations was to study the long-term orbital evolution of the quadruple system VW LMi. Using module *Elements* we transformed the results of numerical integrations (cartesian position and velocity vectors) to Keplerian orbital parameters. *Elements*’s were developed to return the orbital elements we were interested in: orbital eccentricity  $e$ , inclination  $i$ , longitude of the ascending node  $\Omega$ , argument of periastron  $\omega$  and the angular momentum vector  $h$ . These were the orbital parameters, which changed in time as the observations proved  $(\omega, e)$ , or they cannot be determined from the observations  $(\Omega, i)$ . The angular momenta vectors were used to calculate the inclination between VW LMi’s two binary systems  $J_{mutual}$ , which cannot be determined from observations.  $J_{mutual}$  is simply the angle between the two angular momenta vectors. Note, that the inclinations  $i$  are the inclinations of VW LMi’s orbits with respect to the plane of sky, not the true mutual inclinations of orbits in the quadruple system. Our plots of the evolution of the orbital elements are shown in Figure 9.7. As described in Section 9.3.1, we studied the integrated orbits, where the initial value of  $\Omega_{1234}$  was set to values  $0^\circ, 30^\circ, 330^\circ$ . Therefore, Figure 9.7 compares the evolution of the elements for these three cases.

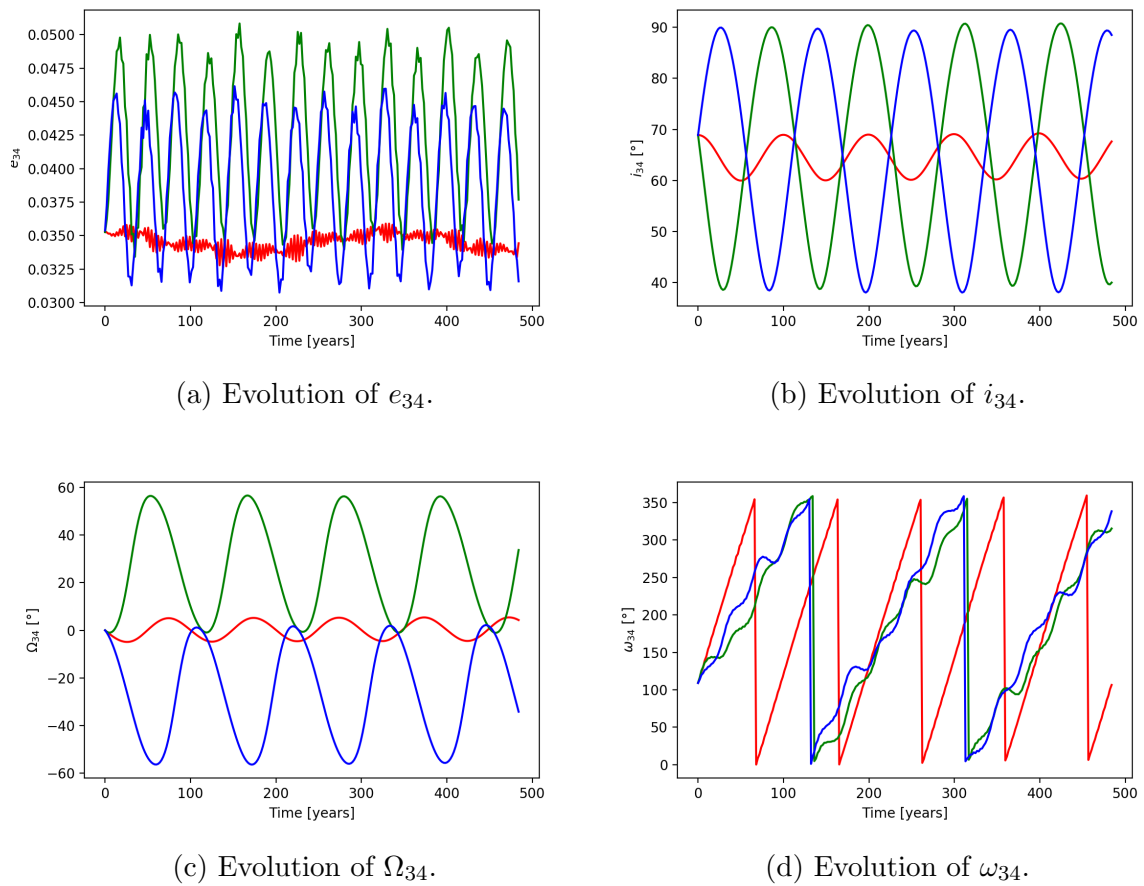


Figure 9.7: Long-term evolution of the orbital elements of VW LMi's detached binary's orbit for various initial values of  $\Omega_{1234}$ . Red curve:  $\Omega_{1234} = 0^\circ$ , green curve:  $\Omega_{1234} = 30^\circ$ , blue curve:  $\Omega_{1234} = 30^\circ$ .

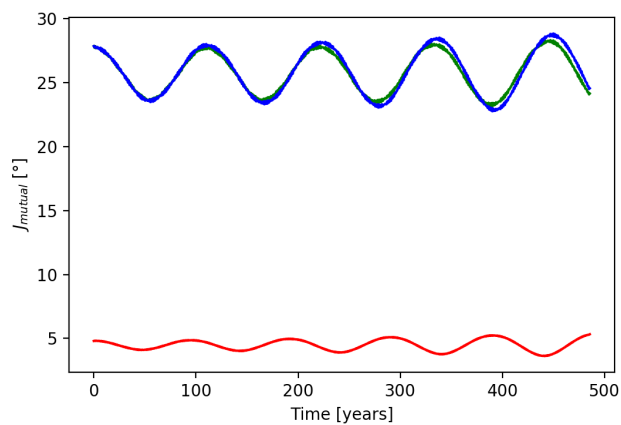


Figure 9.8: Long-term evolution of the inclination between both binaries of VW LMi for various initial values of  $\Omega_{1234}$ . Red curve:  $\Omega_{1234} = 0^\circ$ , green curve:  $\Omega_{1234} = 30^\circ$ , blue curve:  $\Omega_{1234} = 30^\circ$ .

Similarly, we studied the evolution of the inclination  $J_{mutual}$  as presented in Figure 9.8. Our results for the selected values of  $\Omega_{1234}$  are in a good match with observational parameters of VW LMi in Table 9.1.

### 9.4.1 Comparison with the observations

Comparing the plots in Figure 9.8 with the orbital parameters determined from MUSCOS (as they are more precise than eShel results) spectra presented in Table 9.1 we can conclude the following results.

#### Eccentricity $e_{34}$

The observational value of the eccentricity  $e_{34}$  is currently 0.042 and in 2008 it's value was 0.035. It means that the value of eccentricity oscillates at least between these two values. As we see in Figure 9.8 the best match for this interval is for  $\Omega_{1234} = 30^\circ$  and  $\Omega_{1234} = 330^\circ$ . Eccentricity oscillations with the least amplitude are present in case if  $\Omega_{1234} = 0^\circ$  - however, this setting does not match with our observations. As we cannot determine the exact value of  $\Omega_{1234}$  (just an interval  $\langle 0^\circ, 0^\circ \pm 30^\circ \rangle$ ) we can conclude, that the true eccentricity of the detached binary system of VW LMi varies in between value 0.03 and 0.05.

#### Inclination with respect to the plane of sky $i_{34}$

The value of the inclination of the detached binary system  $i_{34}$  was determined by Pribulla et al. (2008) as  $68.9^\circ$ . More exactly it was approximated as one cannot determine this orbital parameter from spectroscopic observations. This value could match with any of the results for various  $\Omega_{1234}$  presented in Figure 9.8. All we can conclude from the numerical integrations is that the value of  $i_{34}$  varies in between  $40^\circ$  and  $90^\circ$  with respect to the plane of sky.

#### Longitude of the ascending node $\Omega_{34}$

During our integrations the initial value of  $\Omega_{34}$  was set to  $0^\circ$  in order to determine the difference of  $\Omega_{34}$  and  $\Omega_{1234}$ . Our results shown in Figure 9.8 imply, that  $\Omega_{34}$  has different oscillation intervals for various values of  $\Omega_{1234}$ . For  $\Omega_{1234} = 0^\circ$  the value of  $\Omega_{34}$  varies between  $-5^\circ$  and  $5^\circ$ , for  $\Omega_{1234} = 30^\circ$  between  $-60^\circ$  and  $0^\circ$  and for  $\Omega_{1234} = 330^\circ$  between  $0^\circ$  and  $60^\circ$ . It implies that the difference of  $\Omega_{34}$  and  $\Omega_{1234}$  could reach the maximal value  $60^\circ$  just as we had determined in Section 9.3.1.

### Argument of periapsis $\omega_{34}$

The observational value of the argument of periapsis  $\omega_{34}$  is currently  $162.7^\circ$  and in 2008 it's value was  $108.9^\circ$ . It means that in the orbit of the detached binary is a definite apsidal motion - the orbit's periapsis moves  $53.8^\circ/\text{decade}$ . Using this observational value, we determined that the orbit's periapsis completes one revolution in 67 years. If we compare this values with the results of numerical integrations, we can see that the best match with this value is for the integration where  $\Omega_{1234}$  was set to  $0^\circ$ . In this case the periapsis completes one revolution in 100 years. The results for  $\Omega_{1234} = 30^\circ$  and  $\Omega_{1234} = 330^\circ$  are quite similar - in these cases the periapsis completes one revolution in not quite 200 years. As we obtained best match with observations for  $\Omega_{1234} = 0^\circ$  we conclude that the difference of  $\Omega_{34}$  and  $\Omega_{1234}$  must vary on an interval smaller than  $\langle 0^\circ, 0^\circ \pm 30^\circ \rangle$ . Also, as the period of periastron motion from integration for  $\Omega_{1234} = 0^\circ$  differs from the period determined from observations, we conclude that the contact binary system, if considered as a solid body (which is true in reality) causes perturbation in the orbit of the detached binary and therefore the observational period of periapsis motion is smaller than the period determined from integration in which we considered a point-mass model of VW LMi.

### Mutual inclination $J_{mutual}$

Is the inclination between both binaries of VW LMi.  $J_{mutual}$  is important as it determines the presence and scale of the Kozai-Lidov effect, see 2.18.  $J_{mutual}$  of VW LMi was not determined before. Our results shown in Figure 9.8 imply, that  $J_{mutual}$  does not reach the critical Kozai angle  $39.2^\circ$  for any of the values  $\Omega_{1234}$ . It means that the orbits of both binaries are almost coplanar and the Kozai-Lidov effect is not present in this quadruple system (anymore). The changes in orbits are caused by standard orbital perturbations in three-body problem, see *Lagrange planetary equations* in (Danby, 1992, chapter 11.5).

### Evolution of the mutual wide orbit

Using results from the numerical integrations we revealed the long-term evolution of VW LMi's mutual wide orbit. As expected, there are no significant changes in this orbit. It is not surprising - as stated in Section 2.3, in case of quadruple systems consisting of two binaries, the binary systems cause orbital perturbations in each others orbits, their mutual wide orbit is not affected.

# Chapter 10

## Conclusion

New observations of the VW Leonis Minoris proved the presence of secular orbital changes in this tight quadruple system. Obtained data included spectroscopic and photometric observations. To acquire spectroscopic elements of the system and to study their secular changes, new software tools had to be developed. In this final Chapter we discuss the accuracy of our software tools and take a closer look on the obtained results.

### 10.1 Discussing our software tools

The processing of spectra and photometric minima times followed the workflow presented in Figure 8.2. The new spectra were deconvolved in order to obtain the broadening functions and radial velocities of VW LMi's individual components in IDL using routines of Rucinski (1999). All the following data processing was carried out in our own software tools, developed especially for the needs of this thesis. These tools are: the *Orbit fitter*, *Coordinates*, *N-body model* and *Elements*. Modules *Coordinates* and *Elements* were used to transform Keplerian orbital elements to cartesian position and velocity vectors and vice versa. Using basic equations of celestial mechanics, these modules provided credible results and there is no need for further discussion. The main software tools were the *Orbit fitter* and the *N-body model*, which we discuss in the following dedicated sections.

#### 10.1.1 Orbit fitter

The first act performed with the *Orbit fitter* was the individual fit of the four datasets of radial velocities and one dataset of new minima times in order to determine the average uncertainties of each dataset. The determined average uncertainties presented in Section 9.2 are in a good match with the average uncertainties determined by T.

Pribulla. Also, these uncertainties have reasonable values if we compare them with the radial velocities of VW LMi's individual components. Using these average uncertainties we proceeded to the global fit of all datasets. As stated in Section 9.2, data from Stará Lesná and Skalnaté Pleso observatories were fitted separately because of their different quality. We compared the results of the *Orbit fitter* with the results of the software tool of T. Pribulla. Both software tools provided reasonable and comparable results. Thus, we conclude that the steepest descent and simplex numerical approach for the global fit of our data are both applicable and both provide adequate results.

### 10.1.2 N-body model

After we obtained the Keplerian orbital parameters of VW LMi via *Orbit fitter* we transformed these elements to cartesian position and velocity vectors at some initial time via *Coordinates* module. Afterwards we proceeded to numerical integrations of orbits using software tool *N-body model*. The software tool was previously tested - we created a numerical model of the Solar system (including the Sun, the planets and some comets). The numerical integration of the Solar system provided precise results, therefore we proceeded to the numerical integrations of VW LMi. The details and settings of the integrations were presented in Section 9.3. The *N-body model* provided precise results for 1 period integrations of VW LMi (outer orbital period  $\approx 355$  days). However, after integrations for more orbital periods we noticed, that the system had lost its stability. Simply the fourth-order Runge-Kutta integrator was insufficient for the integration of the quadruple system VW LMi. In this system there are four stars. Each of these stars has approximately the mass of the Sun and moreover they are very close to each other (0.1 a.u. in the case of the detached binary). To handle this quadruple system a higher-order Runge-Kutta method was required. Therefore, the long-term numerical integrations were obtained via *ReboundX* simulator and its fifteenth-order Runge-Kutta integrator *ias15*. With this integrator we were able to integrate VW LMi for 500 orbital periods without losing its stability. Our future plans involve implementation of a higher-order Runge-Kutta integrator (not necessary fifteenth-order) to our tool *N-body model* - a task, which was not incorporated in this thesis due to shortage of time.

## 10.2 Discussing our results

Hereby, we discuss our results obtained during the data processing. The main results are the radial velocities obtained in IDL, the Keplerian orbital parameters of VW LMi

obtained in the *Orbit fitter* and the various results from the numerical integration of VW LMi's orbits obtained in the *N-body model* and *ReboundX*.

### 10.2.1 Radial velocities and minima times

We processed spectra from Stará Lesná, Skalnaté Pleso & Tautenburg. The quality of spectra from various spectrographs differed widely - the best spectra were from Tautenburg observatory. However, since there were only few spectra available, we neglected the further use of the Tautenburg spectra. Thus, our results come from the spectra from the échelle spectrograph at Stará Lesná observatory and Skalnaté Pleso observatory. Although these spectra provided less precise radial velocities, there were more numerous. Thus, the further fit of the radial velocity equation was more reliable. All together, we obtained 222 new radial velocities of VW LMi, 110 from the eShel and 112 from the MUSICOS spectra. Also, we obtained 48 new minima times at the Stará Lesná observatory with a 18cm f/10 auxiliary Maksutov Cassegrain telescope attached to the Zeiss 60cm Cassegrain telescope. These 222 new radial velocities and 48 new minima times served as the input data to the *Orbit fitter* software tool.

### 10.2.2 Orbital parameters and secular orbital changes

All the orbital parameters of VW LMi determined from the observational data are shown in Table 9.1. The table contains results from two different approaches: columns marked with an asterisk are the results of T. Pribulla, who used steepest descent approach, while the remaining columns are the results obtained via *Orbit fitter* using simplex approach. First of all, we compare the results of these two approaches. As we can see, the results from the two approaches are in a good match and the  $\chi^2_\nu$ 's of both approaches are close to unity. In Figures 9.1, 9.2 and 9.3 the best fits of radial velocities for individual datasets are presented. As we can see, the best fits obtained via *Orbit fitter* result in a larger scatter of the observations after the correction for the outer/inner orbital motion. As the  $\chi^2_\nu$ 's of the fits are close to unity (which mean that the fits are good) the scattering could be caused by some aberration arising during the construction of the phase diagram. However, we did not find the mentioned bug, thus the best fits obtained via *Orbit fitter* remained more scattered. Comparing the results, we can conclude that both approaches return reliable values of the orbital parameters and the *Orbit fitter* developed for this thesis is a well-grounded software tool. As we concluded that the obtained results - orbital parameters of VW LMi are reliable, we compare the quadruple's orbital parameters from (Pribulla et al., 2008) with the new orbital parameters determined from the new observations. As discussed previously,

spectra from various observatories had different quality. As the highest quality spectra were from MUSICOS spectrograph from Skalnaté Pleso observatory, we compare the orbital parameters determined by the global fit to MUSICOS data with the orbital parameters from (Pribulla et al., 2008). As stated in section 2.3, secular orbital changes in quadruple stellar system are present in the orbits of individual binary systems (as they perturb each other's orbits). However, no orbital perturbations should occur in the mutual wide orbit of the quadruple system. Pribulla et al. (2008) showed, that secular orbital changes are present in the orbit of the detached binary system of the quadruple VW LMi.

### 10.2.3 Changes in the detached binary's orbit

As presented in Table 9.1, we found the presence of secular orbital changes in the orbit of the detached binary. The most visible change is in the argument of perigee  $\omega_{34}$ . While in 2008  $\omega_{34}$  was equal to 1.90 radians, our new value of  $\omega_{34}$  is 2.84 radians. It means that the orbit's periapsis moves 0.94 radians (or  $53.8^\circ$ ) per decade. Also, the eccentricity of the orbit increased from the value 0.035 in 2008 to the current value 0.042. However, the rate of this change was determined from the results of numerical integrations. As presented in Figure 9.8, the eccentricity of the detached binary's orbit oscillates between values 0.03 and 0.05. Also, using our results from the numerical integration of orbits we obtained the changes of orbital parameters  $i_{34}$  and  $\Omega_{34}$  (which one cannot obtain from spectroscopic observations). We can conclude from the numerical integrations that the value of  $i_{34}$  varies in between  $40^\circ$  and  $90^\circ$  with respect to the plane of sky. Our results also imply, that  $\Omega_{34}$  has different oscillation intervals for various values of  $\Omega_{1234}$ . For  $\Omega_{1234} = 0^\circ$  the value of  $\Omega_{34}$  varies between  $-5^\circ$  and  $5^\circ$ , for  $\Omega_{1234} = 30^\circ$  between  $-60^\circ$  and  $0^\circ$  and for  $\Omega_{1234} = 330^\circ$  between  $0^\circ$  and  $60^\circ$ . The remaining orbital parameters did not show the presence of striking orbital changes. As the spectroscopic semi-amplitudes  $K_3$  and  $K_4$  remained quite stable during the last decade we can also conclude, that the detached orbit and the mutual orbit of VW LMi are very close to coplanar.

### 10.2.4 Changes in the contact binary's orbit

In the presented orbital parameters shown in Table 9.1 we did not find significant orbital changes. Similarly to the detached binary, the spectroscopic semi-amplitudes  $K_1$  and  $K_2$  remained quite stable during the last decade we can also conclude, that the contact binary's orbit and the mutual orbit of VW LMi are very close to coplanar. Also, as our *N-body model* is a point-mass model, we considered the whole contact

binary system as one point mass. In this thesis we did not focus on the secular orbital changes in this binary system. For the reader interested in the orbital changes of this contact binary, we recommend to compare (Pribulla et al., 2008) with the article of Djurašević et al. (2013), which contains the photometric study of VW LMi.

### 10.2.5 Changes in the wide orbit

No secular orbital changes in the mutual orbit of VW LMi were expected. However, as presented in Table 9.1 we found changes in the mutual orbit's eccentricity  $e_{1234}$  and argument of perigee  $\omega_{1234}$ . In 2008 the value of  $e_{1234}$  was equal to 0.097 (Pribulla et al., 2008), while the new value of  $e_{1234}$  is 0.049. As for the argument of perigee  $\omega_{1234}$ : in 2008  $\omega_{1234}$  was equal to 2.20 radians, our new value of  $\omega_{1234}$  is 3.60 radians. These are similar changes in eccentricity and the argument of perigee as they are present in the detached binary's orbit. However, in case of the detached orbit, the secular orbital changes are caused by gravitational perturbations from the contact binary system - the mutual orbit should not be affected. In case that VW LMi is a quadruple stellar system. However, the changes in  $\omega_{1234}$  and  $e_{1234}$  are a serious clue, that there might be fifth component in this stellar system, which eventually causes secular perturbations in the mutual orbit of the quadruple VW LMi. As stated in Chapter 3, VW LMi (the quadruple system) forms a loose binary with star HD95606 as published in (Pribulla et al., 2008). In order to examine this relationship, we compared the parallaxes and mean motions of VW LMi and HD95606 from the latest Gaia data release (Gaia Collaboration et al., 2018). The parallax and the mean motion of VW LMi is  $\pi = 9.0488$  mas,  $\mu_\alpha = 13.303$  mas.yr<sup>-1</sup>,  $\mu_\delta = -6.083$  mas.yr<sup>-1</sup>, while the parallax and mean motion of HD95606 is  $\pi = 7.7238$  mas,  $\mu_\alpha = 12.720$  mas.yr<sup>-1</sup>,  $\mu_\delta = -4.469$  mas.yr<sup>-1</sup>. Although these parallaxes and mean motions have similar values, they are quite different to form a quintuple stellar system. It means that there might be a closer and yet undiscovered fifth component of VW LMi, which causes secular orbital changes of the mutual orbit of the quadruple system.

### 10.2.6 The longitudes of ascending nodes

One major result of the numerical integrations was the determination of the unknown longitudes of ascending nodes  $\Omega_{34}$  and  $\Omega_{1234}$ . As discussed in Section 9.3.1 these values one cannot determine - we could determine only the value of their difference. Therefore, we integrated the orbits of VW LMi for various settings as discussed in Section 9.3.1. Then we transformed the resulting position and velocity vectors to Keplerian orbital parameters and compared them with the orbital parameters determined from

observations. From the best matches, we implied that the difference of  $\Omega_{34}$  and  $\Omega_{1234}$  must be a value from interval  $\langle 0^\circ, 0^\circ \pm 30^\circ \rangle$ . This is an unprecedented result, never determined before.

### 10.2.7 The mutual inclination of the binaries

Another unprecedented result obtained in this thesis is the determination of the mutual inclination  $J_{mutual}$  in between the contact and detached orbits. This parameter is important because it can prove the presence of the Kozai-Lidov effect in the system VW LMi. As stated in Section 2.1, a minimal mutual inclination in between such orbits must reach the critical value  $39.2^\circ$  to manifest secular orbital changes due to the Kozai-Lidov effect. As stated in Section 9.4.1,  $J_{mutual}$  does not reach the critical Kozai angle  $39.2^\circ$ . It means that the Kozai-Lidov effect is not present in this quadruple system. The changes in orbits are caused by standard orbital perturbations in three-body problem.

## 10.3 Discussing the nature of secular perturbations

In this section we discuss the nature of the secular orbital perturbations in the quadruple system VW LMi. As it was stated in Section 10.2, the calculated value of inclination between the detached and mutual orbit implies that Kozai-Lidov oscillations are not present in this quadruple system any more. We concluded, that the perturbations are caused by standard orbital perturbations. Now, let's recall Section 2 where we described the Kozai-Lidov effect. The timescale of the secular orbital changes caused by the Kozai-Lidov effect could be calculated using Equation 2.24. However, we already proved that the Kozai-Lidov effect is not present in the system, we confirm our result by calculating the timescale of such oscillations using Equation 2.24. Furthermore, we calculate the timescale of Kozai-Lidov oscillations in quadruple systems using the Equation 2.25. The calculated timescales are shown in Table 10.1.

<b>Effect</b>	<b>Equation</b>	<b>Timescale</b>
Kozai-Lidov	2.24	14.07
Kozai-Lidov in quadruple systems	2.25	131.93

Table 10.1: Timescales (in years) of secular perturbations in the detached orbit.

As we see, the computed timescale of the Kozai-Lidov oscillations differs from the oscillation periods of the detached orbit's parameters presented in Figure 9.7. This just confirms our conclusion that the effect is not present in the system as the calculated

timescale is unrealistic. Although, if we consider the analytic solution of the Kozai-Lidov effect in quadruple systems and the timescale calculated using Equation 2.25 we obtain a result (132 years), which is similar to oscillation periods of the detached orbit's parameters presented in Figure 9.7. This result could mean, that Kozai-Lidov effect is eventually present in the quadruple system VW LMi and it is described by analytic solution of Vokrouhlický (2016). This quadruple system was even mentioned in (Vokrouhlický, 2016) as a perspective candidate to test the analytic solution. As we compare our results of numerical integrations with the timescale calculated using Equation 2.25 we can see, that the formulation of Vokrouhlický (2016) is in a close match with our results. Consequently, the changes in orbital parameters of VW LMi can be described by the analytical formulation of the Kozai-Lidov effect in quadruple systems as published by Vokrouhlický (2016). Describing the secular orbital changes through this approach might be eventually more accurate than describing them through *Lagrange's planetary equations*.

## 10.4 Overview

VW LMi is an exceptionally interesting stellar system. It is the tightest quadruple stellar system yet discovered and striking secular changes occur in its orbits. Both of the system's inner binaries act as perturbers on each other, thus causing secular orbital perturbations in each others orbits. In our work we proved the existence and the scale of these secular changes. Moreover, we determined the unprecedented values of the longitudes of the ascending nodes and the value of the mutual inclination in between the quadruples binaries. However, some additional questions arised. First of all, the existence of the contact binary could be a consequence of the Kozai-Lidov effect. Due to transport of the angular momentum of the (now) contact system to the distant perturber, its orbit could have shrunked until the two stars reached the Roche-limit and eventually became a contact binary. As stated in Chapter 2, the transport of the angular momentum is directly caused by the Kozai-Lidov effect. Secondly, even the mutual wide orbit of the quadruple system is extremely tight (1.62 a.u.). This tightness could have been caused by an extra and yet unknown companion of the quadruple system, which "stole" the inner system's angular momentum. This means that VW LMi is, or at some time interval was even a quintuple stellar system. However, both of these questions are difficult to answer. The first question would require a large-scale backward integration of the system, while the second one requires observations of VW LMi's closest stellar neighbours. All in all, our results are satisfactory. We had developed four fully functional software tools, which formed the data processing

---

pipeline for the needs of this thesis. The obtained results proved the presence of secular orbital changes in the orbits of VW LMi as forecasted by Pribulla et al. (2008) and finally, we showed that the Kozai-Lidov effect is not affecting the quadruple system anymore - but this effect is certainly responsible for the existence of this tight quadruple system.

# Bibliography

- Antognini, J. M. (2015). Timescales of kozai–lidov oscillations at quadrupole and octupole order in the test particle limit. *Monthly Notices of the Royal Astronomical Society*, 452(4):3610–3619.
- Baudrand, J. and Bohm, T. (1992). MUSICOS - A fiber-fed spectrograph for multi-site observations. *Astron. Astrophys.*, 259:711–719.
- Benz, W., Hills, J., and Thielemann, F.-K. (1989). Three-dimensional hydrodynamical simulations of stellar collisions. ii-white dwarfs. *The Astrophysical Journal*, 342:986–998.
- Bevington, P. R., Robinson, D. K., Blair, J. M., Mallinckrodt, A. J., and McKay, S. (1993). Data reduction and error analysis for the physical sciences. *Computers in Physics*, 7(4):415–416.
- Binnendijk, L. (1960). Properties of double stars; a survey of parallaxes and orbits. *NASA Planetary Data System*.
- Bowman, K. P. (2006). *An Introduction to Programming with IDL: Interactive data language*. Elsevier.
- Brouwer, D. (1959). Solution of the problem of artificial satellite theory without drag. *The Astronomical Journal*, 64:378.
- Cochran, W., Hatzes, A., Butler, R., and Marcy, G. (1996). Detection of a planetary companion to 16 cygni b. In *Bulletin of the American Astronomical Society*, volume 28, page 1111.
- Danby, J. (1992). Fundamentals of celestial mechanics. *Richmond: Willman-Bell*,—*c1992, 2nd ed.*
- Djurašević, G., Baştürk, Ö., Latković, O., Yılmaz, M., Çalışkan, Ş., Tanrıverdi, T., Şenavcı, H., Kılıçoğlu, T., and Ekmekçi, F. (2013). Photometric analysis of hs aqr, eg cep, vw lmi, and du boo. *The Astronomical Journal*, 145(3):80.

- Dumitrescu, A. (2000). BV Photometry of the Binary Star VW LMi. *Information Bulletin on Variable Stars*, 4952.
- Dumitrescu, A. (2003). Photometric Study of the Eclipsing Binary VW Leonis Minoris. *Romanian Astronomical Journal*, 13:119–123.
- Eggleton, P. P., Kiseleva, L. G., and Hut, P. (1998). The equilibrium tide model for tidal friction. *The Astrophysical Journal*, 499(2):853.
- Evans, D. S. (1968). Stars of Higher Multiplicity. *Quart. Jrn. Royal Astron. Soc.*, 9:388.
- Ford, E. B., Kozinsky, B., and Rasio, F. A. (2000). Secular evolution of hierarchical triple star systems. *The Astrophysical Journal*, 535(1):385.
- Gaia Collaboration, G., Brown, A., Vallenari, A., Prusti, T., de Bruijne, J., Babusiaux, C., and Bailer-Jones, C. (2018). A&a (special issue on gaia data release 2). *preprint*.
- Gomez-Forrellad, J. M., Vidal-Sainz, J., Sanchez-Bajo, F., and Garca-Melendo, E. (2003). Photometric Observations of VW LMi and the New Binary System V345 Gem. *Information Bulletin on Variable Stars*, 5387.
- Goodwin, S. P. and Kroupa, P. (2005). Limits on the primordial stellar multiplicity. *Astronomy & Astrophysics*, 439(2):565–569.
- Gray, D. F. (2005). *The Observation and Analysis of Stellar Photospheres*.
- Griffin, J. (1967). Jj griffin, phys. lett. 24b, 5 (1967). *Phys. Lett.*, 24:5.
- Guenther, E. W., Hartmann, M., Esposito, M., Hatzes, A. P., Cusano, F., and Gandolfi, D. (2009). A substellar component orbiting the F-star 30 Arietis B. *Astron. Astrophys.*, 507:1659–1665.
- Harrington, R. S. (1968). Dynamical evolution of triple stars. *The Astronomical Journal*, 73:190–194.
- Hartmann, M., Guenther, E. W., and Hatzes, A. P. (2010). A Sub-stellar Companion around the F7 V Star HD 8673. *Astrophys. J.*, 717:348–356.
- Hatzes, A. P., Guenther, E. W., Endl, M., Cochran, W. D., Döllinger, M. P., and Bedalov, A. (2005). A giant planet around the massive giant star HD 13189. *Astron. Astrophys.*, 437:743–751.
- Hilditch, R. W. (2001). *An Introduction to Close Binary Stars*.

- Hilditch, R. W. (2001). *An introduction to close binary stars*. Cambridge University Press.
- Hog, E., Fabricius, C., Makarov, V. V., Urban, S., Corbin, T., Wycoff, G., Bastian, U., Schwekendiek, P., and Wicenc, A. (2000). The tycho-2 catalogue of the 2.5 million brightest stars. Technical report, NAVAL OBSERVATORY WASHINGTON DC.
- Katz, B. and Dong, S. (2012). The rate of wd-wd head-on collisions may be as high as the sne ia rate. *arXiv preprint arXiv:1211.4584*.
- Kiseleva, L., Eggleton, P., and Mikkola, S. (1998). Tidal friction in triple stars. *Monthly Notices of the Royal Astronomical Society*, 300(1):292–302.
- Kozai, Y. (1962). Secular perturbations of asteroids with high inclination and eccentricity. *The Astronomical Journal*, 67:591.
- Kwee, K. and Van Woerden, H. (1956). A method for computing accurately the epoch of minimum of an eclipsing variable. *Bulletin of the Astronomical Institutes of the Netherlands*, 12:327.
- Landsman, W. (1993). The idl astronomy user’s library. In *Astronomical Data Analysis Software and Systems II*, volume 52, page 246.
- Lehmann-Filhés, R. (1894). Ueber die bestimmung einer doppelsternbahn aus spektroskopischen messungen der im visionsradius liegenden geschwindigkeitscompo-  
nente. *Astronomische Nachrichten*, 136(2):17–30.
- Lidov, M. (1962). The evolution of orbits of artificial satellites of planets under the action of gravitational perturbations of external bodies. *Planetary and Space Science*, 9(10):719–759.
- Lithwick, Y. and Naoz, S. (2011). The eccentric kozai mechanism for a test particle. *The Astrophysical Journal*, 742(2):94.
- Naoz, S. (2016). The eccentric kozai-lidov effect and its applications. *Annual Review of Astronomy and Astrophysics*, 54:441–489.
- Naoz, S., Farr, W. M., Lithwick, Y., Rasio, F. A., and Teyssandier, J. (2011). Hot jupiters from secular planet–planet interactions. *Nature*, 473(7346):187.
- Nelder, J. A. and Mead, R. (1965). A simplex method for function minimization. *The computer journal*, 7(4):308–313.

- Newville, M., Stensitzki, T., Allen, D. B., Rawlik, M., Ingargiola, A., and Nelson, A. (2016). Lmfit: non-linear least-square minimization and curve-fitting for python. *Astrophysics Source Code Library*.
- Pejcha, O., Antognini, J. M., Shappee, B. J., and Thompson, T. A. (2013). Greatly enhanced eccentricity oscillations in quadruple systems composed of two binaries: implications for stars, planets and transients. *Monthly Notices of the Royal Astronomical Society*, 435(2):943–951.
- Perets, H. B. and Fabrycky, D. C. (2009). On the triple origin of blue stragglers. *The Astrophysical Journal*, 697(2):1048.
- Press, W. H., Flannery, B. P., and Teukolsky, S. A. (1986). *Numerical recipes. The art of scientific computing*.
- Pribulla, T., Baluďanský, D., Dubovský, P., Kudzej, I., Parimucha, Š., Siwak, M., and Vaňko, M. (2008). VW LMi: tightest quadruple system known. Light-time effect and possible secular changes of orbits. *Mon. Not. R. Astron. Soc.*, 390:798–806.
- Pribulla, T., Garai, Z., Hambálek, L., Kollár, V., Komžík, R., Kundra, E., Nedoroščík, J., Sekeráš, M., and Vaňko, M. (2015). Affordable échelle spectroscopy with a 60 cm telescope. *Astronomische Nachrichten*, 336(7):682–689.
- Pribulla, T. and Rucinski, S. M. (2006). Contact binaries with additional components. i. the extant data. *The Astronomical Journal*, 131(6):2986.
- Pribulla, T., Rucinski, S. M., Lu, W., Mochnacki, S. W., Conidis, G., Blake, R. M., DeBond, H., Thomson, J. R., Pych, W., Ogłóza, W., and Siwak, M. (2006). Radial Velocity Studies of Close Binary Stars. XI. *Astron. J.*, 132:769–780.
- Pych, W. (2004). A Fast Algorithm for Cosmic-Ray Removal from Single Images. *Publ. Astron. Soc. Pac.*, 116:148–153.
- Rein, H. and Spiegel, D. S. (2014). Ias15: a fast, adaptive, high-order integrator for gravitational dynamics, accurate to machine precision over a billion orbits. *Monthly Notices of the Royal Astronomical Society*, 446(2):1424–1437.
- Rucinski, S. (1999). Determination of Broadening Functions Using the Singular-Value Decomposition (SVD) Technique. In Hearnshaw, J. B. and Scarfe, C. D., editors, *IAU Colloq. 170: Precise Stellar Radial Velocities*, volume 185 of *Astronomical Society of the Pacific Conference Series*, page 82.

- Rucinski, S. (1999). Spectral broadening functions. *Turkish Journal of Physics*, 23(2):271–288.
- Ruciński, S. M. (1973). The W UMa-type Systems as Contact Binaries. I. Two Methods of Geometrical Elements Determination. Degree of Contact. *Acta Astron.*, 23:79.
- Sánchez-Bajo, F. and Garcia-Melendo, E. (2007). Gómez-forrellad jm, 2007. *Ap&SS*, 312:151.
- Selam, S. O. (2004). Key parameters of W UMa-type contact binaries discovered by HIPPARCOS. *Astron. Astrophys.*, 416:1097–1105.
- Skrutskie, M., Cutri, R., Stiening, R., Weinberg, M., Schneider, S., Carpenter, J., Beichman, C., Capps, R., Chester, T., Elias, J., et al. (2006). The two micron all sky survey (2mass). *The Astronomical Journal*, 131(2):1163.
- Soker, N. and Tytenda, R. (2006). Violent stellar merger model for transient events. *Monthly Notices of the Royal Astronomical Society*, 373(2):733–738.
- Sterken, C. (2005). The oc diagram: basic procedures. In *The Light-Time Effect in Astrophysics: Causes and cures of the OC diagram*, volume 335, page 3.
- Tamayo, D., Rein, H., and Shi, P. (2016). Reboundx: A library for adding additional effects to n-body simulations. In *AAS/Division of Dynamical Astronomy Meeting# 47*, volume 47.
- Tamuz, O., Mazeh, T., and Zucker, S. (2005). Correcting systematic effects in a large set of photometric light curves. *Monthly Notices of the Royal Astronomical Society*, 356(4):1466–1470.
- Thizy, O. and Cochard, F. (2011). Spectrographs for small telescopes. In Neiner, C., Wade, G., Meynet, G., and Peters, G., editors, *Active OB Stars: Structure, Evolution, Mass Loss, and Critical Limits*, volume 272 of *IAU Symposium*, pages 282–283.
- Tokovinin, A. (2004a). Statistics of multiple stars. In *International Astronomical Union Colloquium*, volume 191, pages 7–14. Cambridge University Press.
- Tokovinin, A. (2004b). Statistics of multiple stars. In *International Astronomical Union Colloquium*, volume 191, pages 7–14. Cambridge University Press.
- Tokovinin, A. (2008). Comparative statistics and origin of triple and quadruple stars. *Mon. Not. R. Astron. Soc.*, 389:925–938.

- Tokovinin, A. (2018). The updated multiple star catalog. *The Astrophysical Journal Supplement Series*, 235(1):6.
- Tokovinin, A. A. (1997). MSC - a catalogue of physical multiple stars. *Astron. Astrophys., Suppl.*, 124:75–84.
- Vokrouhlický, D. (2016). Secular dynamics of gravitationally bound pair of binaries. *Mon. Not. R. Astron. Soc.*, 461:3964–3975.
- Weinersmith, Z. (2017). *Science: Abridged Beyond the Point of Usefulness*. Goodreads.
- Wolf, M. (2014). Light-time effect as a valuable tool in stellar astrophysics. *Contributions of the Astronomical Observatory Skalnaté Pleso*, 43:493–497.
- Zasche, P. (2005). Eclipsing binaries showing light–time effect. *Astrophysics and Space Science*, 296(1-4):127–130.

# Appendix A

## New radial velocities and minima times

HJD [days]	Epoch [days]	HJD [days]	Epoch [days]
2454931.362	5091	2456709.534	8814.5
2455168.714	5588	2457056.478	9541
2455192.589	5638	2457056.717	9541.5
2455220.525	5696.5	2458073.673	11671
2455235.566	5728	2458127.633	11784
2455249.414	5757	2458133.365	11796
2455249.415	5757	2458134.797	11799
2455253.474	5765.5	2458149.6	11830
2455253.474	5765.5	2458073.673	11671
2455274.484	5809.5	2458127.633	11784
2455274.485	5809.5	2458133.365	11796
2455280.454	5822	2458134.797	11799
2455290.482	5843	2458149.6	11830
2455295.497	5853.5	2458166.793	11866
2455295.497	5853.5	2458188.762	11912
2455304.334	5872	2458188.762	11912
2455356.386	5981	2458201.656	11939
2455356.387	5981	2458201.656	11939
2455534.52	6354	2458236.52	12012
2455535.714	6356.5	2458236.519	12012
2455560.545	6408.5	2458250.371	12041
2455589.431	6469	2458250.37	12041
2455589.432	6469	2458251.326	12043
2455659.393	6615.5	2458251.327	12043

Table A.1: New minima times.

HJD	RV1	RV2	HJD	RV3	RV4	HJD	RV3	RV4
[days]	[km.s <sup>-1</sup> ]	[km.s <sup>-1</sup> ]	[days]	[km.s <sup>-1</sup> ]	[km.s <sup>-1</sup> ]	[days]	[km.s <sup>-1</sup> ]	[km.s <sup>-1</sup> ]
2457753.634	78.57	-200.87	2457753.613	40.45	-18.71	2458133.546	55.55	-53.66
2457774.593	117.22	-216.42	2457753.624	39.62	-18.98	2458133.557	54.14	-53.55
2457774.604	113.99	-223.23	2457753.634	39.43	-17.4	2458188.386	43.53	-79.75
2457780.596	-105.65	207.49	2457774.593	33.22	-25.55	2458188.398	43.52	-80.38
2457780.606	-100.95	200.7	2457774.604	32.99	-26.29	2458188.408	43.90	-79.58
2457780.618	-88.74	191.36	2457774.615	32.88	-27.2	2458188.422	44.42	-79.82
2457797.505	101.81	-218.11	2457774.626	34.21	-27.47	2458188.433	43.80	-79.5
2457797.516	101.91	-225.12	2457780.596	-54.53	57.62	2458188.443	44.01	-80.14
2457797.526	91.24	-232.47	2457780.606	-54.81	57.33	2458188.455	43.43	-80.23
2457814.455	-103.45	226.35	2457780.618	-53.68	57.39	2458188.467	44.08	-80.03
2457843.388	103.63	-145.62	2457780.629	-53.75	56.67	2458188.556	42.38	-78.87
2457843.398	97.8	-192.67	2457782.633	34.22	-33.57	2458188.589	43.79	-78.69
2457843.409	109.1	-184.27	2457800.489	47.68	-61.63	2458188.601	42.30	-79.47
2457844.357	113.45	-195.62	2457800.500	46.73	-61.34	2458188.612	42.00	-79.37
2457844.368	97.65	-168.22	2457800.510	46.51	-60.51	2458200.408	-85.92	45.9
2457845.329	87.92	-179.27	2457814.455	24.43	-48.5	2458200.418	-86.40	46.64
2457854.346	93.14	-234.48	2457840.405	25.31	-66.34	2458200.428	-87.14	45.7
2457854.357	117.74	-224.23	2457840.415	24.76	-66.37	2458203.383	28.35	-71.56
2458133.483	-115.5	215.06	2457843.388	-88.27	46.68	2458203.394	27.97	-71.57
2458133.493	-105.42	214.8	2457843.398	-87.49	46.63	2458217.364	-57.54	10.44
2458133.504	-97.77	223.3	2457843.409	-88.11	44.6	2458217.375	-55.80	9.58
2458133.525	-90.65	200.14	2457844.357	-65.82	24.29	2458217.385	-54.93	9.15
2458133.536	-80.72	200.99	2457844.368	-65.78	23.22	2458218.465	-2.58	-43.61
2458188.386	-94.78	217.67	2457854.346	23.56	-70.8	2458218.488	-4.48	-44.7
2458188.398	-96.66	241.53	2457854.357	23.17	-71.34	2458220.400	35.13	-83.99
2458188.408	-92.06	232.81	2458073.634	-45.36	85.67	2458236.331	34.57	-86.56
2458188.422	-85.24	245.9	2458073.644	-44.71	85.84	2458236.347	34.05	-84.93
2458188.433	-81.78	241.86	2458073.655	-44.63	85.34	2458236.382	33.29	-87.83
2458188.443	-86.72	226.93	2458073.665	-43.92	84.24	2458236.393	32.75	-86.29
2458188.467	-65.21	134.03	2458073.676	-44.10	84.18	2458236.403	32.05	-83.56
2458203.394	106.38	-155.91	2458073.686	-44.33	83.97	2458251.347	33.98	-84.17
2458217.364	88.72	-151.7	2458073.697	-43.16	85.31	2458251.359	33.88	-84.47
2458218.465	-92.15	219.9	2458127.617	-28.86	39.12	2458251.371	33.15	-83.44
2458218.488	-84.25	250.04	2458133.483	56.52	-53.47	2458262.363	-52.96	7.91
2458220.400	-90.7	265.07	2458133.493	56.94	-53.92			
2458236.382	112.39	-223.18	2458133.504	56.93	-54.93			
2458236.393	121.68	-229.73	2458133.525	56.10	-54.23			
2458236.403	121.41	-230.72	2458133.536	55.74	-53.86			

Table A.2: New radial velocities obtained from spectra taken with eShel spectroscope of Stará Lesná observatory.

HJD [days]	RV1 [km.s <sup>-1</sup> ]	RV2 [km.s <sup>-1</sup> ]	HJD [days]	RV3 [km.s <sup>-1</sup> ]	RV4 [km.s <sup>-1</sup> ]	HJD [days]	RV3 [km.s <sup>-1</sup> ]	RV4 [km.s <sup>-1</sup> ]
2457781.477	-98.99	186.24	2457781.477	-18.62	21.49	2458230.338	-38.08	-7.46
2457781.491	-105.42	204.72	2457781.491	-17.96	21.21	2458231.328	-80.21	35.75
2457781.504	-112.2	210.19	2457781.504	-17.25	20.3	2458231.34	-80.62	36.04
2457843.421	92.28	-180.83	2457843.421	-84.33	49.54	2458231.351	-81.11	36.21
2458107.688	-121.7	198.33	2457843.435	-84.04	49.66	2458231.365	-81.23	36.5
2458107.701	-116.16	196.71	2457843.448	-83.87	49.46	2458231.376	-81.73	37.17
2458107.715	-124.29	218.78	2458107.688	43.42	-17.78	2458236.31	36.44	-83.92
2458166.501	-59.47	194.06	2458107.701	43.92	-17.98	2458236.323	36.25	-83.75
2458168.534	79.28	-191.72	2458107.715	44.54	-18.71	2458236.336	35.95	-83.97
2458168.55	90.36	-213.35	2458155.579	37.25	-47.22	2458241.325	-49.31	2.87
2458168.564	102	-230.64	2458155.593	37.67	-47.78	2458242.31	-1.17	-45.98
2458168.579	97.94	-227.92	2458155.606	37.94	-48.43	2458242.324	-0.42	-46.35
2458179.348	-92.48	252.92	2458168.534	-75.6	58.28	2458242.338	0.05	-46.66
2458179.36	-86.5	240.04	2458168.55	-75.53	58.21	2458245.354	3.66	-50.66
2458186.442	-75.86	218.45	2458168.564	-75.71	57.95	2458245.368	3.17	-50.03
2458186.456	-80.84	215.24	2458168.579	-75.49	58.2	2458245.383	2.41	-49.05
2458186.47	-89.19	241.75	2458179.348	28.02	-55.03	2458268.382	33.21	-75.28
2458223.456	95.88	-195.32	2458179.36	28.51	-55.14	2458268.393	32.48	-74.81
2458231.34	-73	212.12	2458179.467	31.8	-59.01	2458268.407	32.2	-74.74
2458231.351	-80.81	231.06	2458179.478	32.61	-59.21	2458268.418	31.92	-74.45
2458231.365	-82.29	270.54	2458179.489	32.78	-59.66	2458269.358	-3.52	-37.7
2458231.376	-92.74	276.06	2458182.498	-13.82	-13.82	2458269.37	-3.93	-37
2458242.31	-61.49	203.78	2458182.51	-13.9	-13.9	2458269.382	-4.79	-36.49
2458242.324	-73.3	228.07	2458212.364	39.96	-83.58	2458270.339	-52.89	13.29
2458269.358	119.6	-217.95	2458212.38	40.19	-83.41	2458270.35	-53.25	13.9
2458269.37	115.75	-212.9	2458212.395	39.72	-83.3	2458270.362	-53.64	14.55
2458269.382	121.53	-202.94	2458223.428	-80.47	37.16	2458530.506	28.95	-54.12
2458270.339	115.2	-199.64	2458223.441	-81.01	37.27	2458530.518	28.51	-53.58
2458270.35	107.02	-192.17	2458223.456	-81.63	37.76	2458530.529	28.3	-53.21
2458270.362	98.56	-148.35	2458229.354	10	-56.79	2458532.506	-64.15	39.93
2458531.48	88.82	-206.29	2458229.367	9.6	-55.92	2458532.517	-64.52	40.35
2458531.492	98.92	-215.57	2458229.38	8.94	-55.53	2458532.529	-65.01	40.66
2458531.503	107.91	-233.88	2458230.306	-36.33	-9.02			
2458532.506	102.09	-210.03	2458230.321	-37.14	-8.28			

Table A.3: New radial velocities obtained from spectra taken with MUSICOS spectro-  
scope of Skalnaté pleso observatory.

# Appendix B

## The orbit fitter

```

1 """
2 @author: Emil Puha
3         Orbit fitter
4 """
5 %% Library import
6
7 from lmfit import Parameters, report_fit, minimize
8 from numpy import cos, sin, pi, linspace, concatenate
9 import matplotlib.pyplot as plt
10 import pandas as pd
11
12 %% Import data
13 '''
14 Import data using pandas library and convert to float64.
15 '''
16
17 hjd = pd.read_csv('*.txt', delimiter = "\t", header=None)
18 rv1 = pd.read_csv('*.txt', delimiter = "\t", header=None)
19 rv2 = pd.read_csv('*.txt', delimiter = "\t", header=None)
20 rv3 = pd.read_csv('*.txt', delimiter = "\t", header=None)
21 rv4 = pd.read_csv('*.txt', delimiter = "\t", header=None)
22 e = pd.read_csv('*.txt', delimiter = "\t", header=None)
23
24 hjds = hjd[0].values
25 rad1 = rv1[1].values
26 rad2 = rv2[1].values
27 rad3 = rv3[1].values
28 rad4 = rv4[1].values
29 minima = e[0].values
30 epochs = e[1].values
31
32 %% Functions
33 '''
34 All the functions used during the fit and plotting.
35 '''
36
37 def mean(t, P, T):
38     '''
39     Mean anomaly equation
40     '''

```

```

41     M = ((2*pi)/P)*(t-T)
42     return M
43
44 def true(t,P,T,e):
45     '''
46     True anomaly truncated series
47     '''
48     phi = mean(t,P,T)+2*e*sin(mean(t,P,T))+1.25*(e)**2*sin(2*mean(t,P,T))
49     return phi
50
51 def lite(x,T,P,K,O,e):
52     '''
53     The light-time effect (LITE) equation
54     '''
55     c = 299792.458
56     M = (((2*pi)/P)*(x-T))
57     phi = M + 2*e*sin(M) + (1.25)*((e)**2)*(sin(2*M))
58     dt = ((K*P*(1-e)**(1.5))/(2*pi*c))*((sin(phi +O))/(1 +e*cos(phi)))
59     return dt
60
61 def Tmin(E,HJD,T,P,Q,K,e,O,Tij,Pij):
62     '''
63     Minima times equation
64     '''
65     c = 299792.458 # km/s
66     M = mean(HJD,P,T)
67     phi = M + 2*e*sin(M) + (1.25)*((e)**2)*(sin(2*M))
68     dt = ((K*P*(1-e)**(1.5))/(2*pi*c))*((sin(phi +O))/(1 +e*cos(phi)))
69     t = Tij + Pij*E +Q*E**2 + dt
70     return t
71
72 def rv(hjd,m,n,V0,Ki,Kij,e1234,eij,Oij,O1234,T1234,Tij,P1234,Pij):
73     '''
74     The radial velocity equation
75     '''
76     radvel = V0+(m)*Kij*(e1234*cos(O1234)\
77                 +cos(O1234+true(hjd,P1234,T1234,e1234)))\
78                 +((-1)**(n+1))*Ki*(cos(Oij+true(hjd,Pij,Tij,eij)))
79     return radvel
80
81 def mc(hjd,m,Kij,e1234,O1234,T1234,P1234):
82     '''
83     The equation of the mass center
84     '''
85     center = (m)*Kij*(e1234*cos(O1234)\
86                 +cos(O1234+true(hjd,P1234,T1234,e1234)))
87     return center
88
89 # %% Parameters
90 '''
91 Creating lmfit Parameters class. Includes all parameters to be optimized with their
92 initial guesses.
93 '''
94 p = Parameters()
95 p.add('V0', value=-2.5)

```

```

96 p.add('Q', value=0.0000000001)
97 p.add('P12', value=0.47755100)
98 p.add('T12', value=2452500.14)
99 p.add('K1', value=104)
100 p.add('K2', value=241)
101 p.add('K12', value=22)
102 p.add('P34', value=7.93)
103 p.add('e34', value=0.04)
104 p.add('T34', value=2452220.26)
105 p.add('K3', value=64)
106 p.add('K4', value=65)
107 p.add('K34', value=21)
108 p.add('omega34', value=2.5)
109 p.add('P1234', value=356)
110 p.add('e1234', value=0.05)
111 p.add('T1234', value=2453093.18)
112 p.add('omega1234', value=3.5)
113
114 # %% FIT ONE
115 '''
116 Separate residual dunctions of the datasets to determine average uncertainties from
    separate fitting. Values of sigma are changed until reduced Chi-squared is equal (
    or close) to unity.
117 '''
118
119 def funcRV1(p, x=hjds[:34], dat1=rad1):
120     model1 = rv(x,1,1,p['V0'],p['K1'],p['K12'],p['e1234'],0,pi/2,
121                p['omega1234'],p['T1234'],p['T12'],p['P1234'],p['P12'])
122     sigma1 = 1
123     residual1 = (dat1 - model1)/sigma1
124     return residual1
125
126 def funcRV2(p, x=hjds[34:68], dat2=rad2):
127     model2 = rv(x,1,2,p['V0'],p['K2'],p['K12'],p['e1234'],0,pi/2,
128                p['omega1234'],p['T1234'],p['T12'],p['P1234'],p['P12'])
129     sigma2 = 1
130     residual2 = (dat2 - model2)/sigma2
131     return residual2
132
133 def funcRV3(p, x=hjds[68:134], dat3=rad3):
134     model3 = rv(x,-1,3,p['V0'],p['K3'],p['K34'],p['e1234'],p['e34'],
135                p['omega34'], p['omega1234'],p['T1234'],p['T34'],
136                p['P1234'],p['P34'])
137     sigma3 = 1
138     residual3 = (dat3 - model3)/sigma3
139     return residual3
140
141 def funcRV4(p, x=hjds[134:200], dat4=rad4):
142     model4 = rv(x,-1,4,p['V0'],p['K4'],p['K34'],p['e1234'],p['e34'],
143                p['omega34'], p['omega1234'],p['T1234'],p['T34'],
144                p['P1234'],p['P34'])
145     sigma4 = 1
146     residual4 = (dat4 - model4)/sigma4
147     return residual4
148
149 def funcT(p, x=epochs, dat5=minima):

```

```

150     model5 = Tmin(x, dat5, p[ 'T1234' ], p[ 'P1234' ], p[ 'Q' ], p[ 'K12' ], p[ 'e1234' ],
151                 p[ 'omega1234' ], p[ 'T12' ], p[ 'P12' ])
152     sigma5 = 1
153     residual5 = (dat5 - model5)/sigma5
154     return residual5
155
156
157 # %% FIT ALL
158
159 def func(p, x=hjds, dat1=rad1, dat2=rad2, dat3=rad3, dat4=rad4, dat5=minima):
160     '''
161     Global residual function of all datasets to minimize. Sigma values taken from
162     previous single fits. The parameters are shared and bounded, they are optimized
163     globally.
164     '''
165     u1 = x[:34]
166     model1 = rv(u1, 1, 1, p[ 'V0' ], p[ 'K1' ], p[ 'K12' ], p[ 'e1234' ], 0, pi/2,
167               p[ 'omega1234' ], p[ 'T1234' ], p[ 'T12' ], p[ 'P1234' ], p[ 'P12' ])
168     u2 = x[34:68]
169     model2 = rv(u2, 1, 2, p[ 'V0' ], p[ 'K2' ], p[ 'K12' ], p[ 'e1234' ], 0, pi/2,
170               p[ 'omega1234' ], p[ 'T1234' ], p[ 'T12' ], p[ 'P1234' ], p[ 'P12' ])
171     u3 = x[68:134]
172     model3 = rv(u3, -1, 3, p[ 'V0' ], p[ 'K3' ], p[ 'K34' ], p[ 'e1234' ], p[ 'e34' ],
173               p[ 'omega34' ], p[ 'omega1234' ], p[ 'T1234' ], p[ 'T34' ],
174               p[ 'P1234' ], p[ 'P34' ])
175     u4 = x[134:200]
176     model4 = rv(u4, -1, 4, p[ 'V0' ], p[ 'K4' ], p[ 'K34' ], p[ 'e1234' ], p[ 'e34' ],
177               p[ 'omega34' ], p[ 'omega1234' ], p[ 'T1234' ], p[ 'T34' ],
178               p[ 'P1234' ], p[ 'P34' ])
179     u5 = hjds[200:]
180     model5 = Tmin(u5, dat5, p[ 'T1234' ], p[ 'P1234' ], p[ 'Q' ], p[ 'K12' ], p[ 'e1234' ],
181                 p[ 'omega1234' ], p[ 'T12' ], p[ 'P12' ])
182     sigma1 = 1
183     sigma2 = 1
184     sigma3 = 1
185     sigma4 = 1
186     sigma5 = 1
187
188     residual1 = (dat1 - model1)/sigma1
189     residual2 = (dat2 - model2)/sigma2
190     residual3 = (dat3 - model3)/sigma3
191     residual4 = (dat4 - model4)/sigma4
192     residual5 = (dat5 - model5)/sigma5
193
194     return concatenate((residual1, residual2, residual3, residual4, residual5))
195
196 # %% Call function
197
198 def call(function):
199     '''
200     Method to minimize residual function and show results. Returned report_fit()
201     '''
202
203

```

```

        contains resulting Chi-squared statistics and optimized parameters
    '''
204
205     result = minimize(function , p, method='nelder')
206     return report_fit(result) , result.params , result.redchi
207
208 def callchi(function):
209     '''
210     Method to minimize residual function and show results. Returns reduced Chi-squares
211     of individual data fits
212     '''
213     result = minimize(function , p, method='nelder')
214     return result.redchi
215 # %% Show result
216
217 '''
218 Minimizing the global residual function. The variable a[1] will contain the optimized
219     parameters which will be used in further plotting
220 '''
221
222 a = call(func)
223
224 '''
225 Minimizing the individual residual functions. Returns Chi-squared values of individual
226     fits
227 '''
228 chi1 = callchi(funcRV1)
229 chi2 = callchi(funcRV2)
230 chi3 = callchi(funcRV3)
231 chi4 = callchi(funcRV4)
232 chi5 = callchi(funcT)
233
234 print('\n', 'Reduced Chi-squared = ', round(chi1,2), round(chi2,2), round(chi3,2),
235       round(chi4,2), round(chi5,2),)
236
237
238 # %% Phases
239 '''
240 Constructing phase values (PHASE) from observational HJD values. Phases for fitting
241     curves (fit) are constructed through numpy linspace interval. The times of
242     periastron passage and orbital period are taken directly from global fit through
243     variable a[1].
244 '''
245
246 linfit1 = linspace(a[1]['T12'].value , a[1]['T12'].value+a[1]['P12'].value ,1000)
247 faza_fit1 = (linfit1 -a[1]['T12'].value)/a[1]['P12'].value
248 i ,fit1 = divmod(faza_fit1 ,1.001)
249 faza1 = (hjds[:34] - a[1]['T12'].value)/a[1]['P12'].value
250 i ,PHASE1 = divmod(faza1 ,1)
251
252 linfit2 = linspace(a[1]['T12'].value , a[1]['T12'].value+a[1]['P12'].value ,1000)
253 faza_fit2 = (linfit2 -a[1]['T12'].value)/a[1]['P12'].value
254 i ,fit2 = divmod(faza_fit2 ,1.0001)
255 faza2 = (hjds[34:68] - a[1]['T12'].value)/a[1]['P12'].value
256 i ,PHASE2 = divmod(faza2 ,1)
257
258 linfit3 = linspace(a[1]['T34'].value , a[1]['T34'].value+a[1]['P34'].value ,1000)
259 faza_fit3 = (linfit3 -a[1]['T34'].value)/a[1]['P34'].value

```

```

253 i, fit3 = divmod(faza_fit3, 1.001)
254 faza3 = (hjds[68:134] - a[1]['T34'].value)/a[1]['P34'].value
255 i, PHASE3 = divmod(faza3, 1)
256
257 linfit4 = linspace(a[1]['T34'].value, a[1]['T34'].value + a[1]['P34'].value, 1000)
258 faza_fit4 = (linfit4 - a[1]['T34'].value)/a[1]['P34'].value
259 i, fit4 = divmod(faza_fit4, 1.0001)
260 faza4 = (hjds[134:200] - a[1]['T34'].value)/a[1]['P34'].value
261 i, PHASE4 = divmod(faza4, 1)
262
263 # %% Prepare plot
264 '''
265 Constructing theoretical radial velocity curves to plot. Parameters are taken from
    the global fit through variable a[1].
266 '''
267 f1 = rv(linfit1, 1, 1, a[1]['V0'].value, a[1]['K1'].value, a[1]['K12'].value,
268         a[1]['e1234'].value, 0, pi/2, a[1]['omega1234'].value,
269         a[1]['T1234'].value, a[1]['T12'].value, a[1]['P1234'].value,
270         a[1]['P12'].value)
271
272 f2 = rv(linfit2, 1, 2, a[1]['V0'].value, a[1]['K2'].value, a[1]['K12'].value,
273         a[1]['e1234'].value, 0, pi/2, a[1]['omega1234'].value,
274         a[1]['T1234'].value, a[1]['T12'].value, a[1]['P1234'].value,
275         a[1]['P12'].value)
276
277 f3 = rv(linfit3, -1, 3, a[1]['V0'].value, a[1]['K3'].value, a[1]['K34'].value,
278         a[1]['e1234'].value, a[1]['e34'].value, a[1]['omega34'].value,
279         a[1]['omega1234'].value, a[1]['T1234'].value, a[1]['T34'].value,
280         a[1]['P1234'].value, a[1]['P34'].value)
281
282 f4 = rv(linfit4, -1, 4, a[1]['V0'].value, a[1]['K4'].value, a[1]['K34'].value,
283         a[1]['e1234'].value, a[1]['e34'].value, a[1]['omega34'].value,
284         a[1]['omega1234'].value, a[1]['T1234'].value, a[1]['T34'].value,
285         a[1]['P1234'].value, a[1]['P34'].value)
286
287 # %% Reduce the motion of mass center
288 '''
289 Reducing the motion of systems mass center from the observational data. Mass center
    equation is defined above
290 '''
291
292 red1 = rad1 - mc(hjds[:34], 1, a[1]['K12'].value, a[1]['e1234'].value,
293                a[1]['omega1234'].value, a[1]['T1234'].value, a[1]['P1234'].value)
294 red2 = rad2 - mc(hjds[34:68], 1, a[1]['K12'].value, a[1]['e1234'].value,
295                a[1]['omega1234'].value, a[1]['T1234'].value, a[1]['P1234'].value)
296 red3 = rad3 - mc(hjds[68:134], -1, a[1]['K34'].value, a[1]['e1234'].value,
297                a[1]['omega1234'].value, a[1]['T1234'].value, a[1]['P1234'].value)
298 red4 = rad4 - mc(hjds[134:200], -1, a[1]['K34'].value, a[1]['e1234'].value,
299                a[1]['omega1234'].value, a[1]['T1234'].value, a[1]['P1234'].value)
300
301 # %% PLOT
302 '''
303 Constructing phase diagrams of the reduced observational radial velocities and the
    theoretical radial velocity curves.
304 '''
305

```

```
306 f, (ax1, ax2) = plt.subplots(2,1,sharex=True,figsize=(8,10),
307                             gridspec_kw = {'height_ratios':[1, 1]})
308 f.subplots_adjust(hspace=0.2)
309
310 ax1.plot(PHASE1,red1,'ko',fillstyle='none', label='rv1')
311 ax1.plot(fit1,f1,'k—')
312 ax1.plot(PHASE2,red2,'k^', label='rv2')
313 ax1.plot(fit2,f2,'k—')
314 ax1.set_title('Contact binary RV fit')
315 ax1.set_ylabel('Radial velocity [km.s-1]')
316 ax1.set_xlim([0,1])
317 ax1.set_ylim([-300,300])
318 ax1.legend(loc='lower right')
319
320 ax2.plot(PHASE3,red3,'ko',fillstyle='none', label='rv3')
321 ax2.plot(fit3,f3,'k—')
322 ax2.plot(PHASE4,red4,'k^', label='rv4')
323 ax2.plot(fit4,f4,'k—')
324 ax2.set_title('Detached binary RV fit')
325 ax2.set_ylabel('Radial velocity [km.s-1]')
326 ax2.set_xlabel('Phase')
327 ax2.set_ylim([-90,75])
328 ax2.legend(loc='lower right')
329
330 f.savefig('plot.png',dpi=300)
331 plt.show()
```

# Appendix C

## The *Coordinates* module

```

1 """
2 @author: Emil Puha
3         Coordinates
4 """
5 from numpy import cos, sin, pi, sqrt, cbrt, array, arctan, tan
6
7 #%% Functions definitions
8
9 s = 86400
10 HJD = 2454619.58209*s
11 G = 6.67408e-11
12 ms = 1.9885e30
13
14 def radian(angle):
15     return (pi*angle/180)
16
17 def MtoAU(meters):
18     return meters*6.68e-12
19
20 def kep(e,M):
21     '''
22     Kepler equation
23     '''
24     j = 0
25     E = M
26     F = E - M - e*sin(E)
27     delta = 10**-8
28     while ( abs(F) >= delta ):
29         E = E - F/ (1 - e*cos(E))
30         F = E - e*sin(E)- M
31         j = j+1
32     return E
33
34 def kep_2_cart(t,m,a,e,i,P,w,Om,T):
35     '''
36     Main transformation equation. Transforms Keplerian orbital
37     elements to cartesian position and velocity vectors.
38     '''
39     mu = G*(m)
40     n = (2*pi)/(P)

```

```

41 M = n*(t - T)
42 E = kep(e,M)
43 nu = 2*arctan(sqrt((1+e)/(1-e)) * tan(E/2))
44 r = a*(1 - e*cos(E))
45
46 ox = r*cos(nu)
47 oy = r*sin(nu)
48
49 odotx = -(sqrt(mu*a)/r)*sin(E)
50 odoty = (sqrt(mu*a)/r)*(1-e**2)*cos(E)
51
52 x = ox*(cos(w)*cos(Om) -sin(w)*cos(i)*sin(Om)) \
53     -oy*(sin(w)*cos(Om)+cos(w)*cos(i)*sin(Om))
54 y = ox*(cos(w)*sin(Om) +sin(w)*cos(i)*cos(Om)) \
55     +oy*(cos(w)*cos(i)*cos(Om)-sin(w)*sin(Om))
56 z = ox*(sin(w)*sin(i)) +oy*(cos(w)*sin(i))
57
58 vx = odotx*(cos(w)*cos(Om) -sin(w)*cos(i)*sin(Om)) \
59     -odoty*(sin(w)*cos(Om)+cos(w)*cos(i)*sin(Om))
60 vy = odotx*(cos(w)*sin(Om) +sin(w)*cos(i)*cos(Om)) \
61     +odoty*(cos(w)*cos(i)*cos(Om)-sin(w)*sin(Om))
62 vz = odotx*(sin(w)*sin(i)) +odoty*(cos(w)*sin(i))
63
64 return array([x,y,z]),array([vx,vy,vz])
65
66 # %% Spectroscopic parameters of the contact orbit
67
68 P12 = 0.47755106*s
69 T12 = 2452500.1497*s
70 e12 = 0
71 K1 = 105.8*1000
72 K2 = 250.2*1000
73 K12 = 21.61*1000
74 w12 = pi/2
75 m1 = 1.66*ms
76 m2 = 0.7*ms
77 i12 = radian(79)
78
79 # %% Spectroscopic parameters of the detached orbit
80
81 P34 = 7.93063*s
82 T34 = 2452274.54*s
83 e34 = 0.035
84 K3 = 63.99*1000
85 K4 = 65.53*1000
86 K34 = 23.22*1000
87 w34 = 1.9
88 m3 = 1.1*ms
89 m4 = 1.09*ms
90 i34 = radian(68.9)
91
92 # %% Spectroscopic parameters of the mutual orbit
93
94 P1234 = 355.02*s
95 T1234 = 2453046*s
96 e1234 = 0.097

```

```

97 w1234 = 2.2
98 i1234 = radian(64.1)
99 M1234 = m1+m2+m3+m4
100
101 # %% Semimajor axis calculation of binary system
102
103 def semimajor(M,m1,m2,P):
104     '''
105     Computes semi-major axes of binary orbits using Kepler's 3rd law.
106     Determines distances of binary's components from mutual mass center.
107     '''
108     a = cbrt((G*M*(P)**2)/(4*(pi**2)))
109     r1 = a/(1+(m1/m2))
110     r2 = (a-r1)
111
112     print('AU:')
113     print('a= %8.6f' %(MtoAU(a)))
114     print('r1= %8.6f' %MtoAU(r1))
115     print('r2= %8.6f' %MtoAU(r2),'\n')
116     print('Meters:')
117     print('a= %8.6f' %a)
118     print('r1= %8.6f' %r1)
119     print('r2= %8.6f' %(a-r1))
120
121     return array([MtoAU(a),MtoAU(r1),MtoAU(r2)]), array([a,r1,r2])
122
123 mutual = semimajor(M1234,(m1+m2),(m3+m4),P1234)
124 comp34 = semimajor(m3+m4,m3,m4,P34)
125
126 # %% Cartesian coordinates of VW LMi's components
127
128 coord_of_12 = kep_2_cart(HJD,(m3+m4)**3/M1234**2,mutual[1][1],e1234,
129                        1.11875,P1234,2.2,0,T1234)
130 coord_of_34 = kep_2_cart(HJD,(m1+m2)**3/M1234**2,mutual[1][2],e1234,
131                        1.11875,P1234,2.2,0,T1234)
132
133 coord_of_3 = kep_2_cart(HJD,(m4)**3/(m3+m4)**2,comp34[1][1],e34,
134                        1.2025,P34,1.9,0,T34)
135 coord_of_4 = kep_2_cart(HJD,(m3)**3/(m3+m4)**2,comp34[1][2],e34,
136                        1.2025,P34,1.9,0,T34)

```

# Appendix D

## The N-body model

```
1 """
2 @author: Emil Puha
3         N-body model
4 """
5 import time
6 import numpy as np
7 import matplotlib.pyplot as plt
8 from Coordinates import coord_of_12 , coord_of_34 , coord_of_3 , coord_of_4 ,
9                             m1,m2,m3,m4,M1234
10 startTime = time.time()
11
12 class Vector:
13     def __init__(self ,x,y,z):
14         self.x = x
15         self.y = y
16         self.z = z
17
18     def __add__(self , other):
19         return Vector(self.x+other.x, self.y+other.y, self.z+other.z)
20
21     def Cross(self , other):
22         i = self.y*other.z - self.z*other.y
23         j = self.z*other.x - self.x*other.z
24         k = self.x*other.y - self.y*other.x
25         return Vector(i,j,k)
26
27     def Vel(self):
28         d = (self.x*self.x + self.y*self.y + self.z*self.z)
29         return d
30
31     def Value(self):
32         d = (self.x*self.x + self.y*self.y + self.z*self.z)**0.5
33         return d
34
35     def __sub__(self , other):
36         return Vector(self.x-other.x, self.y-other.y, self.z-other.z)
37
38     def __rmul__(self , other):
39         return Vector(self.x*other , self.y*other , self.z*other)
40
```

```

41     def __mul__(self, other):
42         if type(self) == type(other):
43             return self.x*other.x+self.y*other.y+self.z*other.z
44         else:
45             return Vector(self.x*other, self.y*other, self.z*other)
46
47     def __truediv__(self, other):
48         return Vector(self.x/other, self.y/other, self.z/other )
49
50 class ObjectAttributes:
51     def __init__(self, t, pos, acc, vel):
52         self.t = t
53         self.pos = pos
54         self.vel = vel
55         self.acc = acc
56
57 class EnergyAttributes:
58     def __init__(self, t, e, m):
59         self.t = t
60         self.e = e
61         self.m = m
62
63 class Body:
64     def __init__(self, mass, x, y, z, vx, vy, vz):
65         self.mass = mass
66         self.pos = Vector(x, y, z)
67         self.vel = Vector(vx,vy,vz)
68         self.acc = Vector(0., 0., 0.)
69         self.G = 6.67408e-11
70         self.attributes = list()
71         self.energies = list()
72         self.newpos = Vector(0., 0., 0.)
73         self.newvel = Vector(0., 0., 0.)
74
75     def CalcAcc(self, other, t, dt):
76         acc = Vector(0,0,0)
77         direction = other.pos - self.pos
78         distance = direction.Value()
79         if distance !=0:
80             acc =(-self.G*other.mass*direction)/(distance **3)
81         return acc
82
83     def CalcAccRK(self, other, t, dt):
84         acc = Vector(0,0,0)
85         direction = other.newpos - self.newpos
86         distance = direction.Value()
87         if distance !=0:
88             acc =(-self.G*other.mass*direction)/(distance **3)
89         return acc
90
91     def Energy(self, other, t):
92         direction = other.pos - self.pos
93         T = 0.5*self.mass*(self.vel.Vel())
94         U = (-self.G*self.mass*other.mass)/direction.Value()
95         return T+U
96

```

```

97     def Momentum(self, t):
98         Lx = self.pos.y*self.mass*self.vel.z - self.pos.z*self.mass*self.vel.y
99         Ly = self.pos.z*self.mass*self.vel.x - self.pos.x*self.mass*self.vel.z
100        Lz = self.pos.x*self.mass*self.vel.y - self.pos.y*self.mass*self.vel.x
101        return Lx + Ly + Lz
102
103 class Model:
104     objects = list()
105
106     def __init__(self):
107         pass
108
109     def RK4(self, t, dt):
110
111         if len(self.objects) > 1:
112             for Body in self.objects:
113                 # Runge-kutta 1st step
114                 hacc = Vector(0,0,0)
115                 for other in self.objects:
116                     if Body != other:
117                         hacc -= Body.CalcAcc(other, t, dt)
118
119                 k1 = (t, Body.vel, hacc)
120
121                 # Runge-kutta 2nd step
122                 Body.newpos = Vector(0., 0., 0.)
123                 Body.newvel = Vector(0., 0., 0.)
124                 Body.newpos += Body.pos + Body.vel*0.5*dt
125                 Body.newvel += Body.vel + Body.acc*0.5*dt
126
127                 hacc1 = Vector(0,0,0)
128                 for other in self.objects:
129                     if Body != other:
130                         hacc1 -= Body.CalcAccRK(other, t, 0.5*dt)
131                 k2=(t, Body.newpos, Body.newvel, hacc1)
132
133                 # Runge-kutta 3rd step
134                 Body.newpos = Vector(0., 0., 0.)
135                 Body.newvel = Vector(0., 0., 0.)
136                 Body.newpos += k2[1] + k2[2]*0.5*dt
137                 Body.newvel += k2[2] + k2[3]*0.5*dt
138
139                 hacc1 = Vector(0,0,0)
140                 for other in self.objects:
141                     if Body != other:
142                         hacc1 -= Body.CalcAccRK(other, t, 0.5*dt)
143                 k3=(t, Body.newpos, Body.newvel, hacc1)
144
145                 # Runge-kutta 4th step
146                 Body.newpos = Vector(0., 0., 0.)
147                 Body.newvel = Vector(0., 0., 0.)
148                 Body.newpos += k3[1] + k3[2]*dt
149                 Body.newvel += k3[2] + k3[3]*dt
150
151                 hacc1 = Vector(0,0,0)
152                 for other in self.objects:

```

```

153         if Body != other:
154             hacc1 -= Body.CalcAccRK(other, t, dt)
155         k4=(t, Body.newpos, Body.newvel, hacc1)
156
157         # Runge-kutta Update attributes
158         update_pos = (1/6)*(k1[1] + 2*(k2[2] + k3[2])+k4[2])
159         update_vel = (1/6)*(k1[2] + 2*(k2[3] + k3[3])+k4[3])
160
161         Body.acc = update_vel
162         Body.vel += update_vel*dt
163         Body.pos += update_pos*dt
164         Body.attributes.append(ObjectAttributes(t, Body.pos, Body.acc,
165                                             Body.vel))
166
167         for other in self.objects:
168             if Body != other:
169                 ha = Body.Energy(other, t)
170
171                 fa = Body.Momentum(t)
172                 Body.energies.append(EnergyAttributes(t, ha, fa))
173     return
174
175     def simulation(self, method, N, years):
176         work_t = 0
177         j = N/20
178         day = 86400
179         interval = years*365.25*day
180         step = interval/N
181         i = 0
182         for i in range(N):
183             work_t += step
184             i += 1
185             method(work_t, step)
186             if i % j == 0:
187                 print('Status: ', i*100/N, '%')
188     return
189
190     def plot(self):
191         d = len(self.objects)
192         work = list()
193         for Body in self.objects:
194             for a in Body.attributes:
195                 work.append([a.pos.x, a.pos.y])
196         work = np.array(work)
197         work = np.vsplit(work, d)
198
199         for i in range(d):
200             x = work[i][:, 0]
201             y = work[i][:, 1]
202             x1 =work[i][:, 0][-1]
203             y1 =work[i][:, 1][-1]
204             plt.plot(x, y, 'k-')
205             plt.plot(x1, y1, 'ko')
206
207         plt.savefig('plot.png', dpi=300)
208         plt.show()

```

```

209         return
210
211 # %% Defining the model of VW LMi
212
213 def VW():
214     star12 = Body(m1+m2,
215                  coord_of_12 [0][0], coord_of_12 [0][1], coord_of_12 [0][2],
216                  coord_of_12 [1][0], coord_of_12 [1][1], coord_of_12 [1][2])
217
218     star3 = Body(m3,
219                 -coord_of_34 [0][0] -coord_of_3 [0][0],
220                 -coord_of_34 [0][1] -coord_of_3 [0][1],
221                 -coord_of_34 [0][2] -coord_of_3 [0][2],
222                 -coord_of_34 [1][0] -coord_of_3 [1][0],
223                 -coord_of_34 [1][1] -coord_of_3 [1][1],
224                 -coord_of_34 [1][2] -coord_of_3 [1][2] )
225
226     star4 = Body(m4,
227                 -coord_of_34 [0][0] +coord_of_4 [0][0],
228                 -coord_of_34 [0][1] +coord_of_4 [0][1],
229                 -coord_of_34 [0][2] +coord_of_4 [0][2],
230                 -coord_of_34 [1][0] +coord_of_4 [1][0],
231                 -coord_of_34 [1][1] +coord_of_4 [1][1],
232                 -coord_of_34 [1][2] +coord_of_4 [1][2] )
233
234     modelVW = Model()
235     modelVW.objects.append(star12)
236     modelVW.objects.append(star3)
237     modelVW.objects.append(star4)
238
239     modelVW.simulation(modelVW.RK4,750000,1)
240     modelVW.plot()
241     return
242
243 # %% Calling the simulation
244
245 VW()
246
247 def humanize_time(secs):
248     mins, secs = divmod(secs, 60)
249     hours, mins = divmod(mins, 60)
250     return '%02d:%02d:%02.2f' % (hours, mins, secs)
251 print('Run time:',humanize_time(time.time() - startTime))

```

# Appendix E

## The *Elements* module

```

1 """
2 @author: Emil Puha
3         Elements
4 """
5 import pandas as pd
6 import matplotlib.pyplot as plt
7 from numpy import linalg, cross, arccos, pi, dot, array
8
9 #%% Transformation
10
11 def degree(angle):
12     return (angle*180/pi)
13
14 def cart_2_kep1(t,m1,m2,r_vec,v_vec):
15     '''
16     Main transformation equation. Transforms cartesian position
17     and velocity vectors to Keplerian orbital elements.
18     '''
19     G = 6.67408e-11
20     h_bar = cross(r_vec,v_vec)
21     h = linalg.norm(h_bar)
22     r = linalg.norm(r_vec)
23     v = linalg.norm(v_vec)
24     a = (G*(m1+m2)*r)/(2*G*(m1+m2)-r*v**2)
25     i = arccos(h_bar[2]/h)
26     ecc_vec = ((cross(v_vec,h_bar))/(G*(m1+m2)))-(r_vec/r)
27     e = linalg.norm(ecc_vec)
28     one = (0,0,1)
29     n_v = cross(one,h_bar)
30     n = linalg.norm(n_v)
31
32     if n_v[1] >= 0:
33         Omega = arccos(n_v[0]/n)
34     elif n_v[1] < 0:
35         Omega = 2*pi - arccos(n_v[0]/n)
36         if Omega >= pi:
37             Omega = -arccos(n_v[0]/n)
38
39     if ecc_vec[2] >= 0:
40         omega = arccos((dot(n_v,ecc_vec))/(n*e))

```

```

41
42     else:
43         omega = 2*pi - arccos((dot(n_v, ecc_vec))/(n*e))
44
45     return a, e, degree(i), degree(Omega), degree(omega), \
46           h_bar[0], h_bar[1], h_bar[2]
47
48 # %% Read data
49 '''
50 Read the results of numerical integration. Parameter 'f' denotes the
51 angle Omega1234.
52 '''
53 f = 330
54
55 ms = 1.9885e30
56 m1 = 1.66*ms
57 m2 = 0.7*ms
58 m3 = 1.1*ms
59 m4 = 1.09*ms
60
61 data = pd.read_csv('500P_12+34/data_'+str(f)+'.txt', delimiter=',')
62 matrix = data.values
63 time = matrix[:,0]
64 pos12 = matrix[:,1:4]
65 vel12 = matrix[:,4:7]
66 pos34 = matrix[:,7:10]
67 vel34 = matrix[:,10:13]
68
69 data34 = pd.read_csv('500P_1+2+3+4/data_'+str(f)+'.txt', delimiter=',')
70 matrix34 = data34.values
71 pos3 = matrix34[:,13:16]
72 vel3 = matrix34[:,16:19]
73 pos4 = matrix34[:,19:22]
74 vel4 = matrix34[:,22:25]
75
76 # %% Compute orbital elements
77
78 work34 = list()
79 work1234 = list()
80
81 for j in range(len(time)):
82     w34 = cart_2_kep1(time[j], m3, m4, -pos3[j]+pos4[j], -vel3[j]+vel4[j])
83     w1234 = cart_2_kep1(time[j], m1+m2, m3+m4, -pos12[j]+pos34[j],
84                       -vel12[j]+vel34[j])
85     work34.append(w34)
86     work1234.append(w1234)
87
88 work34=array(work34)
89 work1234=array(work1234)
90
91 a34=work34[:,0]
92 e34 = work34[:,1]
93 i34= work34[:,2]
94 Om34= work34[:,3]
95 om34 = work34[:,4]
96 h34 =work34[:,5:8]

```

```

97
98 a1234=work1234[:,0]
99 e1234 = work1234[:,1]
100 i1234= work1234[:,2]
101 Om1234= work1234[:,3]
102 om1234 = work1234[:,4]
103 h1234 =work1234[:,5:8]
104
105 r = 19999
106 d = 10
107 dt = time[:,r][::d]/31557600
108
109 plt.plot(dt,e34[:,r][::d], 'k-')
110 plt.ylim(0.01,0.07)
111 plt.xlabel('Time [years]')
112 plt.ylabel('$e_{34}$')
113 plt.savefig('e34_'+str(f)+'.png',dpi=200)
114 plt.show()
115
116 plt.plot(dt,i34[:,r][::d], 'k-')
117 plt.xlabel('Time [years]')
118 plt.ylabel('$i_{34}$ [$\degree$]')
119 plt.savefig('i34_'+str(f)+'.png',dpi=200)
120 plt.show()
121
122 plt.plot(dt,Om34[:,r][::d], 'k-')
123 plt.xlabel('Time [years]')
124 plt.ylabel('$\Omega_{34}$ [$\degree$]')
125 plt.savefig('Omega34_'+str(f)+'.png',dpi=200)
126 plt.show()
127
128 plt.plot(dt,om34[:,r][::d], 'k-')
129 plt.xlabel('Time [years]')
130 plt.ylabel('$\omega_{34}$ [$\degree$]')
131 plt.savefig('Somega34_'+str(f)+'.png',dpi=200)
132 plt.show()
133
134 # %% Mutual inclinations
135
136 listJ = list()
137
138 for p in range(len(h34)):
139     a=dot(h34[p],h1234[p])
140     b = (linalg.norm(h34[p]))*(linalg.norm(h1234[p]))
141     J = arccos(a/b)
142     listJ.append(degree(J))
143
144 listJ=array(listJ)
145
146 plt.plot(dt,listJ[:,r][::d], 'k-')
147 plt.xlabel('Time [years]')
148 plt.ylabel('$J_{mutual}$ [$\degree$]')
149 plt.savefig('mutual_inlination_'+str(f)+'.png',dpi=200)
150 plt.show()

```